RICE UNIVERSITY

The Mechanical Characterization of Multi-Wall Carbon Nanotubes and Related Interfaces in Nanocomposites
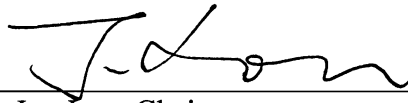
by

Yogeeswaran Ganesan

A THESIS SUBMITTED
IN PARTIAL FULFILLMENT OF THE
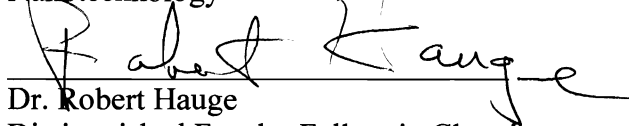REQUIREMENTS FOR THE DEGREE

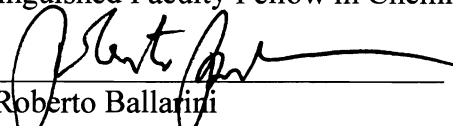**Doctor of Philosophy**

APPROVED, THESIS COMMITTEE:

_____
Dr. Jun Lou, Chair
Assistant Professor ofMechanical Engineering and
Materials Science

_____
Dr. Pulickel M. Ajayan
Benjamin M. and Mary Greenwood Anderson
Professor in Engineering Materials Science and
Nanotechnology

_____
Dr. Robert Hauge
Distinguished Faculty Fellow in Chemistry

_____
Dr. Roberto Ballarini
James L. Record Professor and Head, Department
of Civil Engineering, The University of Minnesota

HOUSTON, TEXAS
Nov_ 2010

A working class hero is something to be…..

<div style="text-align: right">-   John Lennon</div>

Abstract

This thesis primarily documents the development and application of a novel technique, which involves the usage of a silicon micro-mechanical device that operates in conjunction with a quantitative nanoindenter within an electron microscope, for the mechanical characterization of nanomaterials and interfaces in composites. The technique was used to conducted tensile tests on individual pristine, nitrogen doped and sidewall fluorinated multi-wall carbon nanotubes (MWNTs), which were found to exhibit varied load-bearing abilities and unique fracture modes. The technique was also used to perform single fiber pullout experiments to study the MWNT/polymer (epoxy) interface. Interfacial failure was found to occur in a brittle fashion, in a manner consistent with the predictions of continuum fracture mechanics models. Although an improvement in the interfacial adhesion was observed upon sidewall fluorination of the MWNT reinforcements, the results of the study essentially highlighted the weak nature of the forces that bind MWNTs to an epoxy matrix.

Acknowledgements

First and foremost, I would like to sincerely thank my advisor Professor Jun Lou, who has served as an extraordinary mentor to me. It has truly been an honor working under his brilliant guidance over the past four years. I am deeply indebted to all my colleagues at the Lou lab, especially Mr. Cheng Peng, who has made significant contributions to this thesis, Dr. Yang Lu and Ms. Avery Cate. I would like to thank my parents, Mrs. Bhavani Ganesan and Mr. S. Ganesan for their constant support and encouragement over the years. I am extremely grateful to Dr. Lijie Ci and Dr. Valery Khabashesku for providing invaluable samples and for useful discussions, the University of Minnesota NFC staff, Mr. Steve Ripley and Mr. Long Chang for help provided with a number of experiments and all my friends at Rice MEMS ("I got by with a little help from my friends"). I must also thank my committee members, Professors P. M. Ajayan, Roberto Ballarini and Robert Hauge for their constructive feedback and stimulating questions. Finally, I would like to thank Professors H. Daniel Wagner and Roberto Ballarini (again), whose work in the areas of nanocomposites and MEMS based mechanical testing respectively have served as "jumping off" point for this thesis.

Table of Contents

Figures and Tables

1. Introduction

1.1. Nanostructures/Nanomaterials

A nanostructure can be defined as either a bulk material with a grain structure of a nominal size in the range of 1 to 100 nanometers, or a structure having one or more dimensions below 100 nm. [1] The past couple of decades have seen an emergence of numerous nanoscale structures including nanowires, nanorods, nanotubes and nanobelts of various materials (see Figure 1.1). A number of applications, in fields as diverse as chemical sensing, high performance composites, nano-electro-mechanical systems (NEMS) and solar cells, have been envisioned for these materials.

Metal and semiconductor nanowires are examples of quasi one-dimensional (1-D) nanostructures that have generated a considerable amount of interest owing to their unique optical, electrical, mechanical and magnetic properties. Increased surface area, very high density of electronic states and joint density of states near the energies of their van Hove singularities, enhanced exciton binding energy, diameter-dependent bandgap and increased surface scattering for electrons and phonons are just some of the reasons why nanowires differ from their corresponding bulk materials. [2] Also, nanowires have been found to possess superior mechanical properties that include having high yield strength values and strength values as high as 100 times that of bulk materials and substantially larger than those reported for bulk nanocrystalline metals. [3]

These materials are generally synthesized either by electrodeposition, physical vapor deposition (PVD) or chemical vapor deposition (CVD) within a nanochannel template or by a vapor-liquid-solid (VLS) mechanism based anisotropic crystal growth method. Nanochannel templates, such as anodic aluminum oxide (AAO) or nano-channel glass (NCG), contain very small cylindrical pores or voids within the host material; these empty spaces can be filled with the chosen material, by one of the aforementioned deposition techniques, in order to form nanowires. The VLS mechanism was first proposed for the growth of single crystal silicon whiskers. The proposed growth mechanism involves the absorption of source material from the gas phase into a liquid droplet of catalyst, supersaturation of the liquid alloy and finally a nucleation event that generates a solid precipitate of the source material.

Nanowires, unlike a number of low dimensional systems have two quantum confined directions, while still leaving one unconfined direction for electrical conduction. [2] This allows nanowires to be used in applications where electrical conduction, rather than tunneling transport, is required. Transport studies of ferromagnetic nanowire arrays (Ni, Fe) have also received much attention because of their potential for high-density magnetic storage applications. Other potential applications for these materials lie in the areas of optical switching, thermoelectricity, drug delivery and hybrid electronics.
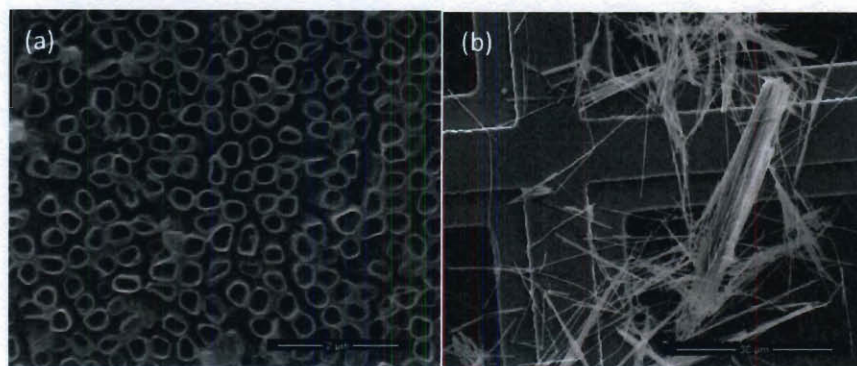
Figure 1.1 (a) SEM image shows semi-conducting TiO$_2$ nanotube arrays grown via anodization (electrochemical method). (b) SEM image shows Ni nanowire bundles (grown via cathodic electrodeposition within an AAO template) on a TEM grid.

Another example of a (quasi) 1-D nanostructure is a carbon nanotube (CNT), a molecular scale fibrous structure made of carbon atoms (see Figure 1.2). Probably the simplest way to envision the structure of a CNT is to imagine a flat sheet of graphite (graphene) rolled into the form of a hollow cylinder. CNTs form two structurally distinct classes. Multi-walled CNTs (MWNTs) were the first to be discovered [4] and exhibit a Russian doll-like structure of nested concentric tubes. Their interlayer spacing can range from 0.342 to 0.375 nm, depending on the diameter and number of shells comprising the tube. The second type of CNTs is the basic single rolled-up graphitic sheet i.e. a single-walled CNT (SWNT). SWNTs produced by most techniques are nearly uniform in diameter (generally between 0.5 to 2 nm) and have the tendency to self-organize into "ropes" held together by van der Waals interaction.

There are several ways of producing nanotubes (see Figure 1.3). Small quantities of nanotubes (both SWNTs and MWNTs) with few structural defects can be produced by methods based on cooling a carbon plasma generated during

an arc discharge between two graphitic electrodes in an inert atmosphere. [4] The carbon plasma can also be formed by laser ablation of a graphitic target. [5] A technique, known as the high-pressure carbon monoxide (HiPco) process, has been used to produce SWNTs from gas-phase reactions of iron carbonyl in carbon monoxide at high pressures (10-100 atm.). [6] There are also a number of methods that rely on the catalytic decomposition of various hydrocarbons, e.g. methane or acetylene mixed with nitrogen or hydrogen in the presence of catalysts [7], within a chemical vapor deposition (CVD) chamber, that allow the controlled growth of nanotubes. Such methods are particularly advantageous since they are suitable for producing structures integrated with CNTs as well as CNTs in industrial quantities.

Despite being structurally similar to a single sheet of graphite, which is a semiconductor with zero band-gap, SWNTs may be either metallic or semiconducting, depending on the sheet rolling direction (chirality) and curvature. The electronic properties of perfect MWNTs are rather similar to those of perfect SWNTs, because the coupling between the nested cylinders is weak in MWNTs. Owing to their nearly one-dimensional electronic structure, ballistic electronic transport is found to occur in metallic SWNTs and MWNTs over long distances, enabling them to carry high currents with essentially no heating. Phonons also propagate easily along the nanotube: The measured room temperature thermal conductivity for an individual MWNT (>3000 W/m·K) is greater than that of natural diamond and the basal plane of graphite (both 2000 W/m·K). [8] Superconductivity has been observed with transition temperatures of ~0.55 K for

1.4-nm-diameter SWNTs. [9] CNTs also possess some extraordinary mechanical properties (detailed in Chapter 2), closely related to those of graphite. Owing to their uniqueness, CNTs are currently being studied for a number of high-tech applications – as components in single electron transistors, as transparent electrodes in solar cells, as VLSI interconnects, as reinforcements for high-performance composites and as mechanical memory elements.
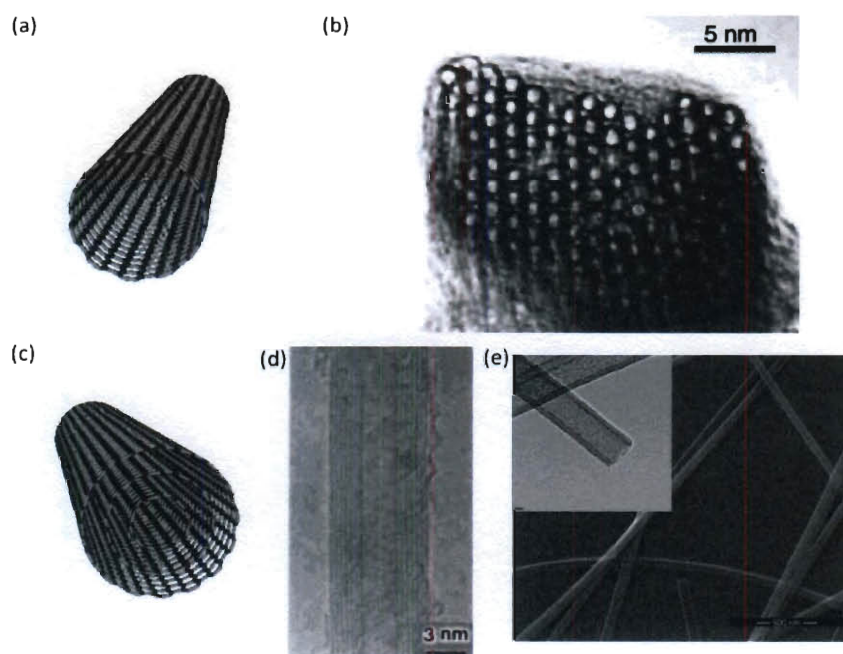
Figure 1.2 (a) Atomistic model of a SWNT, (b) TEM image of a bundle of SWNTs, |5| (c) atomistic model of a MWNT, (d) TEM image of a MWNT |4| and (e) SEM image of highly disordered MWNTs grown via hydrocarbon (acetylene) decomposition within the channels of an AAO template (inset shows a TEM image of the nanotubes). The scale bar in the inset reads 20 nm.
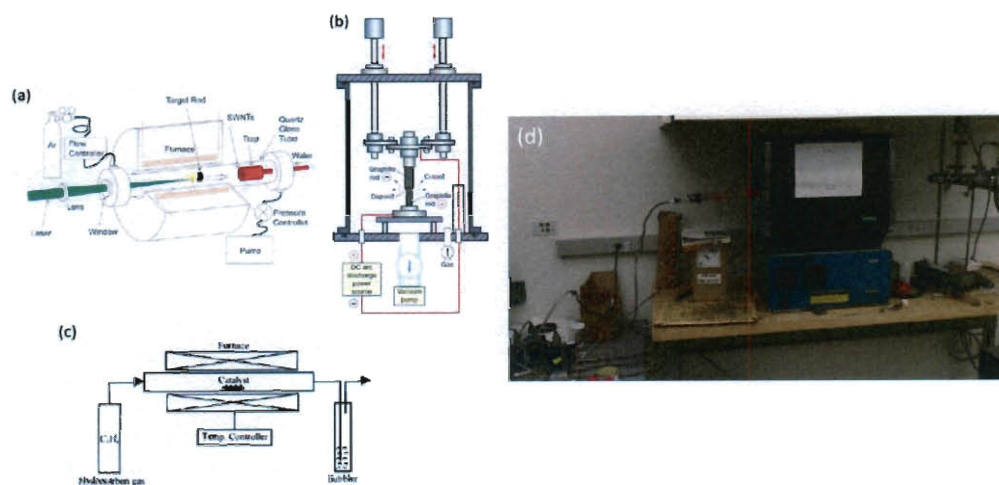
Figure 1.3 CNT growth techniques include (a) Laser ablation, (b) Arc discharge, (c) Catalytic CVD. [10] (d) CVD system setup for MWNT growth.

1.2. Nanocomposites

A nanocomposite is created by introducing nanomaterials into a macroscopic matrix, usually a polymer, a metal or a ceramic. Nanocomposites represent a new class of material alternative to conventional composites and possess some extremely interesting properties. There are a number of reasons for this. (a) Firstly, nanoscale fillers often have properties that are different from the bulk properties of the same material. Hence, nanoparticles provide an opportunity for creating composites with unique properties. (b) One should note that nanoscale fillers can be considered small defects as opposed to micrometer-scale fillers, which are similar in size to the critical crack size for failure. Nanocomposites are thus expected to possess superior ductility and toughness. (c) Nanocomposites, particularly the ones with a polymer matrix, have a low percolation threshold (ultra-low filler levels required for connectivity through the

sample) and can be developed with extremely low filler loading (values less than 5 vol.% [11]) when compared to traditional micrometer sized filler reinforced composites (in some cases values as high as 60 vol. % are necessary). (d) Lastly, due to the large surface area of the fillers, nanocomposites have a large volume of interfacial matrix material with properties different from the bulk matrix material. This interfacial material can dramatically modify the thermal, mechanical, and electrical properties of the overall composite.

There are a number of areas in which nanofilled composites are expected to have a considerable technical impact in the coming years. In the field of tribology, for example, the wear rate of PTFE (polytetrafluoroethylene), a solid lubricant, can be reduced by 4 orders of magnitude by the addition of alpha phase alumina nanoparticles into the matrix, without dramatically affecting its dry sliding friction coefficient. [11] Studies involving the usage of CNTs to reinforce a wide range of polymer matrices have been reported, and there is growing interest in CNT/ceramic and CNT/metal composites. Much of the work pertaining to the preparation of carbon nanotube composites has been driven by a desire to exploit the tubes' stiffness and strength. CNTs have also been incorporated into conducting polymers matrices such as poly-aniline in order to develop composites that provide enhanced conductivity (as well as improved mechanical properties). These materials are of interest for electronic dissipation, light emitting diodes, photovoltaics and non-linear optics.

A commonly used method for preparing CNT reinforced polymer composites involves the mixing of CNT dispersions (in solvents such as toluene)

with solutions of the polymer followed by controlled solvent evaporation. The nanotubes are often pretreated chemically to facilitate effective dispersion. Melt processing techniques such as shear mixing and extrusion can be used to produce CNT based composites if the matrix material is a thermoplastic. Shear mixing results in a homogeneous dispersion of nanotubes within a matrix and extrusion is generally used to produce nanotube alignment or to fabricate artifacts in the required form by injection molding. Techniques described so far focus on producing composites in which the nanotubes are distributed evenly throughout the polymer. For a number of applications, however, a layered or a hierarchical arrangement is advantageous. Such structures can be obtained by layer by layer deposition or by solvent exchange processing techniques. Spark plasma sintering, sol gel synthesis and *in situ* CNT growth techniques can be used to fabricate CNT/ceramic composites. Powder metallurgy techniques, conventional powder mixing, melting and drawing and electroless plating methods can be used to fabricate CNT/metal composites. [12]

1.3. Mechanics at Small Scales

Materials and structures with small scale dimensions, such as nanomaterials, have been known to exhibit large deviations from bulk properties. The deviations can be caused owing to a number of effects; the presence of a finite number of grains in a given structure, surface, interface and intermolecular mechanisms and the role played by factors such as residual stresses and defects such as dislocations. For example, when a thin film's dimensions begin to approach that of its microstructural features (i.e. micron & submicron regime),

mechanical properties such as plasticity, fracture toughness and fatigue resistance begin to exhibit size effects (see Figure 1.4). [1] This happens since all these properties depend on defect generation and evolution. The strength of materials with pre-existing dislocations can be increased by reducing systems' characteristic length scales. In crystals, the strengthening mechanism is based either on the blockage or on the elimination of dislocations; the Hall–Petch strengthening effect in polycrystalline metals arises because of dislocation blockage whereas the ultra-strength in nanoscale pillars is a representative example of strengthening by dislocation elimination (starvation). [13] Dislocations also play an important role in the relaxation and intramolecular plasticity observed in carbon based nanostructures such as carbon nanotubes. Dislocations dipoles comprised of 5-7 Stone–Wales (SW) defects play a key role in CNT relaxation under tension. The formation of such defects in CNTs depends on a number of interdependent factors such as strain, symmetry, time, and temperature. When the dislocations unlock, one of two possible mechanisms occur, depending upon the temperature. At low temperatures, a mechanism of transformations, 7/8/7 followed by 7/8/8/7 and so on and so forth, leads to the brittle failure upon formation of larger molecular openings such as 7/14/7. At high temperatures however, the two dislocations glide away along a spiral path, leaving behind a nanotube of smaller diameter and different symmetry (chirality). [14] Elastic properties are dependent on the nature of bonding and only exhibit size effects at the atomic scale. However, as the grain size or structural

dimensions fall below 50 nanometers, mechanical behavior control is transitioned from dislocation based mechanisms to surface and intermolecular mechanisms.

With regard to theories and simulations used to predict material behavior at different length scales, it is important to first understand that classical plasticity, which can be described in terms of traditional continuum mechanics, is applicable only when the dimensions are greater than ~100 μm. Molecular dynamics (MD) is applicable at the other end of the scale and involves the generation, mobility, and interaction between individual dislocations, twinning, stacking faults and other defects. However, since it is based on large scale numerical simulations it can, in general, only be used to study systems that are less than one million atoms in size (i.e. limited by computational power). In the regime between classical plasticity and molecular dynamics, theories such as strain gradient plasticity have been used and models based on discrete dislocation mechanics have been proposed to predict mechanical behavior. However, all theories and models require experimental verification, which is why fields such as experimental nanomechanics and *in situ* nanomechanical testing (defined as the testing of a material while simultaneously observing its deformation and microstructure evolution) are relevant; in order to (a) observe the nature of mechanical behavior at small scales and to (b) determine what are the underlying mechanisms that dictate mechanical behavior at small scales.
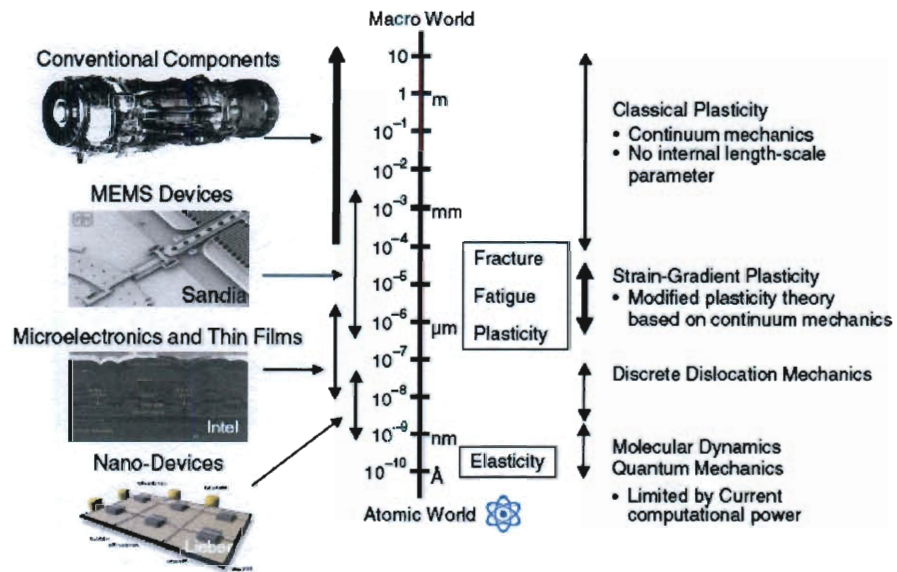
Figure 1.4 Illustration of length-scale effects on the mechanical properties of materials. [1] The right side of figure lists the theories used to predict material behavior and the length scales at which they are applicable.
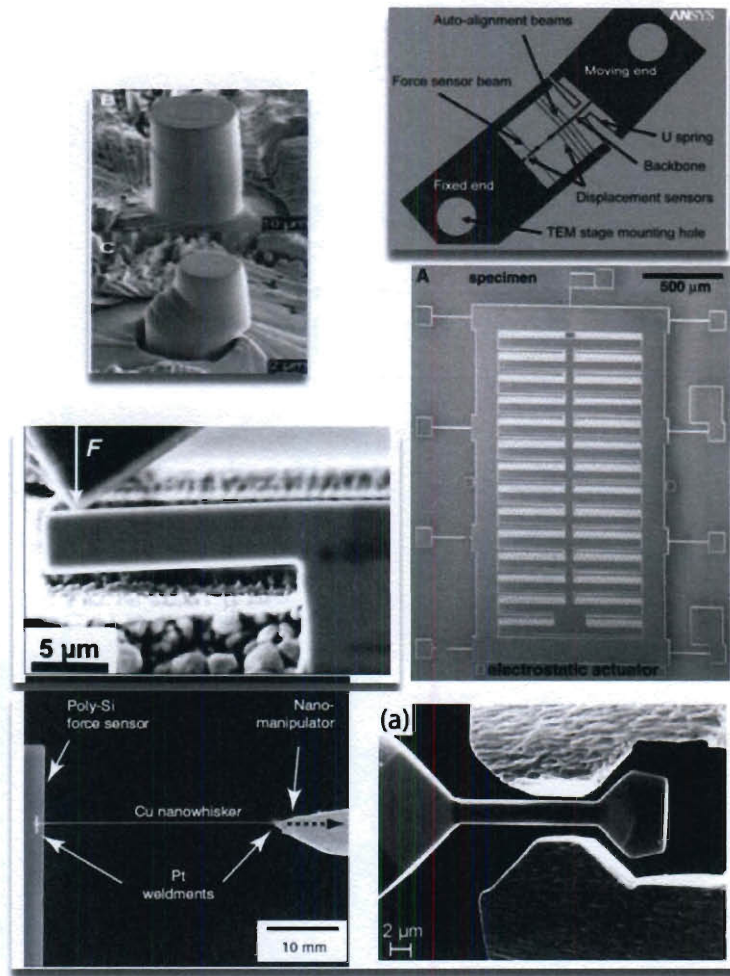
Figure 1.5 Collage shows a few representative *in situ* mechanical testing techniques that are currently being used by researchers to study the mechanical properties of small scale materials.

1.4. Thesis Overview

One of the main purposes of this thesis is to present a novel technique that can be used to perform nanomechanical experiments within an electron microscope (transmission or scanning) chamber. The technique, which involves the usage of a novel microfabricated device that works in conjunction with a quantitative nanoindenter, can be used to study the mechanical properties of

nanomaterials and interfaces in nanocomposites while simultaneously observing their deformation and failure in real time. The development of the technique and its application for the mechanical characterization of Ni nanowires are discussed in Chapter 3. Chapter 4 discusses the mechanical characterization of individual catalytically grown multi-wall carbon nanotubes (pristine, nitrogen-doped and sidewall functionalized) conducted using the technique. Chapter 5 discusses single CNT pullout experiments that were conducted, using the novel technique, to study the mechanical properties of interfaces in multi-walled carbon nanotube reinforced epoxy composites.

2. Mechanical Characterization of Carbon Nanotubes and Related Interfaces in Composites: Literature Review

2.1. Carbon Nanotubes: Properties and Characterization

Owing to their remarkable properties (briefly described in Chapter 1), the discovery of CNTs has opened whole new fields of study in the areas of physics, chemistry and materials science. Nanotubes possess a unique combination of small size (diameters ranging from approx. 1 to 100 nm and lengths up to several mm), low density, high stiffness, high strength (reported values vary between 30 and 110 GPa [15, 16] for MWNTs and between 13 and 53 GPa [17] for SWNTs) and a broad range of electronic properties from metallic to p- and n-doped semiconducting.

As mentioned earlier, CNTs are essentially single sheets of graphene, rolled into a cylindrical shape with axial symmetry. The direction of the rollup is described by the chiral vector $C_h = na_1 + ma_2$ (where n and m are integers and the magnitude of the vectors a_1 and a_2 is equal to the lattice constant of graphite, 2.49 A). The chirality of a nanotube dictates its electronic properties (these properties are also diameter dependent to some extent) and also plays a role in determining its strength and Poisson's ratio. With regard to other mechanical properties, it is important to note that sp^2-hybridized in-plane bonds (σ-bonds), that are 1.42 A

long (same as in graphite), give them an exceptionally high Young's modulus while out-of-plane π bonds are responsible for the weak van der Waals interlayer (MWNTs) or inter-tube (SWNTs) cohesion. The Young's Modulus of a CNT has been theoretically estimated to be equal to 0.97 TPa [18] (assuming the interlayer separation of graphite, 0.34 nm, to be equal to the nanotube's thickness), a value which is in good agreement with the C_{11} elastic constant of graphite. This value has been known to be practically independent of the tube's chirality and diameter (in the range 0.68–27 nm).

Owing to their small size and the magnitude of the forces and deformation involved, the mechanical characterization of individual CNTs can be extremely challenging. The first measurements of the mechanical properties of CNTs were thus indirect, based on measuring the amplitude of their thermally induced vibrations inside a transmission electron microscope. [23] The nanotubes were modeled as stochastically driven resonators and their Young's moduli were estimated from their Gaussian vibrational profiles. From a series of measurements performed as a function of temperature an average Young's Modulus value of 1.8 GPa was obtained. A similar method, that involved the direct excitation of MWNTs using an AC electric field, was used subsequently by researchers to calculate the bending modulus, $E_{bending}$ of CNTs (see Figure 2.1(a)). [24] For nanotube diameters below 10 nm, a typical $E_{bending}$ value of 1 TPa was obtained, a value which reduced to 100 GPa for thicker tubes. Lateral and vertical bending of MWNTs, using an AFM probe to apply a known force, has also been used in the past to study CNTs (see Figure 2.1(c)). The first quantitative measurement of

Young's modulus of MWNTs using an AFM-based set-up was reported by Wong et al. [25] MWNTs were randomly dispersed on MoS_2 single crystals and pinned on one side to this substrate by deposition of an array of square pads. Nanotubes were deformed laterally by an AFM tip and lateral force–distance curves were acquired, which were in turn used to deduce the mean value for MWNT Young's modulus (~1.3TPa). Salvetat et al. [26] measured Young's modulus of isolated SWNTs, SWNT ropes and MWNTs produced using different methods as well as the shear modulus of SWNT ropes. Their technique involved measuring the vertical deflection of CNTs bridging holes on an anodized alumina template (see Figure 2.1(b)). Young's moduli of the order of 1 TPa for both isolated SWNTs and MWNTs (arc discharge grown) were reported, and no dependence of the mechanical response on the tube diameter was observed. However, they did observe that the mechanical properties of CNTs were dictated by the synthesis technique i.e. the extent of the degradation of the graphitic structure brought about by the introduction of defects during production.
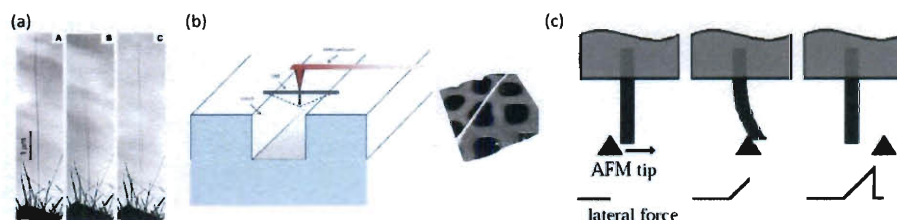
Figure 2.1 (a) Dynamic responses of an individual CNT to alternate applied potentials have been used in the past to ascertain mechanical properties. [24] (b) (Left) Schematic for typical AFM assisted bending experiment. The technique was used by Salvetat et al. [26] to study the mechanical properties of CNTs dispersed on nanochannel templates (Right image). (c) Schematic for an AFM based lateral bending experiment. [25]

The first measurements of the mechanical properties of CNTs via tensile testing relied on the application of axial strain using an AFM tip within a SEM chamber (see Figure 2.2(a)). [15] One end of each nanotube was attached to a rigid AFM cantilever, driven using a linear piezo-motor. The other end was attached to a compliant cantilever which acted as the load sensor. The technique was used to successfully test 7 MWNT specimens and their stress vs. strain curves were used to estimate MWNT Young's moduli (values ranging from 270 to 950 GPa were found). Examination of broken tubes revealed that nanotubes fractured via a 'sword-in-sheath' mechanism, wherein only the outer layer was found to be load-bearing (see Figure 2.3(a)). Also, an average bending strength of 14 GPa and axial strength values up to 63 GPa were observed for the arc discharge grown MWNTs. The authors were also able to measure the tensile properties of SWNT bundles using the same method they used for their MWNT study. [17] They observed Young's Moduli in the range 0.32-1.47 TPa and strengths between 10 and 52 GPa. Failure was found to occur only for the nanotubes on the perimeter of the bundle with the rest of the tubes simply slipping apart.

A more recent work described tensile testing of individual MWNTs within a transmission electron microscope using a MEMS material testing system (see Figure 2.2(b)). The usage of the MEMS device allowed the accurate measurement of both load and displacement simultaneously with TEM imaging. Load was applied using a thermal actuator on one side of the mobile testing stage, and displacement was measured using a MEMS differential capacitive sensor on the opposite end. The experimental measurements of single shell failure in

multiwalled carbon nanotubes displayed fracture strength values as high as 100 GPa and fracture strains that are very close to theoretical predictions. Young's Modulus values close to 1 TPa were reported. Interestingly, the authors also found that electron irradiation-induced crosslinking of multiwalled carbon nanotubes resulted in dramatic increases in sustainable loads. [16]
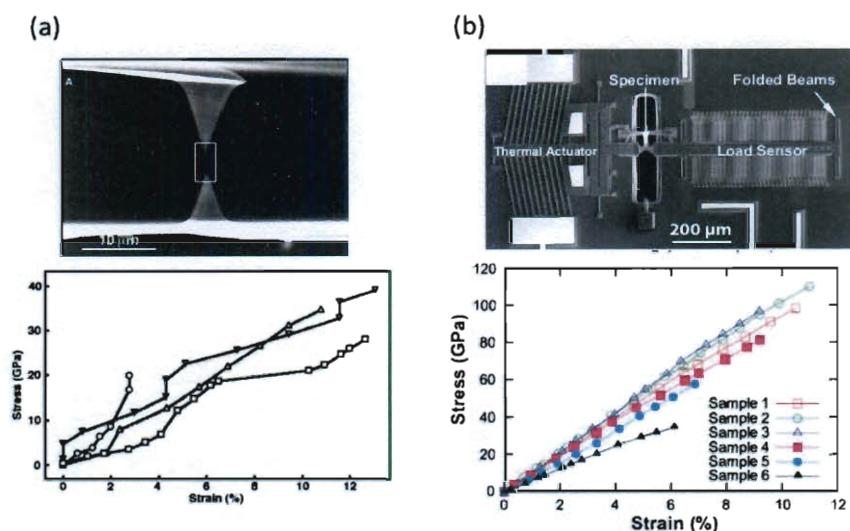
Figure 2.2 (a) The first direct mechanical tests on MWNTs were performed using AFM tips within a SEM chamber; test setup (top) and stress vs. strain curves obtained are shown (bottom). [15] (b) *In situ* testing on MWNTs were conducted recently using a MEMS based material testing system; test setup (top) and stress vs. strain curves obtained are shown (bottom). [16]

2.2. CNT-Matrix Interfaces: Properties and Characterization

Ever since the discovery of carbon nanotubes almost two decades ago, attempts have been made to incorporate them into matrices, especially polymers, in order to exploit their superior mechanical properties. The effective utilization of nanotubes in composite applications depends on the ability to disperse the

tubes homogeneously throughout the matrix without destroying the integrity of the CNTs. If the tubes are poorly dispersed, they tend to exhibit failure by separation from bundles or aggregates rather than failure by fracture. It also critically depends on the effectiveness of the interfacial stress transfer which in turn depends on the nature and strength of the nanotube/matrix interface.

There are three major modes of interaction between a CNT and a polymer matrix: chemical bonding, nano-mechanical interlocking, and non-bond interactions (e.g. van der Waals and electrostatic interactions; also, refer to Figure 2.3(b)). A perfect sp^2 hybridized carbon structure has a limited ability to form any sort of strong covalent bonds with a surrounding polymer matrix. However, on does need to bear in mind that this is somewhat dependent on the type of matrix used also, since there is some evidence that a few polymers, such as polyurethane and poly-(methylmethacrylate), chemically bond with pristine CNTs. [19, 20] A nanotube's interaction with any given polymer matrix can be improved via chemical modification of the tubes with functional groups. However, a disadvantage with modifying the hollow nanotubes by sidewall functionalization is that it changes the surface structure and breaks C-C bonds along the graphitic sidewall, and therefore affects the intrinsic properties of the nanotubes. Fortunately, non-disruptive chemical modifications such as wrapping of surfactants or DNA around the nanotubes or adsorption of aromatic structures onto their sidewalls can often be adopted to improve the level of chemical interaction at the interfaces. [21] Nano-mechanical interlocking is not easily achievable in nanotube composites due to the atomically smooth surface of a

CNT. There is, in fact, some evidence to prove that nanotubes slide relatively easily from a surrounding polymer matrix after full debonding from the matrix. [22] However, this might not be the case with nanotubes with twisted, uneven surfaces or mechanically deformed nanotubes with surface steps formed by gliding of dislocations. There have been conflicting studies pertaining to non-bond interactions, primarily based on theoretical models or simulations, especially with regard to their impact on adhesion at the interface.

As a result of the filler/matrix interactions, if there exists a strong adhesive force between the CNT and the matrix at the interface, an applied load (stress) on the composite could almost be completely transferred to the reinforcing nanotube (effective interfacial stress transfer). If the adhesion is weak, interface failure or de-bonding may occur at small loads, and the nanotubes could end up behaving as nanostructured flaws, introducing local stress concentrations and reducing the overall strength of the composite. While a weak interface between a nanotube and a matrix can be exploited to produce useful functionalities such as high mechanical damping or toughness (since nanotube slippage could create significant friction energy dissipation), it is generally desirable to have a composite with strong adhesion forces acting at the interface.

Reliable measurements of the strength of the interface between an individual nanotube and a surrounding matrix are difficult to make, given the small size of the nanotube and the lack of a robust testing platform that can be used to conduct nanoscale interfacial adhesion measurements. There are thus a number of indirect techniques that can be used to probe such interfaces. Data from

standard macro-scale tests performed on CNT-reinforced composite specimens can be analyzed using equations derived from standard composite theory in order to yield valuable information on the filler/matrix interface. M. S. P. Shaffer et al., [27] for example, conducted systematic tensile tests on catalytically grown MWNT-reinforced polyvinyl alcohol (PVA) thin films. The tensile elastic modulus of the composites was assessed using a dynamic mechanical thermal analyzer (DMTA) as a function of nanotube loading and temperature. The stiffnesses of the composites measured at room temperature were found to be only marginally better than that of the unreinforced polymer matrix. Based on their analysis of the test results using the Krenchel's expression for short-fiber composites, [28] the authors hypothesized that poor stiffness values were primarily due to imperfections in the graphitic layers of the catalytically grown nanotubes used, poor shear stress transfer between the shells of MWNTs under tensile axial loading, and excessive bending of tubes after dispersion into the matrix. M. Cadek et al., [29] on the other hand, obtained more encouraging results with their nanoindentation experiments on arc-grown MWNT-reinforced PVA and poly(9-vinyl carbazole) (PVK) composites. The Young's modulus and hardness of the composites were both found to increase by factors as high as 1.8 and 1.6 with the addition of 1 wt. % MWNTs in PVA and 2.8 and 2.0 with the addition of 8 wt. % MWNTs in PVK. The aforementioned values were subsequently plugged into the modified Halpin–Tsai equation for randomly oriented fibers [30] in order to compare the interfacial strengths of the two composites. The analysis showed that strong adhesion forces existed at the

interfaces in both composites with the interfacial bonding in MWNT/PVA composites being far superior to the one that existed in MWNT/PVK composites.

H. D. Wagner et al. [31] conducted tensile tests on MWNT/polyurethane/diacrylate oligomer thin films using an Instron apparatus and observed nanotube fragmentation within the composites after failure. By plugging in the average value for fragment length within the fractured specimens into a modified Kelly–Tyson model equation, [32] the authors were able to ascertain the stress transfer ability of the nanotube–polymer interfaces and found it to be of the order of 500 MPa, and thus, an order of magnitude higher than the stress transfer ability of some of the currently used advanced composites.
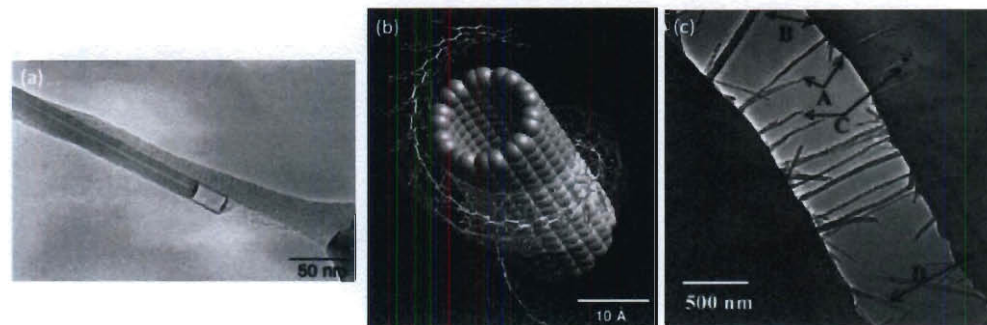
Figure 2.3 (a) Image shows "Sword-in-sheath" failure occurring after a MWNT was subjected to tensile stresses via electron irradiation. [33] This type of failure occurs due to the weak coupling between the outer and inner layers of the MWNT and can dramatically lower the effectiveness of load transfer in MWNT/polymer composites. (b) Cisoidal poly(phenylacetylene) (PPA) wraps perfectly around a (10,10) single-walled carbon nanotube, whose diameter precisely matches the accessible interior void of a PPA helix. |34| Polymer chain wrapping around nanotubes can improve interfacial strength significantly. (c) A TEM image showing crack propagation in MWNT/PS thin films induced by thermal stresses. The tube labeled B appears to have been pulled out of the matrix. The tubes labeled

A and D are nanotubes that broke between the crack faces. The tube labeled C broke at a defect site, which in this case is an iron catalyst nanoparticle. [35]

Both scanning and transmission electron microscopy can be used to visualize a CNT within a polymer matrix and qualitatively study factors such as nanotube dispersion and tensile fracture mechanisms as well as interfacial adhesion. Qian et al. [35] performed *in-situ* transmission electron microscopy deformation studies on MWNT/polystyrene (PS) composites, prepared by a simple solution-evaporation method, in order to shed some light on the tensile fracture mechanisms in such composites (see Figure 2.3(c)). The authors adopted a technique in which the TEM electron beam was condensed onto specific regions on a thin film of the composite, thus inducing local thermal stresses which in turn initiated cracks in the composite. Cracks were found to nucleate at low nanotube density areas and then propagate along weak nanotube–PS interfaces or relatively low nanotube density regions. The presence of nanotubes was found to be advantageous since they aligned perpendicular to the direction of crack propagation and bridged the crack faces in their wake, thus providing closure stresses across the crack faces. Only when the crack opening displacement exceeded ~800 nm were the nanotubes found to break and/or pullout of the matrix. P. Watts and W. Hsu performed similar experiments on MWNT-reinforced 2-methacryloyloxyethyl phosphorylcholine (2-(diethylamino) ethyl methacrylate diblock copolymer (MPC-DEA) composites. [36] Their observations were similar to the ones made by Qian et al., with a notable exception being that Watts and Hsu observed no tube breakage, either owing to the presence of a weak interface or to the fact that defect free arc discharge grown tubes were used in

their experiments as opposed to catalytically grown tubes. Examination, via high resolution microscopy, of nanotubes on fracture specimen surfaces can shed some light on the nature and strength of interfaces. Fragmentation of tubes, as observed by O. Lourie et al. [37] on the surface of SWNT/epoxy composite tensile fracture specimens, can provide some insight into the nature of load transfers occurring at interfaces. The presence of a polymer layer on a nanotube after fiber pullout can be considered an indication of a strong filler-matrix interface. C. Bower et al., for example, observed contact and adherence of polymer to most of the nanotubes examined on the surface of an MWNT/polyhydroxyaminoether composite fracture specimen. [38] On the other hand, poor wetting and no apparent sheathing of nanotubes by epoxy was observed from SEM micrographs of fractured surfaces of an SWNT/epoxy composite by P.M. Ajayan et al., [39] suggesting the existence of a weak interface.
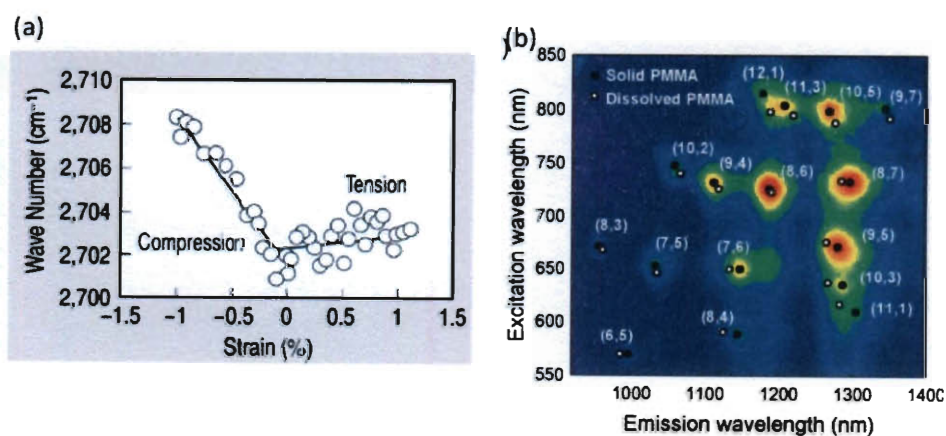
Figure 2.4 (a) The shifts in the second order A_{1g} Raman peak for MWNTs embedded in an epoxy matrix, as a function of strain in the composite; [40] (b) Fluorescence excitation–emission matrix of SWCNTs in a dried PMMA film. [41]

A number of spectroscopic techniques have also been used to study the properties of such nanocomposites at the interfacial regions. Micro-Raman spectroscopy can be used to qualitatively measure the effectiveness of load transfer in MWNT-reinforced composites because the second-order A_{1g} (disorder-induced) Raman peak position shifts with applied strain on the tubes (see Figure 2.4(a)). L. S. Schadler et al. [40] conducted macroscopic tensile and compression experiments on MWNT/epoxy resin composite specimens using standard testing procedures (American Society for Testing and Materials D638 and D695-91 tests) while simultaneously using Raman spectroscopy to monitor the strain on the tubes. The authors found the compression modulus of the composites to be higher than the tensile modulus and that load transfer to the nanotubes was much more effective in compression. The authors attributed the ineffective load transfer to the tubes during tension to weak coupling between the outer and inner layers of the multi-wall tubes and to poor interfacial adhesion (see Figure 2.3(b)). The second-order A_{1g} mode has also been found to shift with applied strain in SWNTs. P. M. Ajayan et al. [39] performed tensile tests on SWNT bundle reinforced epoxy composites and observed small shifts in the second order A_{1g} band upon loading. The authors inferred that the individual nanotubes were not significantly stretched upon application of axial tension due to sliding of the nanotubes out of bundles. Z. Jia et al. [19] successfully used infrared (IR) transmission spectroscopy to study the chemical bonds between nanotubes and PMMA in an MWNT/PMMA composite they synthesized by an *in situ* polymerization technique. The presence of a new peak in the IR spectrum of the composite at about 1,665 cm^{-1} was

considered as evidence for the existence of C-C bonds between the nanotubes and PMMA. Near-IR band gap fluorescence has also been used to study load transfer, strain, and interfacial adhesion limits in semiconducting SWNT-reinforced composites since spectral shifts are known to be proportional to strain in the tubes and marked deviations from linearity of the shifts can be interpreted as loss of nanotube-polymer adhesion and reveal slippage of individual nanotubes within the matrix. T. K. Leeuw et al. [41] used this technique recently to estimate the forces required to overcome adhesion at an SWNT/PMMA interface, the values for which were found to be between 1.5 nN and 6 nN.

It is worth noting that only a few of the aforementioned techniques provide any sort of quantitative information on the magnitude of the interfacial strength in such composites. Also, as all of them are indirect techniques, they are subject to numerous discrepancies. In 2002, C.A. Cooper et al. [22] reported on the usage of a scanning probe microscope (SPM) tip for drawing out individual MWNTs and SWNT ropes bridging across holes in a matrix. The lateral force exerted by the SPM tip on the tubes was resolved into its component parallel to the relevant direction in order to ascertain the nanotube-polymer interfacial shear strength. Tests on MWNT-epoxy composites showed that the interface strength decreased with an increase in the embedment depth of the nanotubes and that its values were significantly higher than those in conventional fiber-polymer interfaces; in some cases the interfacial strength value was as high as 376 MPa. The aforementioned technique was subsequently modified by A.H. Barber et al. [42] to perform single fiber pullout tests in order to measure the interfacial

strengths of MWNT/polyethylene-butene composites. Individual carbon nanotubes, attached to ends of AFM tips, were pushed into a molten polymer (thermoplastic). Following solidification of the polymer, the nanotubes were pulled away, with the forces required for pullout being recorded. Using a fracture mechanics based energy balance approach for data analysis, the authors were able to ascertain the interfacial fracture energy, G_c, for the system. For the pristine MWNT/polyethylene-butene system, the G_c values were found to lie between 4 J/m^2 and 70 J/m^2 (see Figure 2.5(b)). The authors postulated that the large interfacial strength values observed i.e. values comparable to those reported for engineering composite systems (see Chapter 5 and ref. 81,) were due to bonding of the tubes with the polymer via defects in their structure or due to the wrapping of polymer chains around the nanotubes. The authors performed a set of similar experiments within a SEM, comparing the interfacial strengths of chemically functionalized (carboxyl-modified) MWNT/epoxy composites to that of pristine MWNT/ epoxy composites (see Figure 2.5(a)). [43] The force required to pull each nanotube out of the polymer was seen to increase as the embedment depth increased, with chemically modified nanotubes showing correspondingly larger pullout forces when compared with pristine ones. Also, for both types of nanotubes, at relatively large embedment depths, the stress in the nanotubes was found to be large enough to break the nanotubes instead of pulling them out from the epoxy, with the modified nanotubes requiring smaller embedment depths for nanotube fracture. Both modified and, to a lesser extent, pristine nanotubes showed an increase in the average interfacial shear strength (IFSS) (equation for

calculating IFSS values can be found in Chapter 5) with embedment depth

decrease, a behavior consistent with classical shear lag theory. [44] Using the plot

of IFSS vs. nanotube embedment depth (see Figure 2.5 (c)), the authors

determined the shear lag constant, β, for the composites. β values for pristine and

modified nanotube-based composites (1.05×10^6 m^{-1} and 7.95×10^6 m^{-1},

respectively) were found to be orders of magnitude greater than those calculated

for larger single-fiber composites (1×10^4 to 1×10^5 m^{-1}), [45] indicating that

stress transfer might be much more efficient in nanotube/polymer composites than

in traditional fiber-based composites.
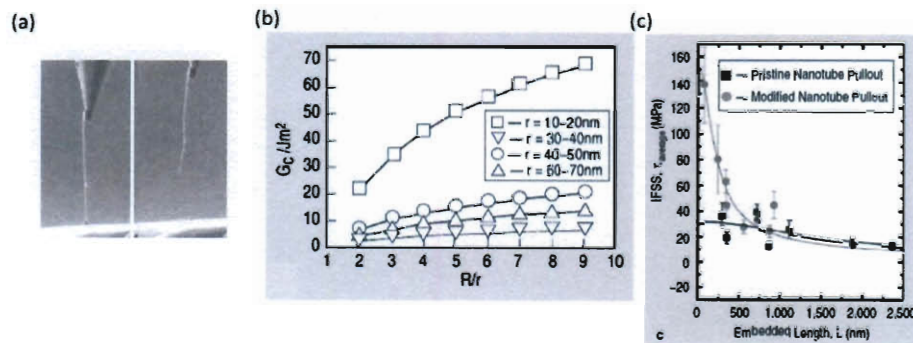
Figure 2.5 AFM probes have been used in the past to pullout MWNTs from polymer matrices. (a) MWNT attached to AFM tip before and after pullout. [43] (b) Results of the pullout experiments have been used to ascertain G_c as a function of stress transfer parameter R/r (see Chapter 5) [42] and (c) average IFSS values as a function of embedment depth. [43]

3. Development and Application of a Novel Technique for the Mechanical Characterization of Nanomaterials

3.1. Introduction

Metal nanowires, carbon nanotubes and other 1-D nanomaterials are of great technological importance due to their current and potential applications in miniaturized electronic, optical, thermal and electromechanical systems. It is crucial to acquire a thorough understanding of their mechanical properties at comparable length scales because of their well-known size effects – large deviation from bulk properties at small scales. In addition to the technological driving force, these one-dimensional nanoscale entities provide unique opportunities and challenges toward the investigation of fundamental mechanisms in materials science, primarily those governing the origin and transitions of size dependent mechanical behavior. Although it is possible to use theoretical analyses and numerical simulations in order to predict their mechanical behavior, experimental verification is still crucial to prove the validity of the theoretical and numerical predictions.

In situ nanomechanical testing provides a powerful means to study deformation processes and to observe the deformation mechanisms in nanomaterials through real-time imaging, for example, within an electron

microscope (SEM) chamber. As a result, a considerable amount of attention has been focused on *in situ* experiments such as piezo-driven MEMS based tensile testing [46], AFM assisted compression [47] and tension tests [17] and tests conducted using electrostatically and thermally actuated platforms [48]–[50], among others, in order to probe the mechanical properties of nanomaterials and thin films. A number of *in situ* mechanical testing techniques cannot be easily adapted for testing 1-D nanomaterials (e.g., the MEMS-based tensile testing technique for nanoscale thin films developed by Haque et al. [46]). A major drawback with methods involving atomic force microscopy is that the force applied on and the deformation of the specimen cannot be simultaneously and independently measured. Furthermore, the force measurement is often semi quantitative at best, since it is based on an estimate of AFM cantilever stiffness and also because it relies on AFM tip deflection monitoring. The electrostatically and thermally actuated platforms developed by Y. Zhu et al. [49] do overcome most of the limitations associated with some of the other aforementioned techniques. However, their technique relies on a complicated setup that involves separate microchips for sample loading and capacitance-based load measurement. Its implementation can thus be both expensive and challenging.

3.2. Electrostatically Actuated Testing Platform

Simple (comb drive based) electrostatically actuated MEMS platforms were fabricated with the intention of using them to perform *in situ* tensile testing experiments on nanomaterials within an electron microscope chamber. The devices, designed by Dr. Harold Kahn [50], consisted of a lateral comb-drive

actuator, fixed and movable pads, a Vernier scale, anchors and tether beams (see Figures 3.1 and 3.3). They were essentially designed to apply pure tension on a specimen with the help of a comb drive actuator and allowed one to study the mechanical properties, such as elastic modulus and tensile strength, of a specimen mounted across the pads.
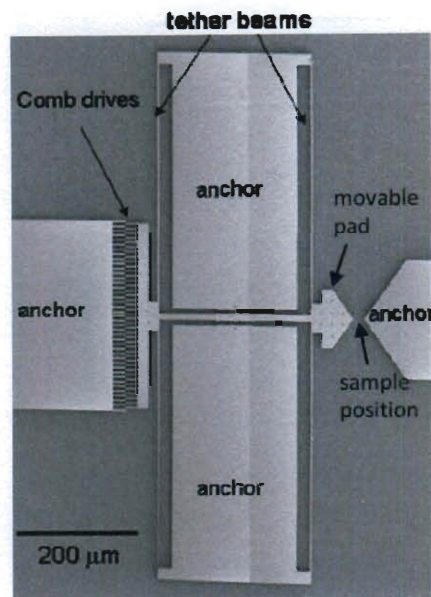
Figure 3.1 Electrostatically actuated mechanical testing platform. [50]

3.2.1. Device Fabrication

The devices were fabricated using standard polysilicon micromachining techniques on 4 inch bare Si wafers that were <100> oriented and boron doped (see Figure 3.2). The process adopted for device fabrication is as follows. Contaminants present on the surface of silicon wafers were first removed via adoption of RCA cleaning procedures. This is important in order to obtain high performance and high reliability semiconductor devices, and to prevent contamination of process equipment, especially the high temperature oxidation,

diffusion, and deposition tubes. A 1 μm thick thermal SiO_2 film was first grown on the surface (both faces) of the wafers. This step was carried out within an oxidation furnace at 1150 C for a period of 100 minutes. Subsequently, a 4μm thick phosphosilicate glass (PSG) film was grown on the surface of the wafers within a LPCVD chamber (deposition temperature ~ 400 C). The oxide films were then densified by annealing at 1100 C followed by B doped polysilicon film growth within an LPCVD reactor. SiH_4 and B_2H_6 gases acted as precursors for the deposition which occurred at 650 C and was carried out for 300 minutes in order to obtain 3 μm thick films. Polysilicon films formed on the back of the wafers were etched away before residual stresses measurements were conducted using a bow measurement system that used a capacitance sensor to measure curvature. The Stoney's equation (G. G. Stoney, 1909), which relates the residual stresses in thin films with their curvature, was used to estimate the residual stresses in the polysilicon films. The stresses were found to be in the order of a few hundred MPa, values that were considered reasonably low and capable of being relieved by thermal annealing. The wafers were thus annealed at 1100 C in a nitrogen atmosphere for 3 hours in order to relieve the residual stresses (step also improves the crystallinity and conductivity of the polysilicon films). Curvature and 4 point probe measurements post annealing showed an order of magnitude reduction in residual stresses and two orders of magnitude reduction in the resistivity (0.3 to 0.003 ohm cm). Standard photolithography techniques were subsequently used to pattern the devices on the wafers (see Table 3.3). The wafers were first (a) pre-baked, on a 115 C hotplate for 2 minutes in order to drive off moisture and

promote adhesion of photoresist to the substrate, (b) placed in a Hexamethyldisilazane (HMDS) fume tank for 3 minutes for photoresist adhesion promotion, (c) spin coated with Shipley's photoresist S1813 (3500 rpm for 30 seconds, this resulted in a photoresist layer of thickness ~4680 Å) and (d) soft-baked on a 105 C hot plate for 1 minute (step eliminated solvents from the photoresist, improved its adhesion to the substrate and also cured the photoresist thus preventing the substrates from sticking to the mask plate during the exposure). (e) Exposure was carried out using a MA 6 Karl Suss mask aligner (SUSS MicroTec AG, Garching, Germany). The intensity of the UV400 lamp had been set (by default) to 12+-0.1 mW/cm^2.The low vacuum mode was used for all exposures. After exposure, the wafers were (f) post exposure baked at 115 C for 1 minute (step minimizes the effects of standing waves & drives the acid-catalyzed reaction that alters the solubility of the polymer in many chemically amplified resists), (f) were placed in a tub with a 351 concentrate developer: deionized (DI) water 1:5 mixture for 30 seconds for photoresist development, (g) placed in a DI water rinsing tank for 5 minutes to stop the development and to remove excess developer and unexposed photoresist and (h) ashed within an Oxygen Asher which used an oxygen plasma to chemically remove photoresist and other organic compounds isotropically from the surface of substrates. The wafers were finally hard baked at 115 C for 30 seconds to remove any additional moisture and solvents, and harden the photoresist prior to etching. Deep reactive-ion etching (DRIE) was carried out to etch polysilicon devices on the wafers using a PlasmaTherm SLR-770 Inductively Coupled Plasma Reactive Ion Etcher

(Plasma-Therm, St. Petersburg, FL). DRIE is a highly anisotropic etch process used to create deep, steep-sided holes and trenches in wafers, with aspect ratios of 20:1 or more. A process known as the Bosch^{TM} process or time-multiplexed etching that alternated repeatedly between two modes, a nearly anisotropic plasma etch mode involving sulfur hexafluoride ions that attack the wafer from a vertical direction and a deposition mode that results in the coating of a chemically inert passivation layer of C_4F_8, was used for the etch. Etch time depended upon the exposed area of the wafers. 8 loops (each loop lasted for about 13 seconds) were sufficient to etch away ~3000 nm of patterned polysilicon (the etching process was monitored through a window on the plasma chamber; visual inspection was used to ascertain the time required to etch the polysilicon films since etch rate depends upon exposed area). After the etch step, the wafers were stripped of photoresist in an acetone bath and the devices were released in a 10:1 buffered oxide etch (NH_4F: HF 36.2:4.7 % by weight) solution bath. The duration of the release step was long enough for the movable portions of the device to be completely released while some of the oxide remained beneath the rectangular pads, leaving them attached to the substrate. The samples were then placed in a methanol bath and finally dried within a supercritical drier (Tousimis research corporation, Rockville, MD) via replacement of methanol by carbon dioxide, in order to avoid stiction issues.

Step 1- 5 μm thick oxide growth on wafer top

Step 2- 3 μm thick doped polysilicon growth on oxide film

Step 3- Photoresist coat on polysilicon layer

Step 4- Photoresist patterning

Step 5- Deep reactive ion etch of polysilicon layer

Step 6- Selective buffered oxide etch followed by critical point dry
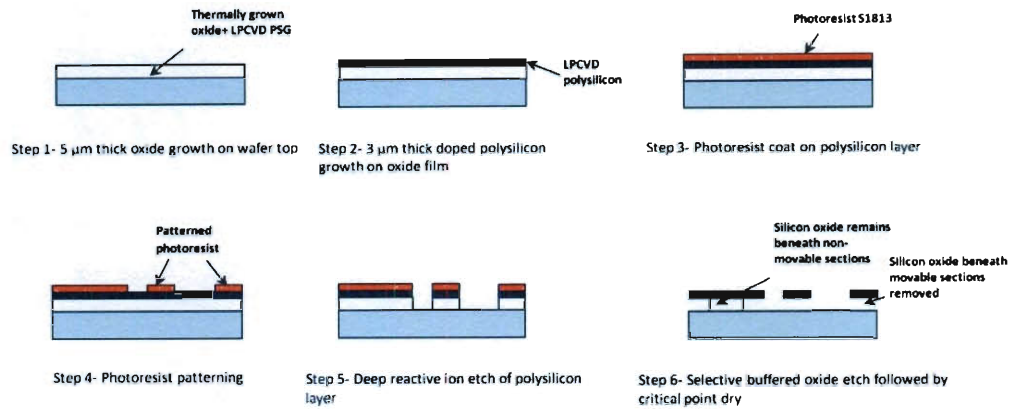
Figure 3.2 Schematic shows the procedure adopted for MEMS device fabrication. Note that the dimensions of the layers have not been drawn to scale.

3.2.2. Device Functioning

When a voltage, V, was applied between two sets of comb fingers, the capacitance, C (see Figure 3.3 (d)) increased as the movable fingers traverse a distance x, in the lateral direction, and increased the inter-finger overlap (see Figure 3.4). The resulting force, F, generated by electrostatic attraction was computed with the help of the following equation

$$F = \frac{1}{2}\frac{\partial C}{\partial x}V^2 = \frac{1}{2}\frac{N\varepsilon t}{d}V^2 \quad (1)$$

C was obtained from the equation

$$C = N\left[\frac{\varepsilon(x + x_0)t}{d} + C_p\right] \quad (2)$$

where N is the number of fingers, ε is the permittivity of the medium between the fingers, t is the thickness of the fingers, x_0 is the initial lateral overlap of the fingers, C_p is the fringe capacitance and d is the gap spacing between the fingers. This electrostatic force was sufficient to move the central portion of the device, including the movable part of the Vernier scale and the movable pad. Sample

elongation/ movable pad displacement was measured using the Vernier scale incorporated on the device. The force generated by the comb-drive actuator was ascertained by inputting the voltage application- movable pad displacement response data for the device in the absence of a mounted specimen into a finite element model (see Figure 3.5). The devices were used to conduct a few preliminary tensile tests on Ni nanowires within a SEM chamber. They possessed the capability of applying forces in the order of a few hundred nN to a few µN, depending on the applied voltage. However, in order to obtain sample elongation data one had to rely on electron microscope images of the Vernier scales (insufficient resolution). Stiction between the devices and the substrate as well the fragility of the tether beams were some of the other issues that hindered their operation and their usage was hence slowly phased out.
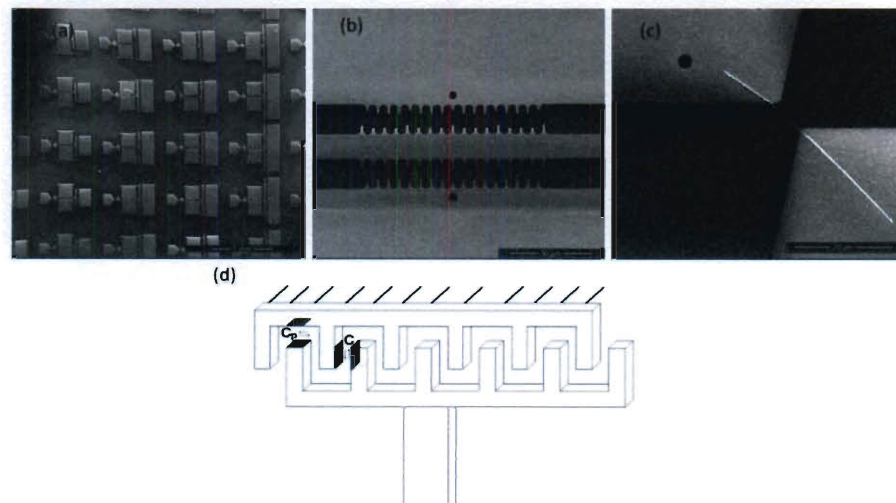
Figure 3.3 (a) SEM image shows electrostatically actuated platforms on a Si wafer. (b) SEM close up view of Vernier scale. (c) A single Ni nanowire placed across the testing platform. (d) Schematic shows fingers of a comb-drive actuator.
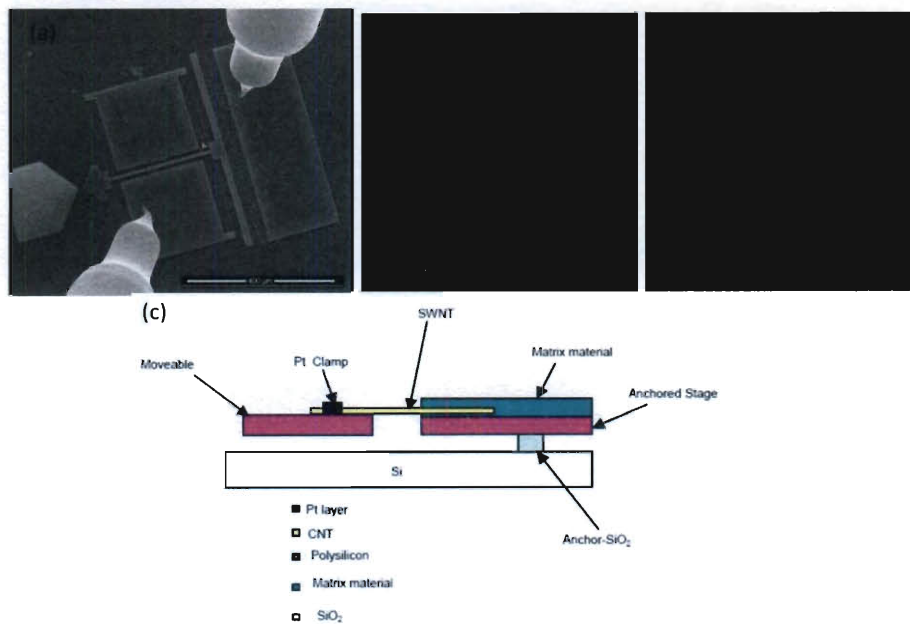
Figure 3.4 (a) Electrostatically actuated platforms were actuated by application of a bias with the help Zyvex™ nanomanipulator probes within a SEM chamber. (b) Optical microscope images of comb drive actuator (left) before and (right) after voltage application. (c) Single fiber pullout experiments (see Chapter 5) can also be performed using the platform by following the outlined scheme
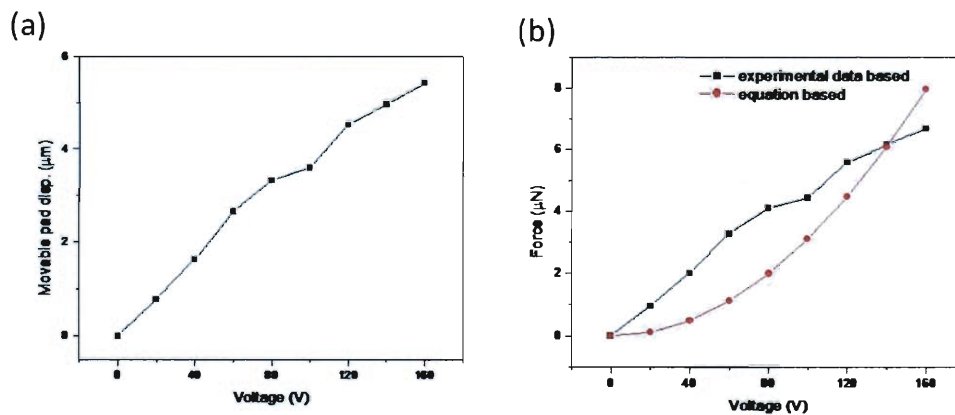
Figure 3.5 Comb-drive actuator (70 fingers) voltage response. (a) Movable pad displacement as a function of applied voltage, deduced from SEM image correlation; (b) Force generated by comb-drive actuator as a function of applied voltage, as deduced from (black curve)

actual experiments in conjunction with finite element analysis and (red curve) from equation (1).

3.3. Nanoindenter actuated testing platform

Nanoindentation is a mechanical property measurement technique that involves the mechanical probing of a material surface to nm-scale depths, while simultaneously monitoring load applied and depth penetrated (displacement). The unloading part of the load-displacement curve can be used to determine the hardness and elastic modulus of a material using equations developed by W. C. Oliver and G. M. Pharr (see Figure 3.6). [51] The nanoindentation test can also be used to assess the fracture toughness, yield strength, scratch resistance and wear properties of the probed material. The nanoindenter, the primary instrument used for conducting a nanoindentation experiment, generally consists of a diamond tip (head) that relies on an electromagnetic actuator for force generation and a capacitance gauge for displacement measurement. Nanoindentation, as a technique, has gained a considerable amount of popularity over the past few decades owing to the development of advanced machines that can record small loads and displacements with high accuracy and precision. Nanoindenters, such as the Agilent ^{TM} G200, possess a theoretical displacement resolution of 0.2 pm and a load resolution of about 1 nN (see Table 3.1).
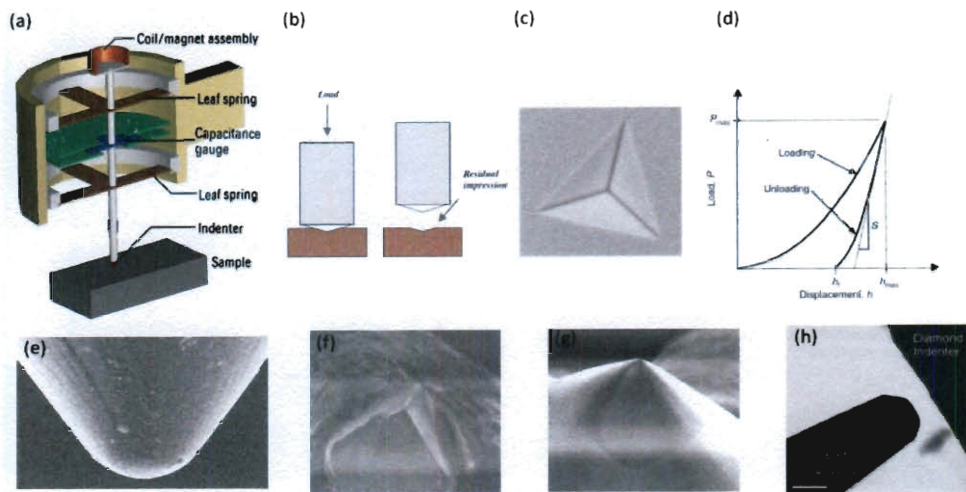
Figure 3.6 (a) Schematic shows the components of an Agilent^{TM} G200 nanoindenter and (b) geometry of a nanoindentation experiment. (c) Residual impression left on a surface after nanoindentation using a Berkovich nanoindenter tip. (d) Ideal load vs. displacement curve for a nanoindentation experiment. [51] SEM images of some of the common types of tips used for nanoindentation viz. (e) spherical, (f) cube corner, (g) Berkovich and (h) flat punch respectively.

1-D nanomaterials such as Ag and GaN nanowires and ZnO nanowires and nanobelts have been probed via nanoindentation in the past. [52] However, such experiments are difficult to perform and their results are often extremely challenging to interpret (the Oliver-Pharr method [51] of modeling contact area is not considered valid for such systems) owing to the size scales of the samples probed. Tensile experiments would be preferred for studying such materials since they result in the application of a homogeneous stress state and are less sensitive to boundary conditions, easing interpretation of experimental data. [53] Since, most nanoindenters, by themselves, cannot be easily adapted to conduct tensile experiments, we designed and fabricated a novel mechanical device that operates via a "push-pull" mechanism and converts a compressive nanoindentation force to

uniaxial tension that acts across a nanoscale specimen. It must be noted that similar schemes have been explored in the past in order to study the mechanical properties of brittle materials (referred to as the Theta sample [54]) and to measure the intrinsic strain in thin films. [55]
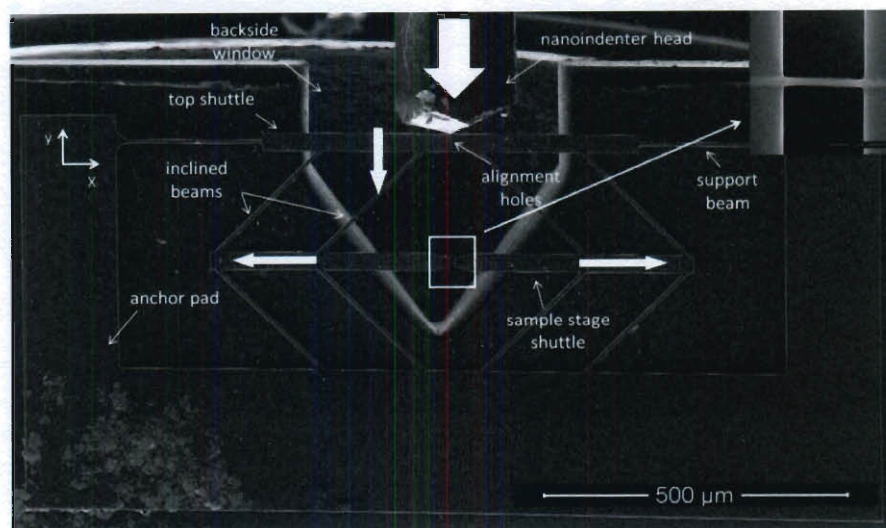
Figure 3.7 SEM image showing the novel micro-device (Generation II) and the indentation geometry; block arrows show the direction of movement of the indenter tip (Berkovich) and the shuttles during the experiment. The edge of the devices were coated with Ag paint (visible at bottom left corner of image) in order to avoid charging issues within SEM. The devices were mounted onto aluminum SEM stubs using Ag conductive epoxy layers (visible in the backside window region). (Inset) close up view of a nanowire sample mounted across the sample stage shuttles; scale bar reads 2 μm.

The device essentially consists of a pair of movable (sample-stage) shuttles that are attached to a top shuttle via inclined freestanding beams. Its actuation involves the usage of a nanoindenter (in our case the Agilent InSEM^{TM} nanoindenter, an Agilent Nano Indenter G200^{TM} based system capable of functioning within an SEM chamber) that applies a force on the top shuttle of the device along the y-axis (see Figures 3.7 and 3.8). Four sets of inclined

symmetrical beams transform the motion of the top shuttle into a 2-D translation of the sample-stage shuttles. Proper alignment of the nanoindenter head results in the sample-stage shuttles moving symmetrically and ensures that the load being applied across the sample, clamped between two ends of the sample-stage shuttles, is purely tensile. The displacement and load resolution of the devices are dictated by that of the nanoindenter (8.675 angstroms and 69.4 nano-newtons; load resolution = displacement resolution x spring constant of instrument); these values were ascertained via noise floor estimation experiments (see Figure 3.8(a)). With regard to stress versus strain curve extraction, the force applied on and the elongation of the test specimen can be extracted from the nanoindenter load and tip displacement data via either a) finite-element-analysis (FEA) based conversion factors or via b) response subtraction (see Chapter 4). While the former technique was found to be primarily applicable for analyzing tests conducted on linear elastic (brittle) materials the latter technique was found to be suitable for all kinds of materials.

Device stiffness depends upon the thickness of the device layer, the number of support beams attached to the top shuttle, and the number and inclination angle of the inclined beams. Two separate sets of devices were fabricated using standard silicon micromachining techniques. The first set of devices, referred to as generation I devices, were fabricated on silicon-on-insulator (SOI) wafers having a device layer thickness of 9.5 ± 0.5 μm (see Figures 3.9 and 3.11). For this generation of devices, the more compliant structures were composed of eight inclined beams at an angle of 45 degrees with

respect to the sample-stage shuttles. The stiffer structures had either eight inclined beams making a 60 degree angle or 20 inclined beams making a 45 degree angle with respect to the sample-stage shuttles. The second set of devices, henceforth referred to as generation II devices, were fabricated on SOI wafers having a device layer thickness of 6 ± 0.5 or 9 ± 0.5 μm (see Figures 3.10 and 3.11). Each of these devices comprised eight inclined beams making an angle either 45 degrees (more compliant) or 60 degrees (stiffer) with respect to the sample-stage shuttles. The generation II devices also differed from the generation I ones with regard to the width of the shuttles, the separation between the inclined beams, and the shape of the sample stage shuttles (see Figure 3.15). Since testing stage size has always a critical issue when setting up *in situ* nanomechanical characterization experiments within an electron microscope chamber, a fabrication scheme was adopted that involved the incorporation of dicing lines onto the photolithography masks such that individual devices could be isolated from the wafers onto either 3 mm × 2 mm (generation I) or 2.5 mm × 1.2 mm (generation II) pieces. Also, an extended back-side window was incorporated into the design to facilitate nanoindenter head positioning and to ensure device electron-beam transparency (a necessity for *in situ* TEM experiments; see Figure 3.12).

Table 3.1 InSEM^{TM} nanoindenter specifications

Parameter	Range	Resolution
Load	0-10mN	1 nN
Displacement	30 μm	0.2 pm
Extension axis	200 mm	35 nm

(a)   (b)   (c)
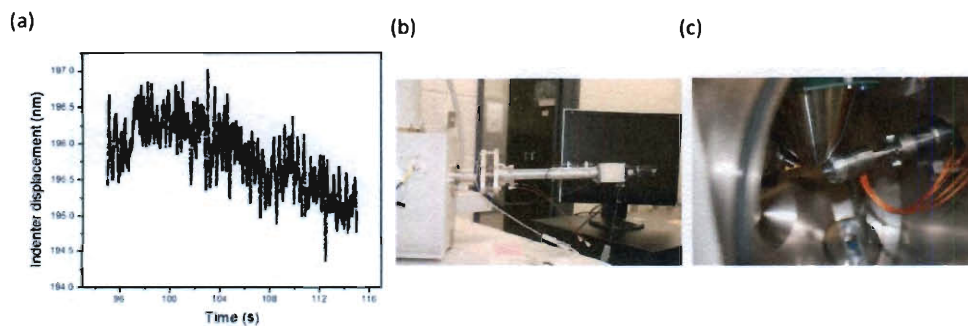
Figure 3.8 (a) Indenter *de facto* resolution values were determined via noise floor measurements. In order to determine the displacement noise floor of the nanoindenter, an indentation load of approximately 8mN was applied on a fused silica specimen for a period of 45 sec. The test method was configured with a fast displacement time constant and a data collection rate of 500Hz. The data collected during the last 20 seconds of the hold period was analyzed to determine the peak-to-peak displacement fluctuation, whose average value was assumed to be equal to the displacement resolution. Peak to peak displacement fluctuation is plotted in figure. (b) Images show InSEM^{TM} indenter extension axis and (c) nanoindenter module within SEM chamber.
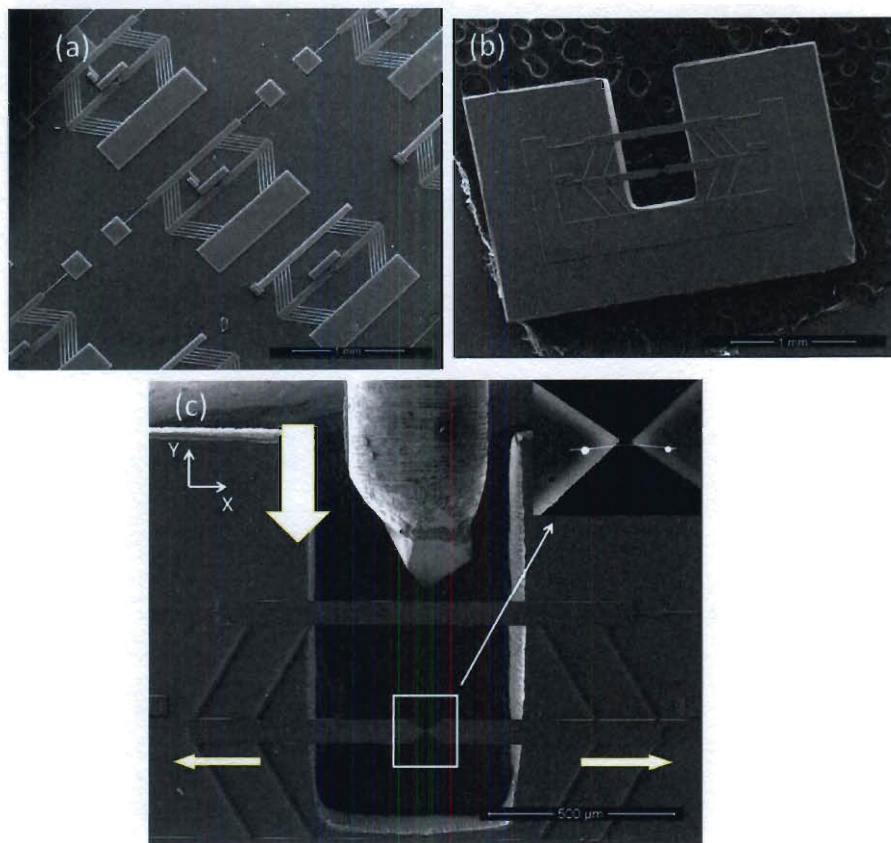
Figure 3.9 (a) SEM image shows generation I micro-device prototypes (polysilicon) fabricated on a Si wafer. (b) SEM image of a generation I micro-device. (c) SEM image shows generation I micro-device and the indentation geometry (a cube corner nanoindenter tip was used to perform the experiments).
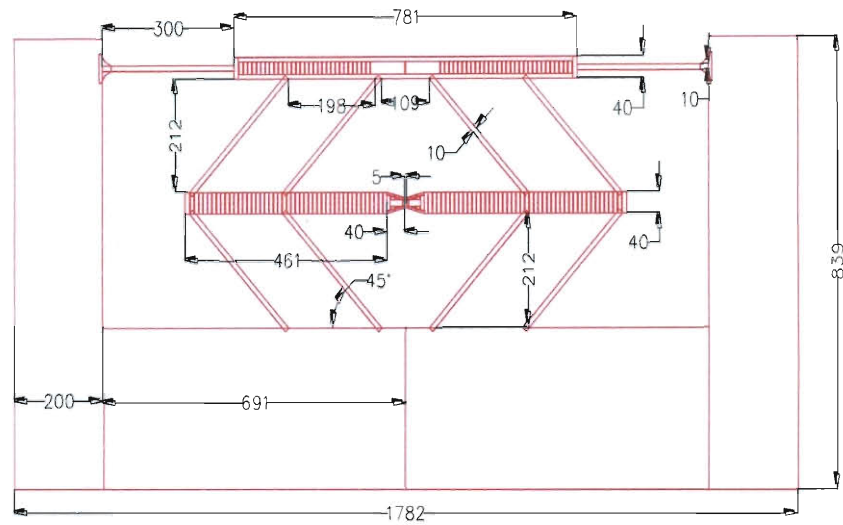
Figure 3.10 AutoCAD drawing of generation II micro-device (Note that sample stage shuttle gap could either be 5 or 2 μm). All dimensions indicated are in μm. Device geometry shown above (same as one shown in Figure 3.7) was used for all the experiments discussed in this thesis.
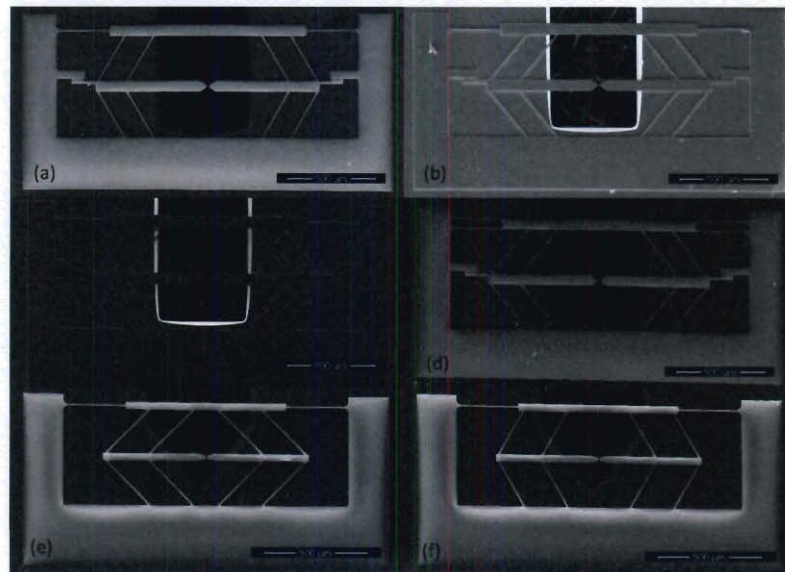
Figure 3.11 Scanning electron microscope images showing geometric variations of the novel microdevice; devices labeled (a) to (d) belong to generation I while devices labeled (e) and (f) belong to generation II. The devices labeled (a) and (f) are comprised of inclined beams

making a 60^0 angle with the sample stage shuttles. The rest of the devices have inclined beams making a 45^0 angle with respect to the sample stage shuttles.
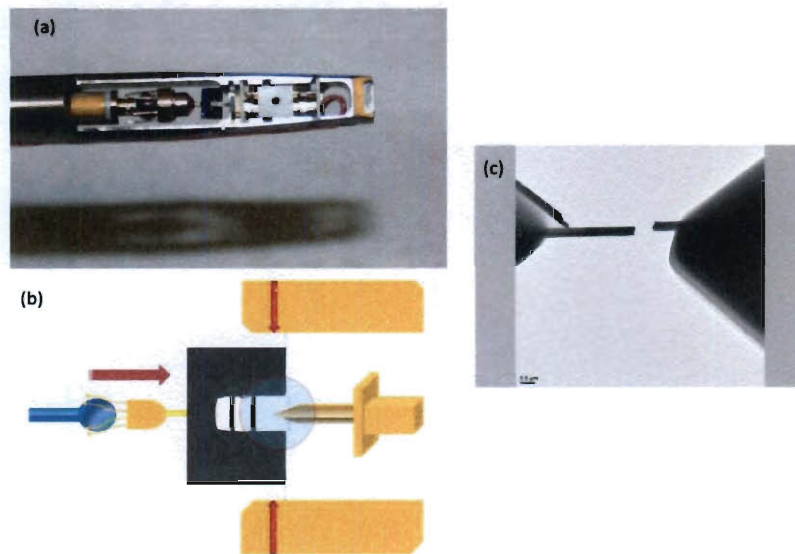
Figure 3.12 The micro-device can also be used to perform experiments within a TEM chamber. (a) Image shows device mounted on a Nanofactory™ TEM nanoindenter sample stage. (b) Schematic shows indentation experiment geometry. (c) TEM image of a Ni nanowire after tensile testing experiment was conducted upon it.

Table 3.2 Comparison of novel technique with AFM tip assisted tensile/single fiber pullout techniques

Novel nanoindenter assisted MEMS based tensile/interface testing	AFM tip assisted tensile/interface testing
Direct and independent (of imaging technique) application and measurement of loads and displacements (using nanoindenter) allowing real-time observation of deforming samples	Load and displacement measurements rely on the sample imaging technique
Nanoindenter controlled application and measurement of forces and displacements with nN and nm resolution (69.4 nN and 0.87 nm)	Piezo motors generally used to apply a displacement. Measurement of forces and displacements dependent upon experiment imaging technique (low resolution for SEM based experiments; very high resolution for TEM based experiments)
Use of quantitative nanoindenter minimizes errors	Extraction of force signal from cantilever stiffness can result in errors because of uncertainties in determination of the cantilever dimensions and material constants
Misalignment issues are minimal owing to design; also misaligned samples can be easily detected and discarded	Nanomaterials must be attached to the side of AFM tips (rather than the end) at an angle to the vertical axis. Also, a natural deviation from the vertical direction occurs during loading of the cantilever-tip assembly
Micro- devices are reusable	AFM tip assembly can also be reused
With regard to experiments conducted within SEM, specimen post failure analysis is facile; devices can be easily mounted onto TEM grids for imaging	AFM tips cannot be mounted onto TEM grids easily
With regard to single fiber pullout experiments, embedded depths can be controlled (to a certain extent) and measured easily	Embedded depths cannot be controlled or measured easily
With regard to single fiber pullout from polymer matrices, the technique allows for the facile implementation of desired processing steps e.g. high temperature cures & post-cures	Desired polymer processing steps cannot be easily implemented

3.3.1. Device Fabrication

As previously stated, device fabrication involved standard silicon microfabrication techniques and was tailored in order to obtain stand-alone devices on mm scale pieces with extended back-side windows (see Figures 3.13 and 3.14). Standard silicon on insulator (SOI) wafers were used for the fabrication. The first generation device wafers consisted of a 9.5 ± 0.5-µm-thick Si (<100> oriented) device layer, a 2-µm thick buried oxide layer and a 490 ± 10-

μm-thick handle Si layer. The second generation devices consisted of a 6 ± 0.5 μm/9 ± 0.5 μm-thick Si (<100> oriented) device layer, a 5-μm-thick buried oxide layer (a thick oxide layer was used in order to avoid stiction issues), and a 490 ± 10-μm-thick handle Si layer. A bright field mask (device mask) was used for device patterning, while a dark field mask (trench mask) was employed to incorporate backside windows on the devices and for dicing lines to facilitate individual device isolation. First, a 4-μm-thick oxide film was grown on the back of the wafers by plasma-enhanced chemical vapor deposition at 340 C, with SiH_4 and O_2 gases acting as the precursors. This oxide layer would act as a mask for subsequent etching of the wafer handle layer. Standard photolithography techniques were then employed followed by a DRIE step, that involved the usage of the Bosch™ recipe, in order to pattern devices on the front side of the wafers (refer to Section 3.2.1 for details). Subsequently, photolithographic techniques were again used to pattern dicing lines and windows on a thick resist layer (Shipley's S1818) coated on the back side of the wafers (see Table 3.3). Mask alignment, during this step, was performed using a SUSS MicroTec MA-BA-6 Mask Aligner equipped with front-to back alignment capability (since the devices patterned on the device layer needed to be aligned with the backside windows and dicing lines). The oxide layers on the back side of the wafers were then patterned by immersion into a 10:1 buffered oxide etch solution for an appropriate period of time. Before the sample was immersed into the 10:1 buffered oxide etch solution, the front side of the wafers were coated with a thick photoresist layer in order to protect the exposed buried oxide layer. The handle layers were subsequently dry

etched within the DRIE etcher. The thick photoresist layers on the front sides were removed using acetone before device release. Device release involved the placement of the wafers in the 10:1 buffered oxide etch tank for a specific period of time. The duration of the release step was long enough for the movable portions of the devices to be completely released while some of the oxide remained beneath the anchor pads, leaving them attached to the substrate. The samples were then placed in a methanol bath and subsequently dried within a supercritical drier.

Table 3.3 Parameters used for Optical Photolithography (' indicates minutes while " indicates seconds)

Step	S1818 (wafer handle patterning)	S1813 (device patterning)
Pre-bake	2'	2'
HMDS vapor tank	4'	3'
Spin coating	3000 rpm, 30" (2.15 μm thick resist layer)	3500 rpm, 30" (1.4 μm thick resist layer)
Soft bake	5' 30"	1'
Exposure	8" (soft contact, 100 μm Al)	5" (low vacuum, 25 μm gap)
Post-bake	1'	1'
Developer tank	30"	30"
Water tank (develop stop)	2'	2'
Ashing	2'	2'
Hard bake	1'	1'
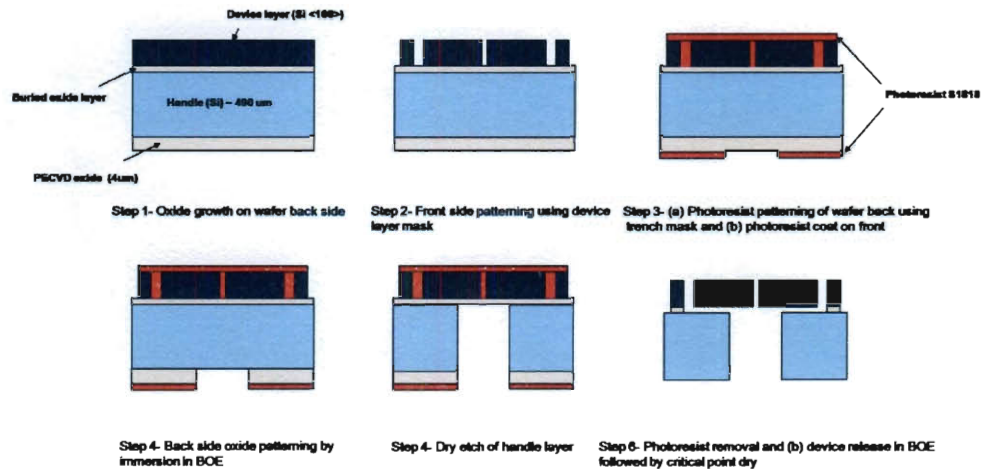
Figure 3.13 Schematic shows the procedure adopted for micro-device fabrication on SOI wafers. Note that the dimensions of the layers have not been drawn to scale.
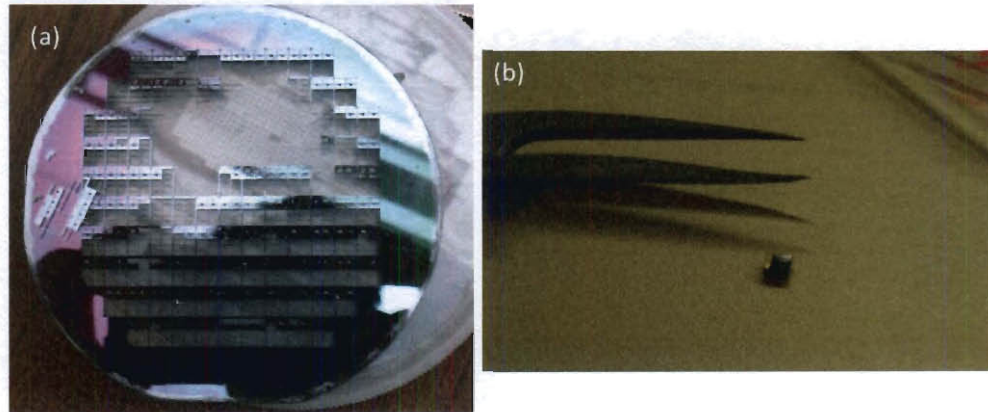
Figure 3.14 (a) Image shows a typical micro-device wafer (after removal of majority of micro-devices); (b) Image of a typical micro-device.
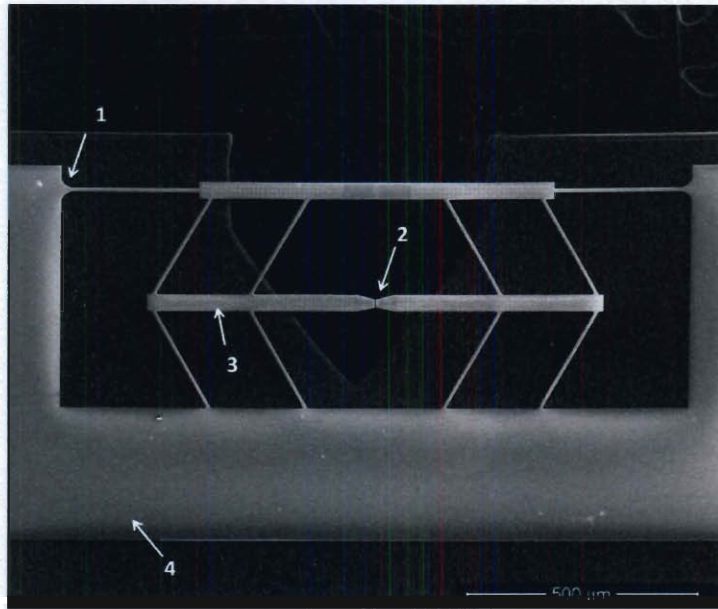
Figure 3.15 Micro-device design features (Generation II). (1) Fillets, at the ends of the support beams, help avoid stress concentrations. (2) Generation I devices were designed with triangular sample stage shuttle ends adjacent to the sample gap. Generation II devices were designed with trapezoid ends (increase area available for sample positioning thus allowing device reuse). (3) 2 μm holes on the movable shuttles facilitate device release. (4) Large area anchor pads were designed in order to prevent devices from getting released entirely from the substrate.

3.3.2. Sample Preparation: Ni Nanowires

The first set of tensile testing experiments, using the novel technique, was conducted on Ni nanowires. The Ni nanowires were synthesized within the channels of an anodized aluminum oxide (AAO) template via electrodeposition. [56] The anodized alumina template synthesis technique and the electrodeposition technique used are outlined below (see Figures 3.16 and 3.17). Prior to anodizing, a commercial aluminum sheet was degreased in acetone and electropolished in a 2:2:4 wt % solution of phosphoric acid: sulfuric acid: distilled water for 1 min.

Two step anodization was carried out at 40 V in a 0.2 M oxalic acid (or sulphuric acid) solution bath at 18 C for about 30 hours. The oxide film was then stripped by immersion into an aqueous mixture of phosphoric acid (6 wt. %) and chromic acid (1.8 wt. %) at 60 C. A second anodization was performed for shorter period (depending on the desired thickness of the nanochannel template) under the same conditions. Finally, the pores on the template were widened by immersion into an aqueous 0.1M phosphoric acid for fixed period of time. Room temperature cathodic electrochemical deposition was carried out at 1-3 V for 2-5 hrs using a $NiSO_4$ + $NiCl_2$ mixture solution as the electrolyte in order to obtain the nanowires. The templates were dissolved in a NaOH solution in order to extract the nanowires.
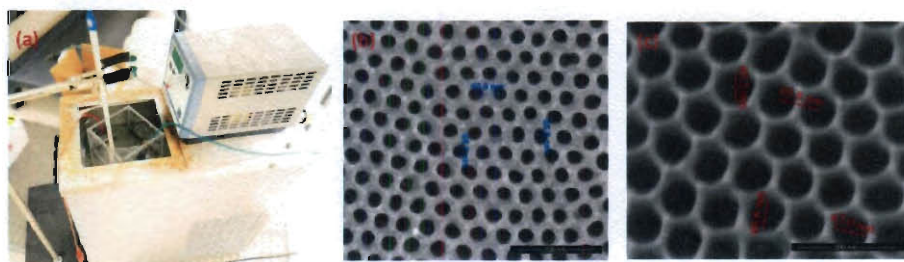
Figure 3.16 (a) Setup for AAO deposition. (b) Top view of AAO template synthesized using H_2SO_4 as the electrolyte (average pore diameter ~ 30 nm). (b) Top view of AAO template synthesized using $H_2C_2O_4$ as the electrolyte (average pore diameter ~ 60 nm).

3.3.3. Sample Positioning: Ni nanowires

Sample positioning refers to the placement of a 1-D nanomaterial at a desired location on the device with micrometer resolution. The fact that the specimens must be freestanding, clamped at both ends, and well aligned in the tensile direction makes sample positioning and clamping quite a challenging task. A novel scheme was adopted in order to mount Ni nanowires on the device for

testing (see Figures 3.18 and 3.19). First, a portion of each sample-stage shuttle was coated with a thin layer of epoxy (HARDMAN Water-Clear Epoxy). A droplet from a nickel nanowire suspension was then dispersed in isopropanol by ultrasonication for 5–10 min. A drop of this dispersion was deposited on a Si wafer coated with a 50 nm thick layer of titanium. Individual nanowires, ~15 μm long and 200–300 nm in diameter and, hence, visible under an optical microscope, were subsequently "picked up" and placed across the shuttles using micromanipulators housed within a probe station (The Micromanipulator Company, Carson City, NV). Tungsten tips (model 7F, The Micromanipulator Company, Carson City, NV) were used to perform the manipulation of the nanowires, since the wires were found to attach to the tips via possibly van der Waals' forces or surface charging induced electrostatic and frictional forces. The epoxy layer, upon hardening, clamped the tensile specimens onto the devices.
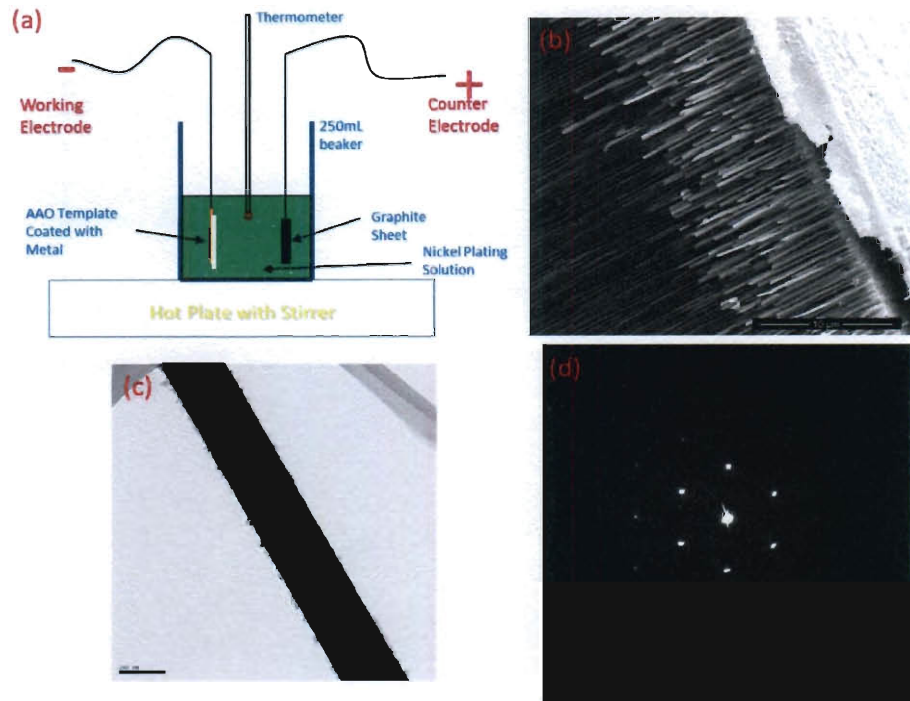
Figure 3.17 Ni Nanowire synthesis. (a) Setup for Ni electrodeposition; (b) anodized alumina template with Ni nanowires; (c) TEM image of Ni Nanowire (scale bar reads 200 nm); (d) Selected Area Diffraction analysis showed that the nanowires were single crystals and grew along the <112> direction.
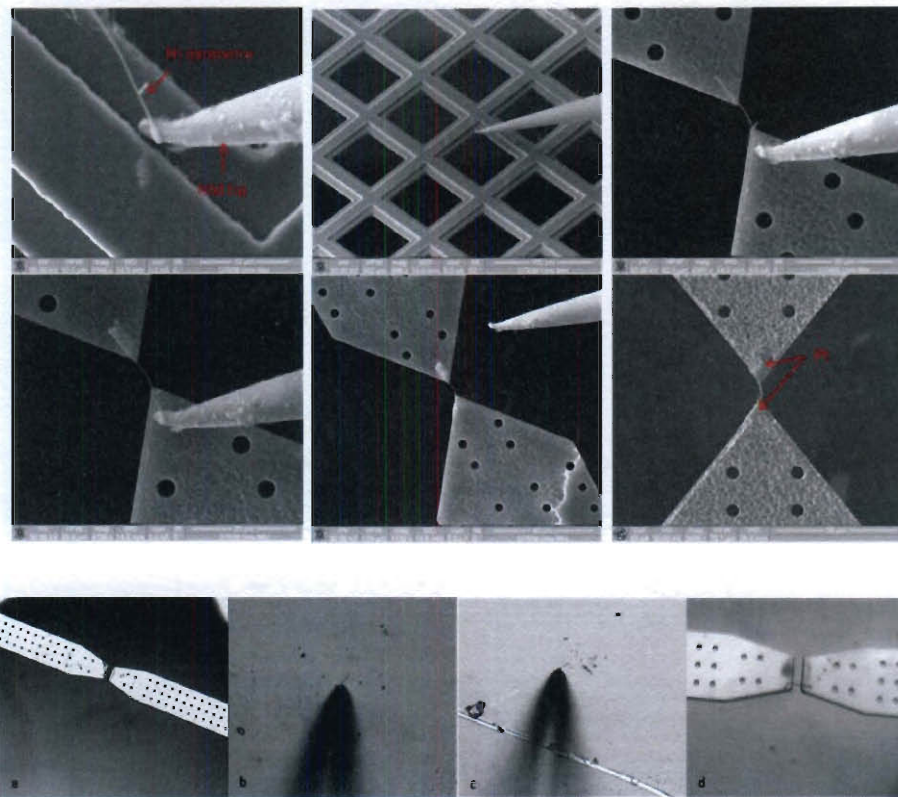
Figure 3.18 (Top set) SEM images show a Ni nanowire as it gets manipulated and clamped onto the micro-device. This procedure was performed within a SEM-FIB equipped with a micro-probe (nanomanipulator) and a gas injection system (for Pt deposition). Owing to its tedious nature, this procedure for tensile specimen preparation was quickly abandoned. (Bottom set) Optical microscope images show the procedure that was developed for the manipulation and clamping of individual nanowires (and nanotubes). (a) The ends of the sample stage shuttles were coated with a thin layer of epoxy (HARDMAN Water-Clear Epoxy). (b) Using micromanipulators housed within a probe station, a tungsten tip was brought into contact with an individual nanowire. (c) The nanowire, which was found to easily adhere itself to the tip, was subsequently placed across the gap between the sample stage shuttles. (d) The epoxy layer generally tends to coalesce around the nanowire thus attaching it to the sample stage shuttles.
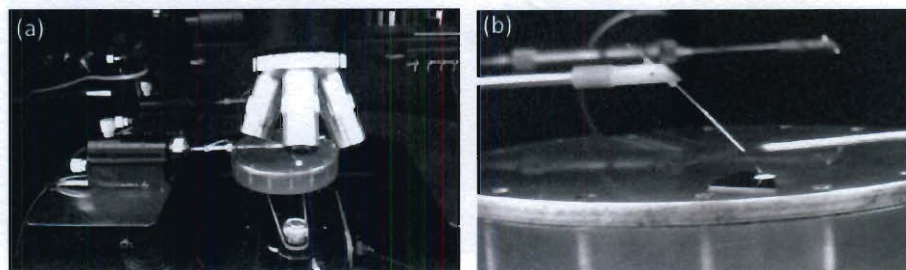
Figure 3.19 (a) Image shows micromanipulators housed within a probe station (The Micromanipulator Company, Carson City, NV). (b) Close up image shows one of the tungsten tips that were used for all the nanowire/nanotube manipulations discussed in this thesis.

3.3.4. Functioning of Nanoindenter Actuated Testing Platform

The tensile testing experiments on the Ni nanowires were performed within a SEM (FEI Quanta 400 high-resolution field emission SEM, FEI Company, Hillsboro, OR) equipped with an InSEM^{TM} Indenter (Agilent Technologies, Oak Ridge, TN) system (see Figure 3.7). A blunt berkovich nanoindenter tip was used to perform the indentation. 9 ± 0.5 µm thick devices with eight 45° inclined beams attached to the sample-stage shuttles were used for all the tensile experiments. The nanoindenter tip was first aligned with the top shuttle of the device in order to make sure that the sample-stage shuttles moved symmetrically. This was done with the help of alignment holes that had been incorporated in the device design (see Figure 3.24 (a)). Note that the alignment along the z axis (see Figure 3.7) relies on the observation of the shadow of the top shuttle on the indenter tip. Once the indenter head alignment was completed, the electron beam was focused on the nanowire specimen in order to monitor its deformation as a function of load. The indentation was performed in the load-controlled mode (the experiment can also be performed in a quasi-displacement

controlled mode), with the loading rate being held at a constant value of 30 μN/s (for the nanowires, this corresponds to a strain rate of approximately 0.007/s) (see Figures 3.20 and 3.21). Nanoindenter head load & displacement data were collected at the rate of 25 Hz. The maximum load applied on the device was 2 mN. Once this value was reached, the load was held constant for 0.5 s; this was followed by an unloading step at the aforementioned rate (see Table 3.4). A thermal drift correction hold step was performed for about 50 s in order to account for small amounts of thermal expansion or contraction in the test material and/or indentation equipment.

Table 3.4 Table 3.4: Nanoindentation experiment specifications

Parameter	Value
Allowable drift rate	0.05 nm/s
Poisson's Ratio	0.18
Surface approach sensitivity	5%
Data Acquisition rate	25 Hz
Displacement rate/load rate	10nm/s / 30 μN/s
Load rate multiple for unload rate	1
Maximum load	Variable (0.1 -2 mN)
Number of times to load	1
Peak hold time	0.5 s
Percentage to unload (before thermal drift step)	99-99.9%
Surface approach distance	1000 nm
Surface approach velocity	50 nm/s
Time to load	inconsequential
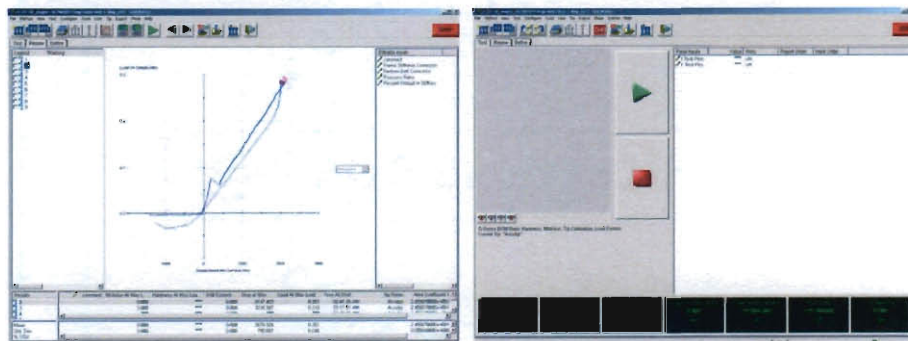
Figure 3.20 Testworks™ 4 was the software used for nanoindenter control. (Left) Figure shows the Testworks™ results review interface and (right) Testworks™ nanoindenter control interface.
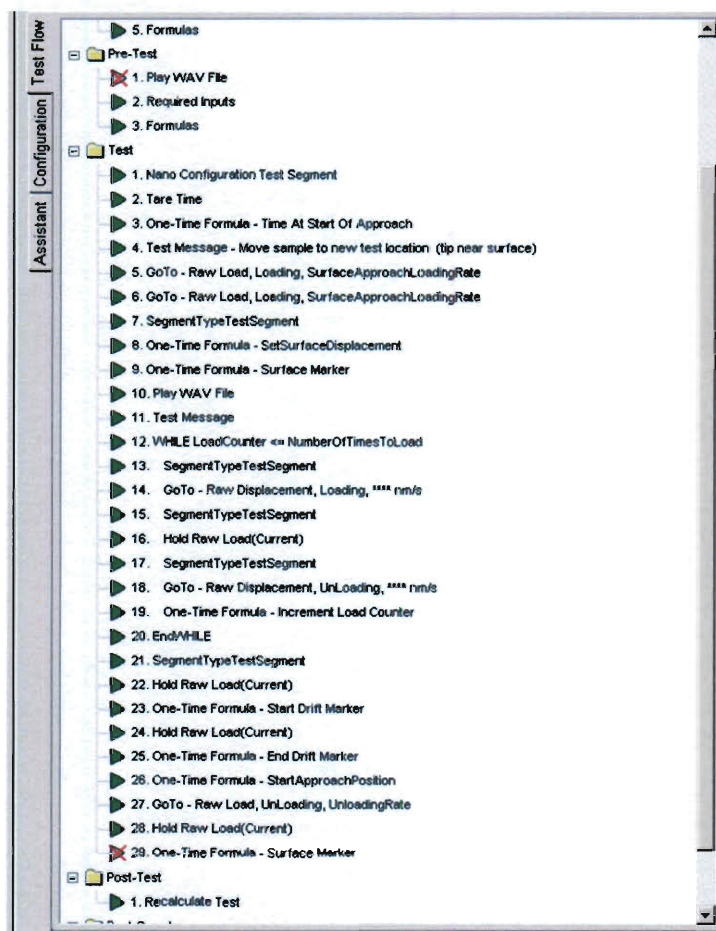
Figure 3.21 Program used to perform displacement controlled experiments using the InSEM™ nanoindenter.

3.3.5. Sample Stress vs. Strain Curve Extraction

The proper measurement of loads and displacements that one encounters when studying the mechanical properties of 1-D nanostructures can be extremely difficult because of their size. Usage of the quantitative nanoindenter to apply forces & displacements on a micro-device essentially alleviates three of the main pain points associated with the *in situ* experimental characterization of 1-D nanostructures, i.e., 1) application and measurement of forces with nano-Newton resolution; 2) measurement of local mechanical deformation with nanometer resolution; and 3) direct and independent (of imaging technique) measurement of load and deformation allowing real-time observation of the deforming samples (see Table 3.2). However, one should note that extraction of the stress vs. strain curves for individual samples clamped on the micro-devices from their corresponding nanoindenter load vs. displacement curves is a non-trivial task. Finite-element-analysis (FEA) based conversion factors were used to analyze the experiments conducted on the Ni nanowires. The analysis technique, described in detail below, was found to be applicable for analyzing tests conducted on linear elastic brittle materials such as the Ni nanowires.

In order to derive the stress vs. strain curve for any given 1-D nanomaterial from the nanoindenter tip load vs. displacement data, two parameters, a) the ratio of the force acting on the sample to the load applied by the indenter tip i.e. the force conversion coefficient, C_F, and b) the ratio of the sample stage shuttle displacement/sample elongation to the nanoindenter tip displacement i.e. the displacement conversion coefficient, C_D, must be determined. The values

of C_F and C_D depend upon device stiffness and the stiffness of the specimen being tested (henceforth referred to as the sample stiffness). The sample stiffness can be estimated from the system stiffness, K_s, defined as the ratio of the applied load to the displacement of the indenter tip i.e. slope of the indenter load vs. displacement curve, using a finite element model. The behavior of the device was modeled in order to generate three curves, namely K_s vs. sample stiffness curve, the C_F vs. sample stiffness curve and the C_D vs. sample stiffness curve (see Figure 3.22). The value of sample stiffness obtained from the K_s vs. sample stiffness curve can be used to ascertain the values of C_F and C_D for a given experiment (with the help of the C_F vs. sample stiffness curve and the C_D vs. sample stiffness curve). Because of the device's planar beam-based geometry, 2-D FEA models were constructed using ANSYS™ Beam 32 elements in order to generate the curves. Material nonlinearities were ignored since the device layer was made of single crystal silicon which is linear elastic at the temperatures at which the experiments were conducted. However, since large deformations might occur as the indenter load increases, geometry nonlinearities were considered in the analyses. For all the analyses, the Young's modulus and Poisson's ratio of single crystal silicon were set equal to 160 GPa (value obtained via nanoindentation of the device layer after fabrication) and 0.278 respectively. Virtual nanowires, (treated as ANSYS™ Link 1 elements) with a Poisson's ratio value set equal to 0.310 (value for bulk nickel), were used to model the device behavior in the presence of a sample.
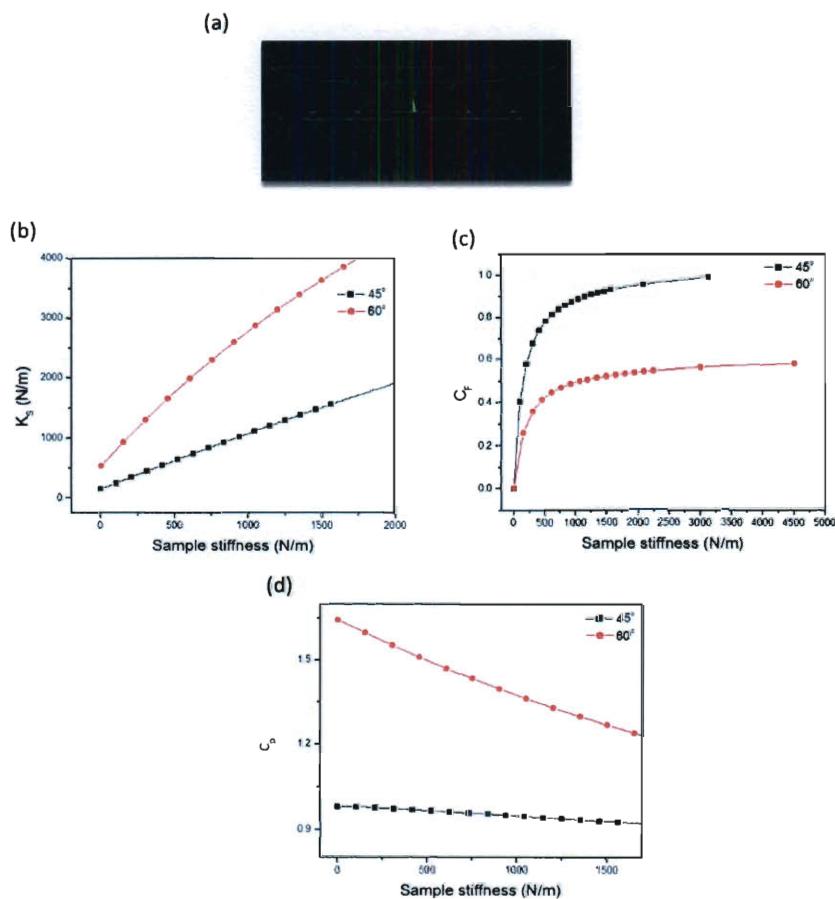
Figure 3.22 (a) A 2-D FEA model (ANSYS BEAM 32 elements) of the device. (b) System stiffness, K_s vs. sample stiffness curves, (c) force conversion coefficient, C_F vs. sample stiffness curves and (d) displacement conversion coefficient, C_D vs. sample stiffness curves as obtained using finite element analysis (The red and black curves correspond to 9 ± 0.5 μm thick generation II devices that were composed of eight inclined beams making an angle of 60° and 45° with respect to the sample stage shuttles respectively).

3.3.6. Error Analysis

Uncertainty in the values of C_F and C_D arise from two sources; random errors such as variation of device thickness, and systematic errors such as misalignment of indenter tip and/or specimen (see Figure 3.24). The uncertainty in the value of C_F was estimated via FEA. For all the devices fabricated, the

thickness variation was about ±0.5 μm, the angles of indenter tip misalignment was assumed to be less than 5^0, the offset distance of loading point for the indenter tip was assumed to be less than 5 μm and the angles of nanowires misalignment was assumed to be less than 10^0. The results of an error analysis conducted indicated that the error in the value of C_F, as a result of the aforementioned factors, would be less than 13% for a device (in the presence of a mounted sample) having a stiffness equal to 1500 N/m. The error in the value of C_D was estimated by comparing the C_D values for the standalone device obtained via finite element analysis with those obtained experimentally via indentation of a standalone device (9 ± 0.5 μm thick devices with eight 45 degree inclined beams) (see Figure 3.23). The experimental values of C_D for the standalone device, in the load range of 0.25 to 2 mN, were obtained by loading it to preset levels followed by acquisitions of high resolution images of the sample stage shuttle gap. The average experimental C_D value, 0.96, when compared to the value obtained by finite element analysis, yielded an error value of 2 %.

The uncertainty in the measurement of force F_y and displacement y_l arise mainly due to the precision of the nanoindenter. The force and displacement resolution values for the InSEM® indenter were known to be 69.4 nN and 0.8675 nm respectively. Since the maximum force applied by the indenter and the maximum indenter head displacement (before sample failure) for a representative experiment conducted on a nickel nanowire were approximately 0.13 mN and 100 nm respectively,

$$\left(\frac{\Delta F_y}{F_y}\right)^2 = \left(\frac{69.4\ \text{nN}}{0.13\ \text{mN}}\right)^2 < 1 \times 10^{-4} \text{ and } \left(\frac{\Delta y_1}{y_1}\right)^2 = \left(\frac{0.8675\ \text{nm}}{100\ \text{nm}}\right)^2 < 1 \times 10^{-4}$$

Uncertainties in the measurement of sample length and diameter arise from the pixel resolution of the SEM micrograph viz. about 10nm. Since the gauge length and diameter of the sample are in order of 4 μm and 300 nm respectively,

$$\left(\frac{\Delta L}{L}\right)^2 = \left(\frac{10 \text{ nm}}{4 \text{ } \mu m}\right)^2 < 1 \times 10^{-4} \text{ and } \left(\frac{\Delta A}{A}\right)^2 = \left(\frac{2\Delta d}{d}\right)^2 = \left(\frac{2 \times 10 \text{ nm}}{300 \text{ nm}}\right)^2 = 4.4 \times 10^{-3}$$

Clearly, the primary source of error is associated with the force conversion factor C_F, and is produced by uncertainties introduced by fabrication, sample manipulation and the experimental setup.
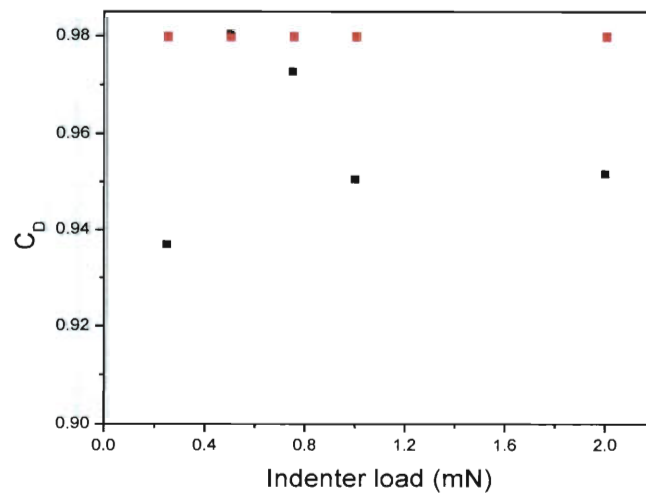
Figure 3.23 C_D, plotted as a function of indenter load for a 9 ± 0.5 μm thick device (geometry shown in Figure 3.7) in the absence of a mounted sample. The red points show the values of C_D, as obtained from FEA. The black points show the values of C_D obtained via image correlation i.e. analysis of SEM images captured during indentation.
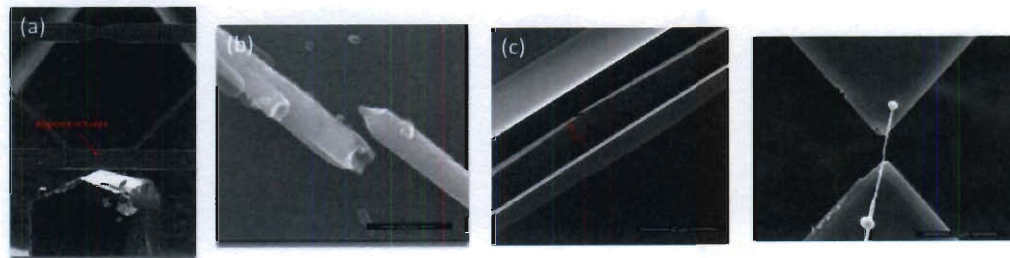
Figure 3.24 Errors were minimized via adoption of a number of procedures. (a) SEM image shows alignment holes that were incorporated onto the devices to facilitate nanoindenter tip alignment. (b) Ion beam assisted deposition of Pt, used for sample clamping, deposits a sheath of Pt around nanowire/nanotube specimens leading to errors. Hence this clamping technique was not used for any of the actual experiments. (c) SEM image shows the side profile of a perfectly planar device. Residual stresses in the device layers of the SOI wafers were a source of error. Devices were flipped onto their side to assess their planarity and non planar devices were discarded. (d) Misaligned nanowire/nanotube specimens were always discarded. Scale bars in (b), (c) and (d) read 500, 40 and 10 μm respectively.

3.3.7. The Tensile Testing of Ni Nanowires: Results

The indenter load vs. displacement curve for a representative tensile test is shown in Figure 3.25. The nickel nanowire specimen used for this experiment was about 12 μm long and had a diameter of 298 nm. The gauge length of the specimen i.e the distance between the clamping points, was ascertained by observation of the side profile of the sample across the sample stage gap under a SEM, and found to be equal to 3.1 μm. The slope of the load vs. displacement curve before and after sample failure was used to determine the stiffness of the device in the presence of and after the failure of a mounted specimen. The initial slope of the curve (1259 N/m) corresponds to the stiffness of the device in the presence of the specimen before failure. A sudden change in the slope of the indentation curve occurs at a load ~0.114 mN which is indicative of the nanowire

sample failure. This phenomenon was independently verified from the sample deformation video. It occurs because, once the sample fails, the slope of the curve (155 N/m) must become equal to the stiffness of the device in the absence of a mounted sample viz. 154.03 N/m as per the finite element model. By interpolation of the K_s vs. sample stiffness curve (Figure 3.22 (b)) the sample stiffness was determined (1211 N/m). The values for C_F and C_D were subsequently determined (using the curves shown in Figures 3.22 (c) and (d)) and the stress vs. strain curve (see blue curve in Figure 3.26 (right)) was plotted. The stress strain curves for two other samples were obtained in a similar fashion. One of the samples tested was found to have undergone considerable plastic deformation (black curve in Figure 3.26 (right)). In this case, two separate sets of values for C_F and C_D, obtained using two separate values of K_s, were used to derive the stress vs. strain curve. The measured Young's moduli for the Ni nanowire specimens (equal to the slope of the stress vs. strain curves shown in Figure 3.26 (right)), were found to be about 25% of that of single crystal Ni along the <112> direction viz. 232.5 GPa. [57] Another feature that was revealed during the experiments was that the nanowires did not fracture until the value of applied stress reached a value greater than 1.3 GPa (see Table 3.5). The ultimate tensile strength values for the samples tested were found to be much higher than the ultimate tensile strength of Ni in bulk form viz. 140-195 MPa. [58] This phenomenon is attributed to the fact that when materials are scaled down, their strength approaches the theoretical strength, i.e. ~1/10 of the Young's modulus).
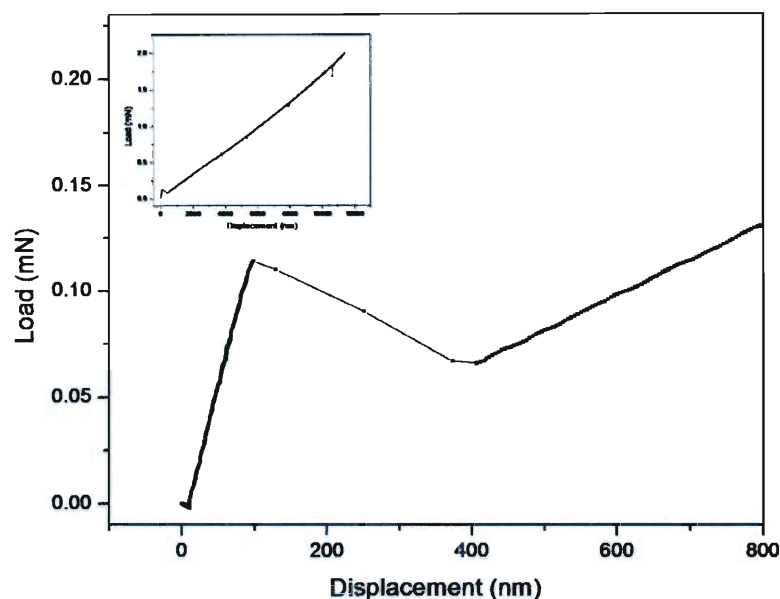
Figure 3.25 Graph shows the nanoindenter load vs. displacement curve for the first 7.5 seconds of a tensile test performed on a 298 nm diameter Ni nanowire sample; inset shows the load vs. displacement curve for the entire loading part of the experiment.
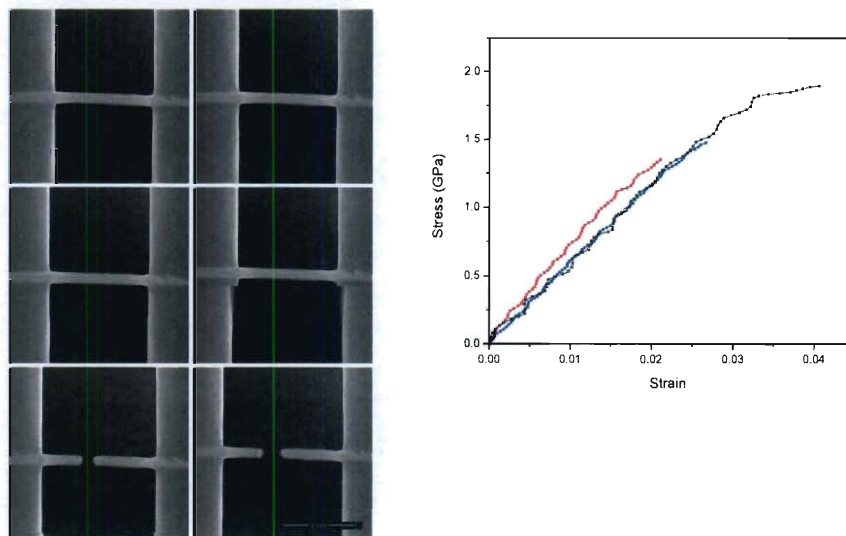
Figure 3.26 (Left) SEM video snapshots show the deformation and failure of a Ni nanowire specimen under tensile loading at (a) t=0 s, (b) t=1 s, (c) t=2 s, (d) t=3 s, (e) t=4 s, and (f) t=6 s. The experiment was conducted at an indenter loading rate of 30 μN/s. (Right) Engineering

stress vs. strain curve for Ni nanowire specimens as derived from the indenter load vs. displacement data. The red curve corresponds to a 263 nm diameter specimen, the blue curve corresponds to a 298 nm diameter specimen and the black curve corresponds to a 215 nm diameter specimen.

Table 3.5 Table shows the nanowire properties determined from the stress vs. strain curves shown in Figure 3.26 (right). Young's modulus values shown are essentially the apparent Young's moduli as they were assumed to be equal to the slope of the stress vs. strain curves. Note that in order to accurately estimate the Young's modulus of a material, load-unload-reload cycles need to be performed.

Sample Diameter (nm)	Young's Modulus (GPa)	Ultimate tensile strength (GPa)	Failure strain (%)
298	56.879	1.472	2.66
215	55.556	1.896	4.0
263	62.993	1.35	2.11
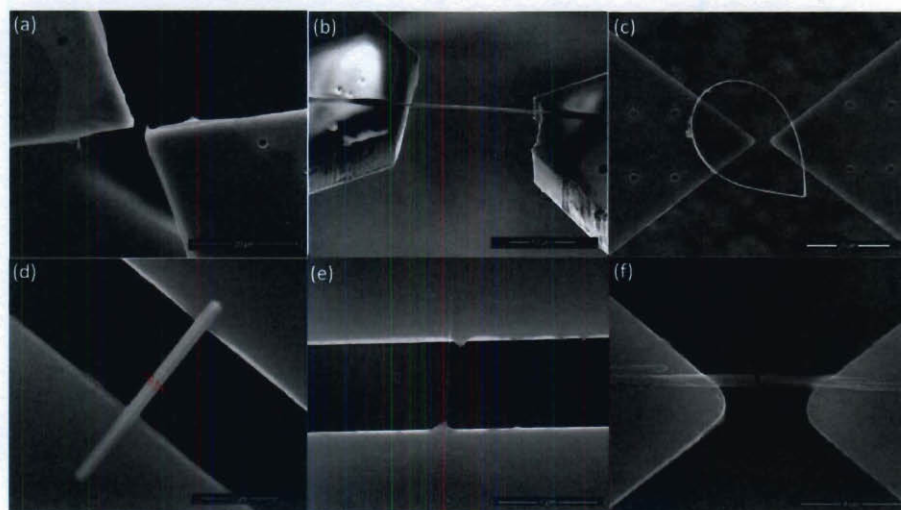
Figure 3.27 Besides Ni nanowires, the technique has also been used to study the mechanical properties of a number of materials including (a) Au nanowires (50-70 nm diameter), (b) Cu nanowires (200-300 nm diameter), (c) Cu nanorings (200-500 nm diameter), (d) Au rods (300-400 nm diameter), (e) arc discharge grown MWNTs (40-70 nm diameter) and (f) AAO template grown highly disordered MWNTs (200-300 nm diameter).

3.4. Conclusions

The development and application of a novel technique for the *in situ* mechanical characterization has outlined in this chapter. Sample preparation and experimental procedures adopted have been discussed in detail. The primary advantages of the technique are its simplicity and its capability to produce high-resolution quantitative data while simultaneously enabling uninterrupted real-time observation of the sample deformation process. It should be noted that while the experiments described in this chapter were discussed in the context of *in situ* tensile testing, the technique itself is versatile and can not only be used to study the mechanical properties of numerous small scale materials (see Figure 3.27) but also the mechanical properties of interfaces (Chapter 5).

4. Mechanical Characterization of Individual Catalytically grown Multi-Wall Carbon Nanotubes

4.1. Mechanical Characterization of Individual Pristine and N doped MWNTs

One of the most promising uses for CNTs is as reinforcements for high strength/stiffness/toughness composites. This is because their mechanical properties are considerably better than those of conventional fibrous materials. Theoretical predictions show that CNTs must possess ultra-high strengths, as high as 300 GPa for single walled carbon nanotubes (SWNTs) [31], owing to the strength of the sp^2 C-C bonds, considered to be the strongest of all chemical bonds. Experimental studies, on the other hand, have reported tensile strength values that vary between 30-110 GPa for individual MWNTs [15, 16] and between 13-53 GPa [17] for SWNTs (indirect measurement). Lower than expected values of measured strength can be attributed to the presence of defects in their structure introduced during purification, sonication or due to electron beam induced reactions between the tubes and residual water within an electron microscope chamber. [60] Also, it well known that the mode of CNT synthesis plays an important role in determining the nature and distribution of defects with catalytic chemical vapor deposition (CVD) grown nanotubes having a more defect

laden structure when compared to nanotubes grown via other techniques such as laser vaporization and arc discharge (AD).

Owing to their small size and the magnitude of the forces and deformation involved, the mechanical characterization of individual SWNTs via direct techniques such as tensile testing is considered extremely challenging. However, with regard to individual MWNTs, a number of indirect as well as direct measurements of the mechanical properties (including tensile strength) have been reported in the past (see Chapter 2). MEMS based tensile testing techniques have a number of advantages over techniques such as dynamic vibration analysis [24] and AFM based lateral bending. [25] Some of these advantages include their ability to provide *in situ* imaging of deformation and obtain stress vs. strain curves for the specimens tested. However, most of the MEMS based studies conducted in the past have focused on high quality nearly defect free arc discharge grown MWNTs. [15, 16] Such MWNTs have been found to possess excellent mechanical properties and their deformation usually involves only a single (outermost) load bearing shell. Little is known however, about the mechanical strength, nature of inter-shell load transfer and failure mechanisms associated with MWNTs grown catalytically via chemical vapor deposition even though these materials are routinely used for research and commercial applications. Hence, the novel technique described earlier was used to probe the mechanical properties of individual pristine MWNTs and that of nitrogen doped MWNTs (CN_x nanotubes), grown catalytically by uniaxial tensile testing, *in situ*, within a SEM chamber.

4.1.1. MWNT Growth and Characteristics

Pristine MWNTs specimens were grown on bare quartz substrates by a direct liquid injection chemical vapor deposition (DLI-CVD) technique which involved injecting a mixture of a 20 mg./ml. ferrocene $((C_5H_5)_2Fe)$ in xylene (C_8H_{10}) solution into a two-stage thermal CVD reactor consisting of a low temperature (200 C) pre-heater followed by a higher temperature main reactor (775 C). The same technique was also used to synthesize the CN_x nanotubes wherein a mixture of xylene and acetonitrile (CH_3CN) acted as the carbon/nitrogen source. A 1 gm. ferrocene dissolved in a 75 ml of xylene + 25 ml of acetonitrile solution mixture was injected into a quartz tube, that was held at 900 C, with the help of a peristaltic pump (flow rate 1ml./min.). In both cases a hydrogen/argon mixture was used as the carrier gas.

TEM images (see Figure 4.1) revealed that the pristine MWNTs thus grown possessed a nested tube structure wherein each MWNT comprised of c.a. 100 continuous shells; the presence of arrays of internal carbon walls (compartment layers) was not obviously evident along the length of the specimens. The CN_x nanotubes on the other hand, exhibited very distinct morphologies, significantly different from the pristine MWNTs. These tubes possessed a nitrogen content of 2-3% as determined by X-ray photoelectron spectroscopy (XPS) (data not shown) and exhibited a bamboo like structure, wherein the interior of the nanotubes contained irregularly spaced arrays of compartment layers. The CN_x nanotubes we tested were each found to be made up of about 50-80 shells; while the outer 20 or so graphitic shells were continuous

throughout the length of the MWNTs, the inner 30-60 shell arrays were found to combine with compartment layers without any defects, resulting in irregular reductions in the total wall thickness. It is important to note that the tube themselves did not appear to be a linearly stacked line of bell cavities, a characteristic observed frequently in such nanotubes [61, 62], owing to the presence of the outer array of continuous shells. The differences in the morphologies of the inner and outer wall arrays were assumed to have arisen due to the higher nitrogen incorporation within the internal nanotube walls. [62]
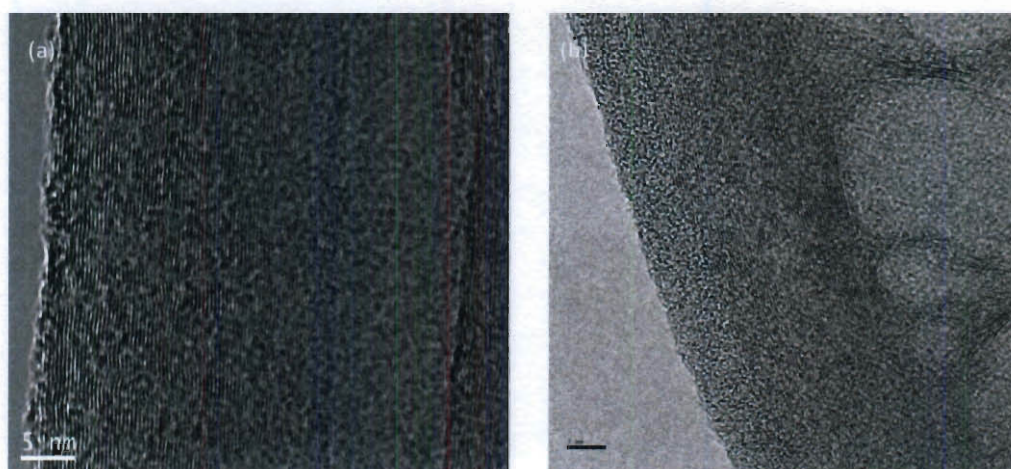
Figure 4.1 TEM images show the morphologies of the (a) pristine MWNTs and the (b) CN$_x$ MWNTs (scale bar in image reads 10 nm).

4.1.2. Tensile Testing Technique

The novel technique outlined in the previous chapter was used to perform the tensile testing experiments on the MWNTs. Its use for testing the aforementioned samples is advantageous for two reasons- a) As stated earlier, it allows the application and measurement of forces with nano-Newton resolution and measurement of local mechanical deformation independently and with nanometer resolution. b) Also, most catalytically grown MWNTs are curved to a

certain degree; hence the samples would be required to be pulled apart to a certain extent before any load application can occur. A clear shift in the indenter load vs. displacement curve is generally observed at the point at which load application on the specimen begins to occur (see Figure 4.4), thus facilitating the extraction of accurate stress vs. strain curves.
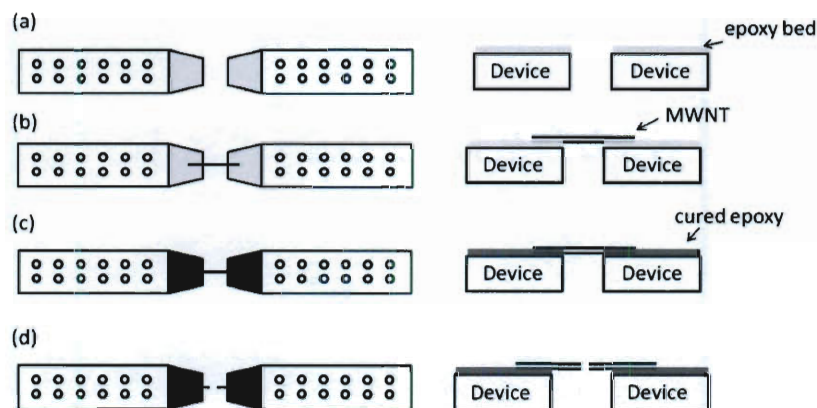
Figure 4.2 Sample preparation procedure; for each step undertaken, the top and side views of the sample stage shuttles are shown side by side. (a) The ends of the sample stage shuttles were first coated with thin layers of epoxy, (b) an individual MWNT was placed across the gap. (c) The thin layers of epoxy, upon curing, clamp the MWNT onto the device. (d) Once this happened, the tensile testing experiments could be performed.

9 ± 0.5 µm or 6 ± 0.5 µm thick devices (Figure 3.7 shows geometry) were used for all the experiments described in this chapter. Sample mounting was accomplished by following a procedure similar to the one outlined in Chapter 3. A portion of each sample stage shuttle was first coated with a thin layer of epoxy (HARDMAN Water-Clear Epoxy). A droplet from a sonicated suspension of the MWNTs in toluene was deposited onto a Si wafer coated with a 50 nm thick layer of titanium. Individual MWNTs, that were about 10 um in length and 70-100 nm in diameter and hence visible under an optical microscope, were subsequently

"picked up" and placed across the shuttles using micromanipulators housed within a probe station. Tungsten tips were used to perform the manipulation of the MWNTs, since they were found to attach to the tips possibly via van der Waals' forces or surface charging induced electrostatic and frictional forces. The epoxy layers, upon hardening, acts as clamps for the tensile specimens. The use of epoxy for clamping purposes was favored over e-beam induced carbon deposition methods (EBID) since it has been known to reduce the probability of nanotube slippage and debonding from the sample stage shuttles. [63] E-beam assisted Pt deposition was also considered unsuitable for sample clamping since it often causes the formation of a Pt sheath (see Chapter 5) around the specimens thus reducing the accuracy of the stress vs. strain curves obtained. The gauge length of the specimens i.e. the distance between the clamping points, were ascertained by observation of the side profile of the samples across the sample stage gap under a SEM.

The tensile experiments were performed within a SEM (FEI Quanta 400 high resolution field emission scanning electron microscope) equipped with an InSEM® Indenter system (see Figure 4.3). A blunt berkovich nanoindenter tip was used for load application on the top shuttle. The nanoindenter tip was first aligned with the top shuttle of the device in order to make sure that the sample stage shuttles moved symmetrically. Once this was done, the electron beam was focused on the nanotube specimens in order to monitor their deformation and fracture in real time. The experiments were conducted at an indenter tip displacement rate of ~10 nm/s (for the MWNTs, this corresponds to a strain rate

of approximately 0.002 sec^{-1}) with the load vs. displacement data being collected at a rate of 25 Hz. The maximum load applied on the device varied between 0.1 to 0.5 mN. Once this value was reached, the load was held constant for 0.5 seconds. This was followed by an unloading step at aforementioned displacement rate. A thermal drift correction hold step was performed at about 1-0.1 % of the maximum applied load for about 50 seconds in order to account for small amounts of thermal expansion or contraction in the test material and/or indentation equipment.

A select number of samples tested were analyzed post-mortem within a high resolution transmission electron microscope (JEM 2100F HR-TEM) chamber. In those cases, the devices that were used to perform the tensile tests were first separated from the substrate by etching away sections of their inclined and support beams using a focused ion beam (FEI Strata DB 235, FEI corp.). A micromanipulator probe was subsequently used to place the devices, laden with the fractured specimens, onto TEM grids for imaging (see Figure 4.6).
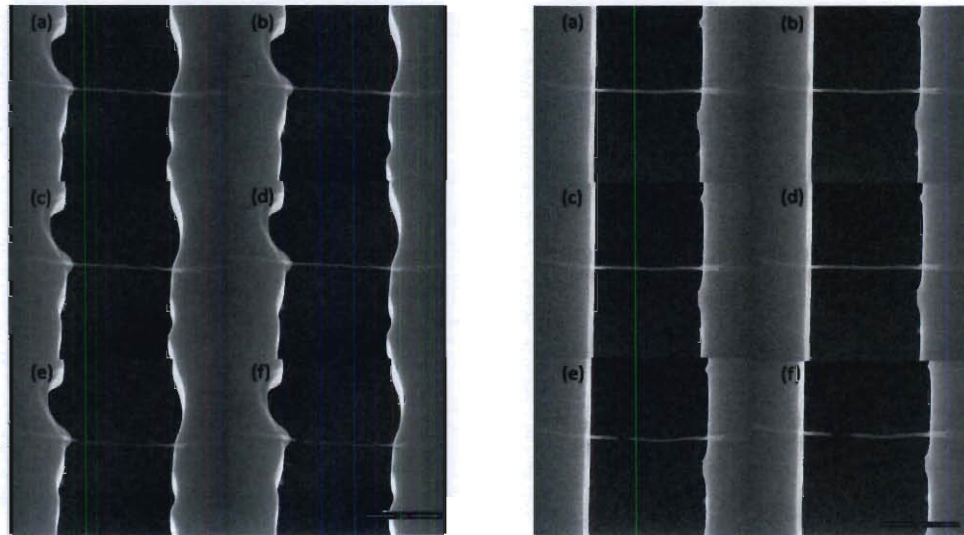
Figure 4.3 SEM snapshots show (left) a pristine MWNT specimen undergoing deformation and failure under a tensile load at (a) t=0, (b) t= 4, (c) t= 8, (d) t= 12, (e) t= 15 and (f) t= 17 seconds. (right) A nitrogen doped MWNT specimen undergoing deformation and failure under a tensile load at (a) t=0, (b) t= 1, (c) t= 2, (d) t= 3, (e) t= 5 and (f) t= 8 seconds. The experiments were conducted at an indenter tip displacement rate of 10 nm/s.

4.1.3. Stress vs. strain Curve Extraction

The FEA based method for stress vs. strain curve extraction from indenter load vs. displacement data outlined in Chapter 3 is only applicable when analyzing curves for linear elastic brittle materials; it is also subject to large errors when analyzing low stiffness specimen curves and does not take into account the actual stiffness of each individual device. A new technique, referred to as response subtraction, was thus developed that is applicable for analyzing tensile testing data pertaining to any given specimen. Response subtraction essentially involves the ascertainment of forces needed to strain the specimens by subtracting the forces needed to deform the device alone from the forces needed to deform the device with the specimen (before specimen fracture occurs). The displacement

conversion coefficient, C_D (defined in the previous chapter) must be incorporated into the equation since the sample elongation = C_D x indenter head displacement. Thus

$$F_s = \frac{1}{C_D}(P_1 - P_2) \qquad (1)$$

where F_s is the force acting on the sample, P_1 is the indenter load value at any point on the load vs. displacement curve of the device in the presence of a mounted specimen and P_2 is the load value for the corresponding deformation of the device alone. The response subtraction method is based on the assumption that the energy expended on deforming the device in the presence of a mounted specimen is equal to the sum of the energy expended on deforming the device alone and the energy expended on deforming the specimen.

The value(s) of C_D for any given experiment can be obtained, in theory, via SEM image correlation (see Chapter 3). However, since it does not vary significantly with variations in the sample stiffness (see Figure 4.5) for the device geometry used that was used for all the experiments pertaining to this thesis, SEM image correlation cannot be used to determine the value of C_D with sufficient accuracy. This is because SEM image snapshots (extracted from video) do not possess sufficient resolution for one to detect the subtle variations in the value of C_D. Hence FEA based curves (Figure 4.5) were used to ascertain the average C_D value for each experiment.
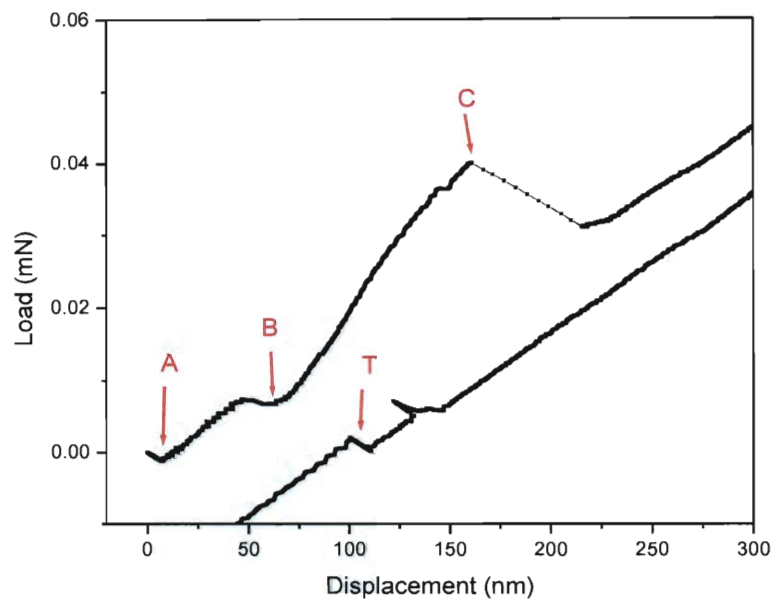
Figure 4.4 Graph shows a section of the indenter load vs. displacement curve (loading and unloading) for a test performed on a pristine MWNT specimen. The letter "A" corresponds to the point at which the nanoindenter begins to apply a force on the device , "B" corresponds to the point at which load application actually begins on the MWNT specimen, "C" corresponds to the point of specimen failure and the letter "T" indicates the region corresponding to the thermal drift correction segment.
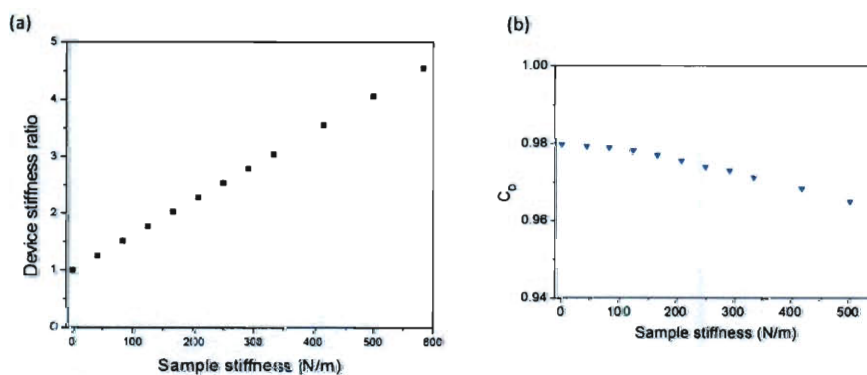
Figure 4.5 (a) Device stiffness ratio (defined as ratio of stiffness of device in the presence of a sample to that of device alone) vs. sample stiffness plot obtained via FEA. The value of device stiffness ratio for each experiment equals the ratio of the slope of the load vs. displacement curve before sample failure to the slope of the load vs. displacement curve after

sample failure (i.e. device stiffness). The device stiffness ratio value (average) for each experiment was used to determine an approximate value for the sample stiffness; sample stiffness value was subsequently used to deduce the C_D value for the experiment using (b) the C_D vs sample stiffness plot (obtained via FEA).
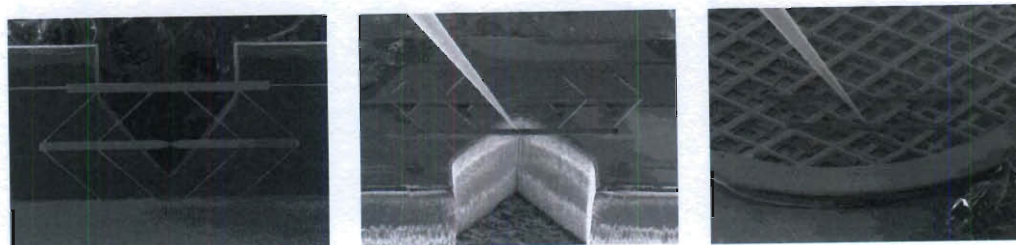
Figure 4.6 TEM sample preparation procedure. (left) Sections of the device's inclined and support beams were etched and (center) using a micromanipulator probe, the device was picked up and (right) placed on a TEM grid.

4.1.4. Test Results and Discussion

It is well established that when defect free MWNTs are subject to tensile loading, only the outermost wall of each tube can be considered to be load bearing. Such MWNTs fail *via* a "sword in sheath" mechanism with the inner walls experiencing a pullout after failure of the load-bearing wall. On the other hand, in the case of CVD grown MWNTs such as the ones used in our experiments, the presence of a large density of vacancies, interstitials of carbon atoms or atoms of the catalyst, Frenkel pairs and dislocations can result in significant intershell cross-linking as a result of which multiple graphitic shells bear tensile loads (see Figure 4.7). The occurrence of cross-linking can be confirmed by the observation of multiple wall fracture at the point of nanotube failure on a fractured specimen. B. Peng *et al.*, for example, observed a simultaneous fracture of 3 to 52 shells in arc discharge grown MWNTs that were inter-shell cross-linked *via* electron irradiation. [16] Thus, in order to accurately

plot the stress vs. strain curves for the catalytically grown MWNT specimens tested, the nanotube load bearing cross section areas were estimated *via* examination of representative fractured specimens using transmission electron microscopy (TEM). In the case of all the pristine MWNTs tested, careful analysis of SEM and TEM images of fracture specimens led us to the conclusion that all the shells (walls) bore the tensile load, since all the graphitic shells were found to have failed in close proximity to one another (see Figure 4.8 (c)). On the other hand TEM images of fractured nitrogen doped MWNT specimens showed that the inner shell arrays that were connected to compartment layers remained intact in the regions where failure occurred (see Figure 4.8 (d)). Only the outer 20 or so shells were found to have failed as a result of the tensile loads. Based upon this, one could conclude that, in the case of the nitrogen doped MWNTs, only the outer shells bore the bulk of the tensile loads; the inner shells were subject to minimal amount of stresses, if any, during the tensile tests. The stress vs. strain curves, plotted in Figure 4.9 (a), were computed based on the assumption that the entire cross-section area of each pristine MWNT was load bearing. The stress vs. strain curves, plotted in Figure 4.9 (b), on the other hand, were computed based on the assumption that only the outer continuous walls of the CN_x nanotubes bore the tensile loads.

From stress vs. strain curves it is evident that while both types of nanotubes were found to possess comparable strengths, average values being 2.13 GPa and 1.52 GPa (see Table 4.1) for the pristine and nitrogen doped MWNTs respectively, the pristine MWNTs possessed higher load bearing capacities

compared to the nitrogen doped MWNTs due to the differences in the load bearing cross section areas. Note also that the strength values of all the MWNTs tested, while consistent with the Young's modulus measurements performed by bending (values as low as 12 GPa were reported) [26, 64], were found to be considerably lower than those reported by Barber *et al.* [63] However, one must bear in mind that the high values reported in the latter manuscript were computed based on the assumption that only the outermost wall of each nanotube tested was load bearing (see Table 4.3). Based on our analysis of fractured specimens, we believe that this might not necessarily be a reasonable assumption for the MWNT samples investigated in this study (see Table 4.3).
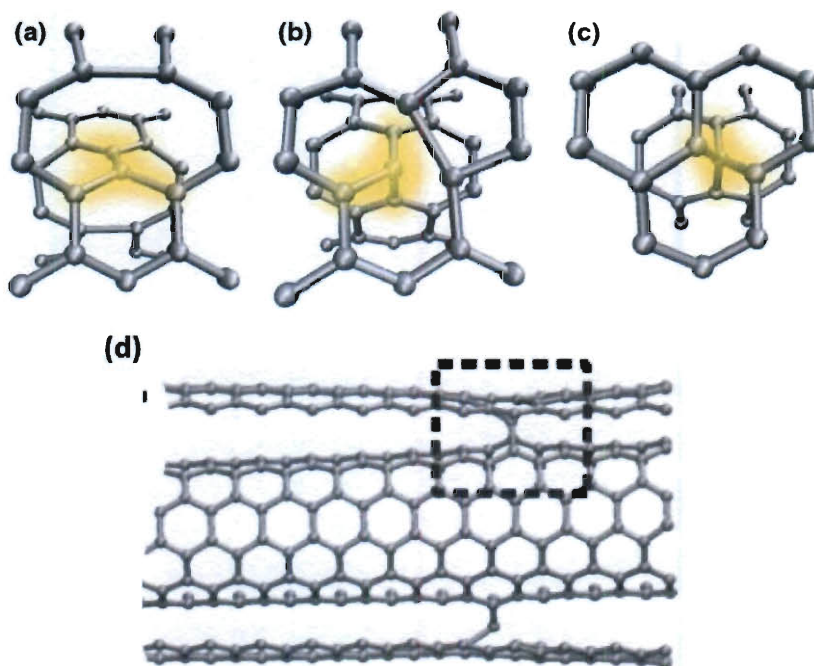
Figure 4.7 Three common crosslinking defects types are a) divacancies, b) Frenkel pairs and c) interstitials. [65] (d) Computational model of a Double Walled Carbon Nanotube showing cross-linking caused by the existence of a Frenkel pair (dashed box) [16]
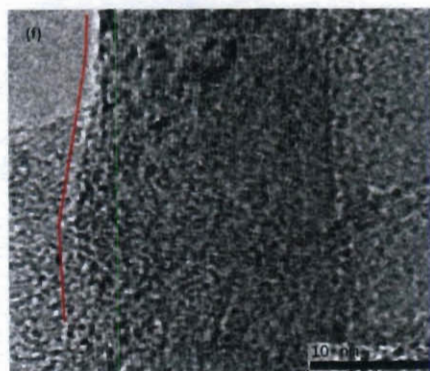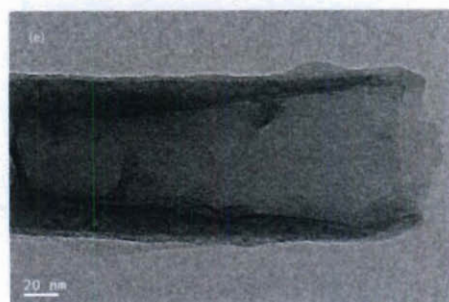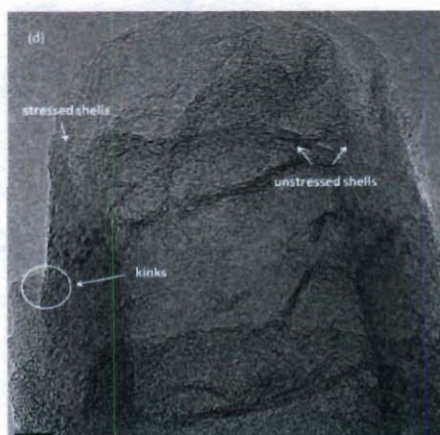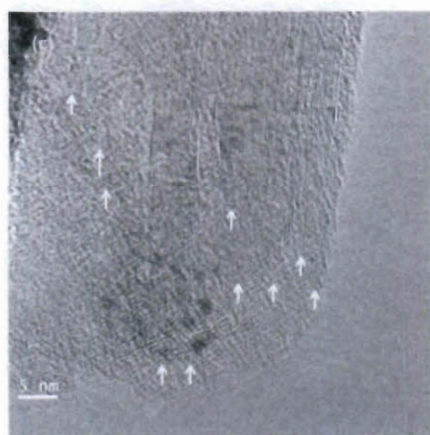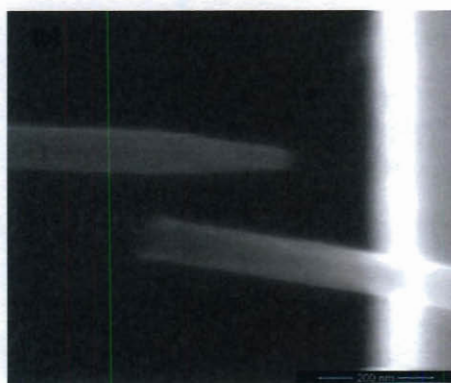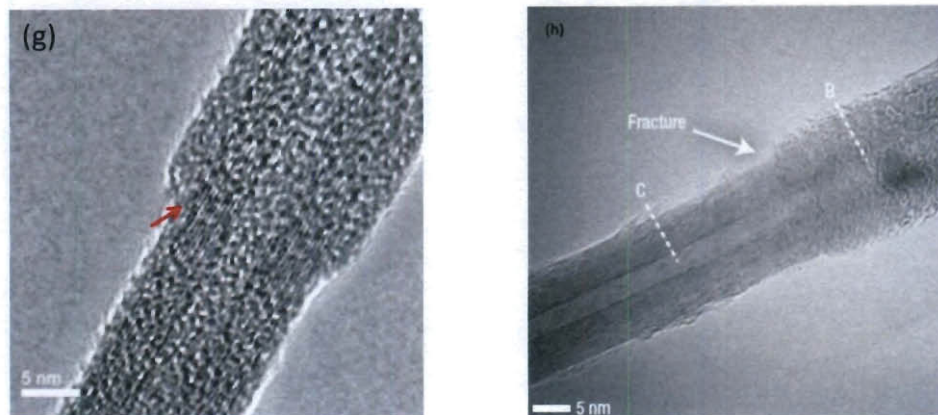
Figure 4.8 SEM images show a close up view of (a) a pristine MWNT fracture specimen and (b) a **nitrogen doped MWNT fracture specimen. TEM images** show (c) a section of the fracture surface of a pristine MWNT with arrows indicating the regions where wall fracture occurred. (d) and (e) are TEM images showing fracture surfaces (corresponding to the left and right sections shown in (b) respectively) of a nitrogen doped MWNT with arrows indicating the load bearing and the non load bearing walls. Scale bar in (d) reads 10 nm. (f) Close up view of the kink circled in (d) with red lines drawn to elucidate its shape. (g) TEM image shows single, outermost wall (shell) fracture frequently observed in defect free arc discharge MWNTs upon application of tensile loads (arrow indicates the fractured wall). [16] (h) TEM image shows multiple wall fracture that was observed after an arc discharge MWNT, subjected to electron beam induced cross-linking, was stretched to failure (arrows indicate point of failure). [16]

(a)

(b)
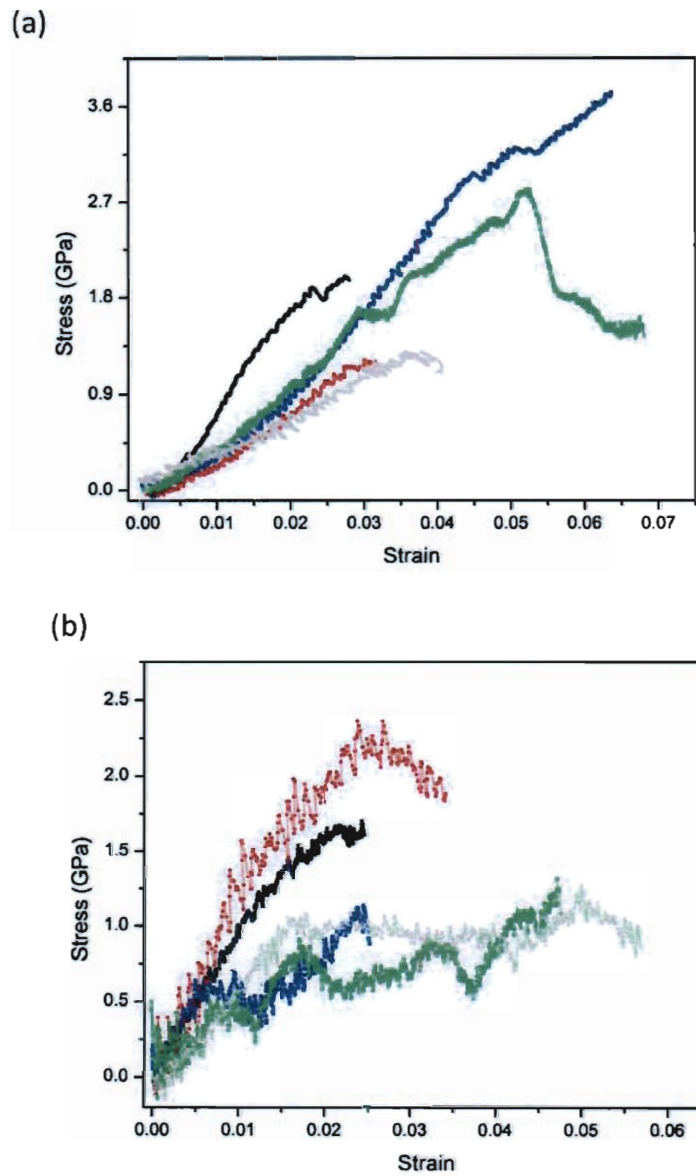
Figure 4.9 Engineering stress vs. strain curves for (a) 5 pristine MWNT specimens and (b) 5 nitrogen doped MWNT specimens.

Table 4.1 Table shows the measured maximum load borne and the tensile strength values of 5 pristine and 5 nitrogen doped MWNTs. All sample diameters were in the 70 to 100 nm range.

MWNT type	Maximum Load (nN)	Tensile strength (GPa)
pristine	6873	1.20
pristine	36838	3.72
pristine	15929	1.96
pristine	11179	0.99
pristine	11654	2.80
nitrogen doped	3953	2.33
nitrogen doped	3409	1.61
nitrogen doped	2120	1.13
nitrogen doped	1829	1.23
nitrogen doped	2557	1.32

Another intriguing feature observed during the course of the experiments was the fact that while the stress vs. strain curves for most of the pristine MWNTs tested were linear up until the point of failure, the curves for the nitrogen doped MWNTs consistently exhibited varying degrees of non-linearity especially at high stress levels. High resolution fracture surface images of the tested nitrogen doped MWNTs specimens clearly showed the presence of a 35-150 nm long region of reduced cross-section area that often extended beyond the amorphous carbonaceous layer that uniformly covered all the tested MWNTs. More importantly, close observation of the HR-TEM images of multiple fractured specimens clearly indicated the presence of kinks on the outer continuous wall arrays adjacent to these regions of reduced cross-section area (see Figure 4.8 (b), (d), (e) and (f)). On the other hand, while some of the pristine MWNT stress vs.

strain curves did exhibit a certain degree of non-linear behavior, their post failure specimens were found to consistently possess relatively flat fracture surfaces (see figure 4.8 (a) and (c)), that were in the vicinity of or were embedded within the preexistent amorphous carbonaceous layers, and no kinks were found in the proximity of the fracture surfaces (features that were consistent with brittle bond breaking mechanism of failure).
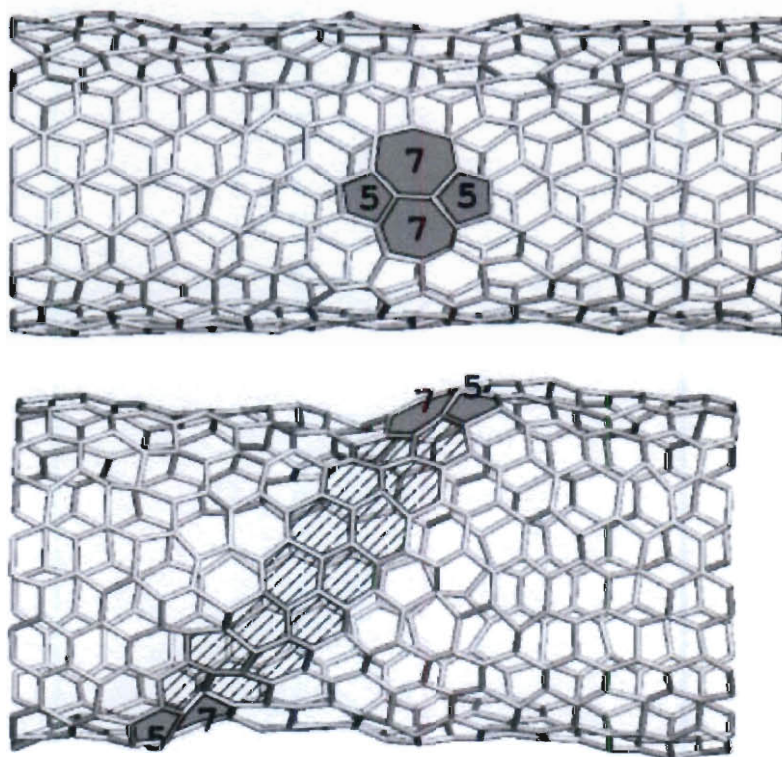
Figure 4.10 Snapshots obtained from molecular dynamics simulations of a (10, 10) nanotube under axial tension. (Top) Formation of a Stone-Wales defect at 2000 K and 10% strain. (bottom) Plastic flow behavior after ~2.5 ns at 3000 K and 3% strain (the shaded area indicates the migration path of the (5-7) edge dislocation). [66]

At temperatures close to 2000 °C super-plasticity has been observed in the past, by Huang *et al.*, [67] in catalytically grown SWNTs and the phenomenon

was attributed to the formation and motion of kinks caused by Stone-Wales defects (see Figure 4.10); in fact, kink motion was found to be the universal plastic deformation mode in all nanotubes. [68] Theoretical studies have shown that that the two alternative routes of brittle bond breaking and plastic relaxation (*i.e.* via kink formation and motion) are mutually competitive. At ambient temperatures, the former failure mechanism is more likely to be prevalent since kink formation requires thermal activation. However, semi-empirical (PM3) and desity functional theory (DFT) based computations have shown that the presence of nitrogen atoms can reduce the activation barrier for Stone-Wales transformation in fullerenes from 5.5 to 1.1 eV. [69] It is thus possible that the plastic deformation observed in the CN_x nanotubes tested occurred due to nitrogen assisted kink formation and motion.

4.2. Effect of Functionalization on the Mechanical Properties of Multi-Wall Carbon Nanotubes

The preparation, processing, and property tuning of carbon nanotubes (CNTs) reinforced nanocomposites require the dispersion and solubilization of CNTs, which in their pristine form are not soluble in most common organic solvents and water. Chemical modification of carbon nanotubes with functional groups has been found to be an excellent method to promote dispersion (by de-bundling) and also to improve their interaction with a matrix material via hydrogen or covalent bonding. In recent years, several approaches to achieve the functionalization of carbon nanotubes have been developed, in both molecular and supramolecular chemistry. These approaches include defect functionalization,

covalent functionalization of the side-walls, non-covalent exohedral functionalization and endohedral functionalization (see Figure 4.11). [70]

Besides a general improvement in the solubility and processibility, which can be achieved by all these approaches, sidewall functionalizations are particularly interesting since they significantly alter the structural and electronic properties of the SWNTs, yielding new nanotube derivatives with useful properties of their own. [71] However, modifying the hollow nanotubes by sidewall functionalization changes the surface structure since it results in the cleavage of carbon-carbon bonds along the graphite sidewall, therefore degrading the intrinsic mechanical properties of the nanotubes.

The direct addition of fluorine, hydrogen, aryl groups, nitrenes, carbenes, and radicals among others, to the side walls of pristine SWNTs have been reported in the past. [71] Fluorination as a covalent functionalization strategy is considered particularly important since it can improve dispersion considerably and because fluorine can be substituted with more complex addends, opening the way to more complex chemical functionalization of nanotubes for improved covalent interactions with matrix materials. In the earliest reports on sidewall functionalization chemistry, it was shown that fluorine substituents on SWNTs can be substituted by alkyl groups from corresponding Grignard and alkyllithium reagents, resulting in the covalent attachment of alkyls to the nanotube sidewalls through the C-C bonds. [72] These reactions were facilitated by weakened C-F bonds relative to those in alkylfluorides and a stronger electron-accepting ability of fluoronanotubes in comparison with that of pristine carbon nanotubes. In

addition to this, partial removal of functional groups from the surface of fluoronanotubes during processing with an epoxy matrix has been observed in the past, suggesting that fluorination could itself facilitate *in situ* direct covalent bonding between nanotubes and a matrix material, ultimately resulting in mechanical reinforcement of the composite. [73]

Thus far, no systematic experimental data can be found in literature that discusses the effects of fluorination on mechanical properties of CNTs. Hence, the novel technique described earlier was used to probe the mechanical properties of individual sidewall fluorinated MWNTs (F-MWNTs) by uniaxial tensile testing, *in situ*, within an SEM chamber.
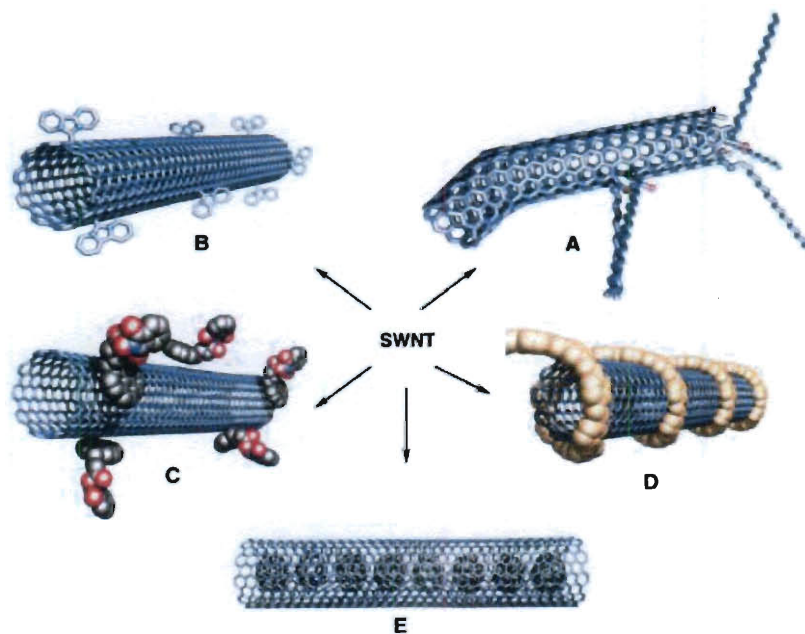
Figure 4.11 Functionalization possibilities for CNTs (SWNTs and MWNTs): A) defect-group functionalization, B) covalent sidewall functionalization, C) noncovalent exohedral functionalization with surfactants, D) noncovalent exohedral functionalization with polymers, and E) endohedral functionalization, for example with C60. [70]

4.2.1. Fluorination of MWNTs

A Mixture of 10 % elemental fluorine and 90% helium was used as the fluorinating agent for the MWNTs. This mixture along with additional helium gas feed was passed through a temperature controlled Monel flow reactor, held at 160 C, containing the nanotube sample. A 4% increase in the weight of the samples occurred after fluorination. X ray photoelectron spectroscopy conducted on the MWNTs showed the C:F ratio on the surface of the MWNTs to be 77.9:22.1 (see Figure 4.12). MWNTs grown catalytically via DLI-CVD (see Figure 4.13) as well as Mitsui^{TM} MWNTs (Mitsui corp., Japan, lot no. 05072001K28) were fluorinated using this procedure; DLI-CVD F-MWNTs were used as specimens for tensile testing experiments while Mitsui^{TM} F-MWNTs were used as specimens for single MWNT pullout experiments (see Chapter 5).
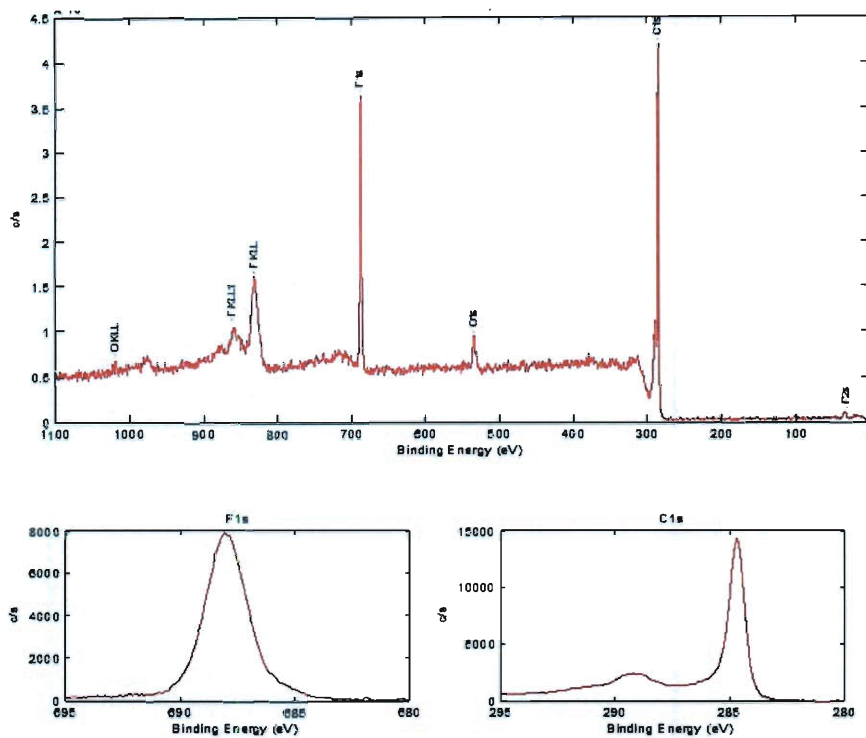
Figure 4.12 X ray photoelectron spectra for fluorinated MWNTs. (top) Survey scan and (bottom) F 1s and C 1s spectra; the C:F ratio on the surface of the MWNTs was found to be 77.9:22.1.
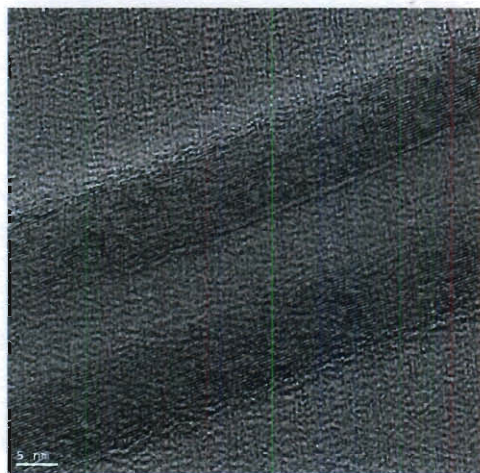
Figure 4.13 TEM image shows the morphology of a fluorinated DLI-CVD grown MWNT.
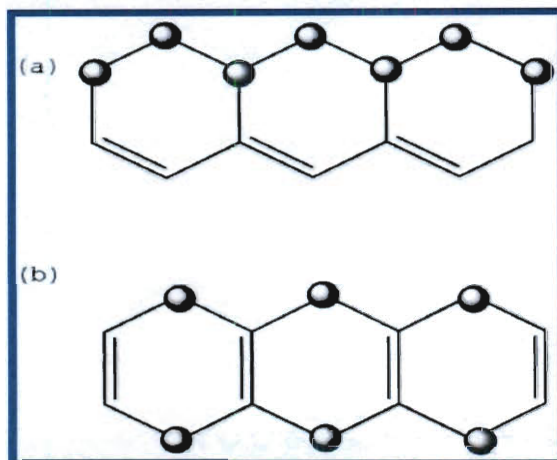
Figure 4.14 Proposed fluorine addition patterns on the fluoronanotubes: (a) 1,2-addition and (b) 1,4-addition. [74]

4.2.2. Tensile Testing: Results and Discussion

F-MWNTs were subjected to tensile testing using the procedure described in detail earlier (Section 4.1.2) (see Figure 4.15). As stated in the previous chapter, significant intershell cross-linking between the graphitic shells in the catalytically grown (DLI-CVD) pristine MWNTs was found to result in load sharing in a fashion that caused all graphitic shells to fracture in close proximity to one another, at the point of failure. SEM images of the fluorinated MWNTs tested, post failure, revealed similar flat (if somewhat corrugated) post failure surfaces (see Fig. 4.16); stress vs. strain curves were thus plotted assuming that the entire cross-section area of each fluorinated MWNT was load bearing (Fig. 4.17). The average strength and maximum load borne values (1.026 GPa and 6.35 μN) (see Table 4.2) were found to be much lower that of pristine MWNTs (2.134 GPa and 16.495 μN) (see Table 4.1).

In defect free MWNTs, sidewall fluorination would result in the formation of C-F bonds (or defects) on the outermost shell of the nanotubes. Hence, considerable degradation of mechanical properties would be expected to occur upon fluorination, in the case of initially defect free MWNTs without significant intershell crosslinking (only outermost wall would be load bearing). With regard to the catalytically grown MWNTs, known to possess high defect densities, fluorine incorporation could occur on more than one outmost graphitic shell of each nanotube. Thus, considerable changes in the mechanical properties would also be expected upon fluorination of such tubes. Comparison of the strength and maximum load borne values with those obtained by testing pristine MWNTs suggest that (a) significant degradation of the mechanical properties of catalytically grown MWNTs does occur upon sidewall fluorination and that (b) while the entire cross-section area of the catalytically grown MWNTs can be considered load-bearing owing to defect based cross-linking, load distribution among the shells is likely to be non-uniform, with the bulk of the tensile loads being borne by the outer shells.
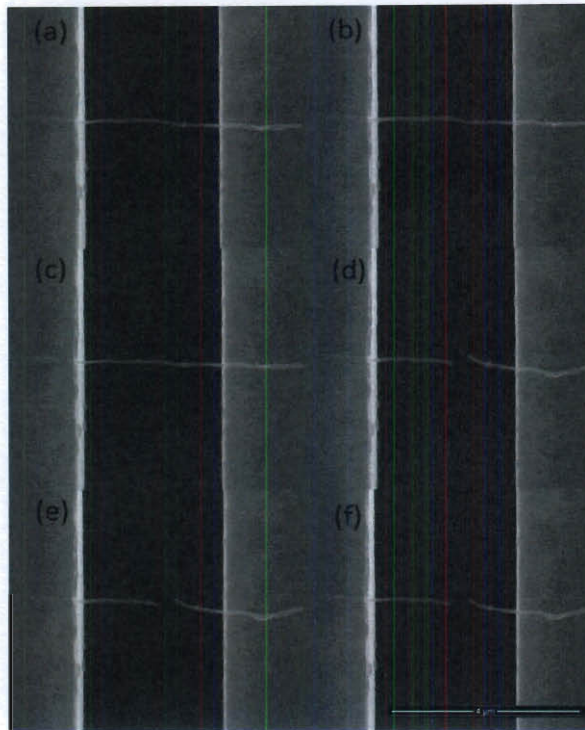
Figure 4.15 SEM snapshots show a fluorinated MWNT specimen undergoing deformation under a tensile load at (a) t=0, (b) t= 4, (c) t= 8, (d) t= 9, (e) t= 12 and (f) t= 18 seconds. Experiment was carried out at an indenter displacement rate of 10 nm/s.
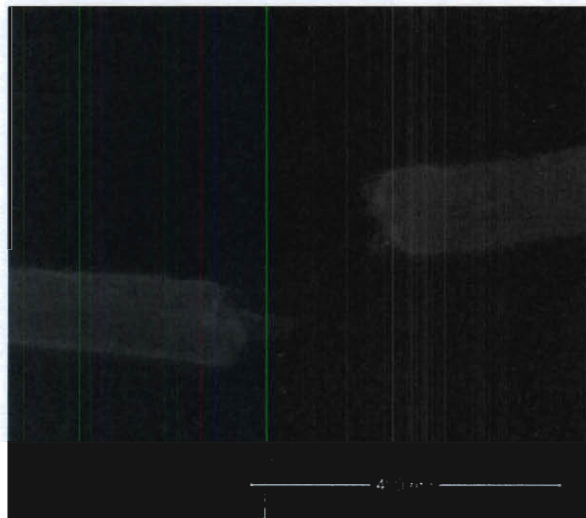
Figure 4.16 SEM image shows fracture surface of a fluorinated MWNT specimen.
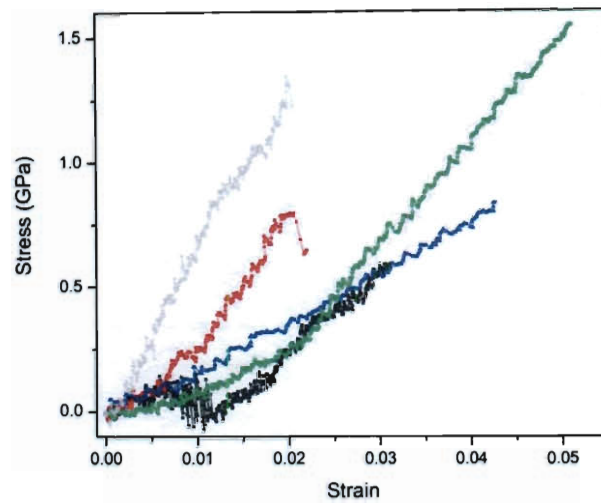
Figure 4.17 Engineering stress vs. strain curves for 5 fluorinated MWNT specimens

Table 4.2 Table shows the measured maximum load borne and the tensile strength values of 5 fluorinated MWNTs. All sample diameters were in the 70 to 100 nm range.

Sample	Maximum Load (nN)	Tensile strength (GPa)
1	4631	1.34
2	4906	0.80
3	11045	1.55
4	7677	0.84
5	3494	0.60

Table 4.3 Table compares MWNT strength values reported by other researchers to those measured using the novel technique. Values reported by others were computed assuming that only the outermost shell of each MWNT tested was load-bearing. If the strength values for MWNTs, tested using the novel technique were computed based this assumption, the numbers would be significantly higher (values highlighted in red).

MWNT growth technique/type (Report)	Strength (GPa)
Arc discharge (M.F. Yu et. al., 2000)	11-63
Arc Discharge (B.G. Demczyk et. al., 2002)	150
CVD (A.H. Barber et. al., 2005)	17.40-259.70
Arc Discharge (B. Peng et. al., 2008)	77-110
CVD grown pristine (this work)	0.99-3.72 (153.5-562.95)
CVD grown Nitrogen doped (this work)	1.13-2.33 (31.60-59.66)
CVD grown F functionalized (this work)	0.60-1.55 (98.95-211.54)

4.3. Conclusions

The mechanical properties of individual catalytically grown MWNTs have thus been studied by tensile testing, *in situ*, within a SEM chamber. Pristine and nitogen doped MWNTs were found to possess comparable strengths but markedly different load bearing abilities (see Table 4.3). Intershell cross-linking in the MWNTs was found to have positively contributed to their load-bearing abilities, especially in undoped MWNTs. In the case of nitrogen-doped MWNTs, fracture specimen analysis showed that inner wall arrays that merged with compartment layers were non-load-bearing. Also, while undoped MWNTs were found to fail via a brittle bond-breaking mechanism, the nitrogen doped MWNTs exhibited a certain degree of plasticity before failure. The repeated observation of kinks in the vicinity of the fractured surfaces led to the conclusion that the plasticity observed in these tubes was a result of kink motion. The presence of nitrogen in the graphitic sheets that formed the nanotubes was assumed to have catalyzed the

formation of kinks in these tubes. Finally, tests conducted on fluorinated MWNTs showed that a significant degradation of the mechanical properties occurred upon sidewall functionalization.

5. Mechanical Characterization of Interfaces in Multi-Wall Carbon Nanotube Reinforced Epoxy Composites

5.1. Introduction

Carbon nanotubes (CNTs) are low density materials that possess high strength and stiffness and thus offer promise as reinforcements for strong, stiff, tough and lightweight composites. However, the superior mechanical properties of CNTs alone do not guarantee nanocomposites with superior strength, stiffness and fracture toughness. Realization of these attributes also depends on two other factors: (a) the level of dispersion of the CNTs within the matrix and (b) the nature of the CNT-matrix interfaces formed (load transfer, adhesion, de-bonding and friction), a factor which literally dominates the overall performance of the nanocomposites.

Both MWNTs and SWNTs tend to aggregate to form bundles held together by weak van der Waals forces. There are a number of ways to promote debundling and improve dispersion of CNTs within a matrix; these include the use of ultrasonication, high shear mixing, the aid of surfactants, the use of chemical modification through functionalization, wrapping the tubes with polymer chains and combinations of these. Owing to the atomically smooth surface of carbon nanotubes and their limited ability to form covalent bonds with

a surrounding matrix material, whatever strength is exhibited by interfaces in pristine CNT reinforced composites is generally attributed to non-bond interactions such as van der Waals forces, electrostatic interactions and the confinement arising from thermal mismatch. [20] Fortunately, chemically disruptive or non-disruptive techniques (see Chapter 2) have been developed for altering the properties of the CNT-matrix interface. However, while dispersion levels can be determined with relative ease, interfacial adhesion characterization can be challenging owing to the small dimensions of CNTs and due to the magnitude of the forces and displacements involved.

5.2. CNT Reinforced Epoxy Composites

With regard to carbon nanotube reinforced polymer composites, significant improvements in the mechanical properties have been observed upon nanotube addition to thermoplastic and elastomeric matrices. For example, an 80 % improvement in tensile modulus was observed upon 1 % CNT addition to poly-(vinyl alcohol) (PVA). [29] In another work, a 3-fold increase in the Young's modulus was obtained upon addition of SWNT (1 wt. %) addition into an RTV silicone rubber matrix. [75] However, the reinforcement of epoxy resins by carbon nanotubes is considered problematic. Only marginal improvements or even a decrease in composite modulus have been observed, after the addition of CNTs into an epoxy matrix. [76] This is because (a) nanotubes tend to remain as entangled agglomerates within the epoxy matrix and homogeneous dispersions are not easily obtained. (b) On load application, nanotubes are typically pulled out from the matrix rather than fractured and play a limited reinforcement role.

Additionally, (c) processing difficulties that arise due to the significant increases in viscosity, caused by the addition of nanotubes into epoxy, result in inferior composite specimens. [73]

The strength of the CNT/epoxy interface can, in theory, be improved by the addition of carboxylic acid groups to their surface, as these groups can undergo esterification reactions with epoxy resins. Carbonyl groups as well as N alkylamino functionalities on nanotubes can also improve the interfacial strength of such composites. [73] However, as mentioned earlier, in order to accurately assess the effectiveness of a surface functionalization technique, it would be necessary to directly (and reliably) characterize the mechanical properties of the interface.

5.3. Single fiber Pullout Experiments

Single fiber pullout experiments have been used by researchers, since the 1950s, to study the nature of the adhesive forces that act at the filler matrix interface in composites (see Figure 5.1). This is because the experiments are considered a direct and quantitative method for the localized characterization of interfaces. An advantage of the pullout test is that in addition to the interfacial bond strength and interfacial toughness, other interfacial properties such as the matrix shrinkage pressure on the filler, the interfacial shear stress and the work done in pulling out the filler from the matrix, can be determined. The last factor is important, since the significant increase in fracture toughness of fibrous composites has been attributed to the fiber pullout process during failure.

A considerable amount of effort has been expended into attempts to perform quantitative CNT pullout experiments. In the past, single MWNT pullout experiments have been successfully carried out using an atomic force microscope (AFM), [42] or using an AFM probe tip within a SEM chamber. [43] However, there are several major issues associated with AFM and AFM probe based single CNT pullout experiments. CNTs must be attached to the end side of AFM tips at an angle with the vertical axis in order to perform such experiments, thus leading to misalignment; the misalignment can be exacerbated by natural deviation from the vertical direction during loading of the cantilever-tip assembly. With regard to AFM probe assisted experiments, the extraction of a force signal is based upon estimates of cantilever stiffness and involves the determination of cantilever deflection from low resolution SEM images, both of which can lead to errors. Lastly, CNT embedment depth within the matrix cannot be controlled or estimated easily when using these techniques.
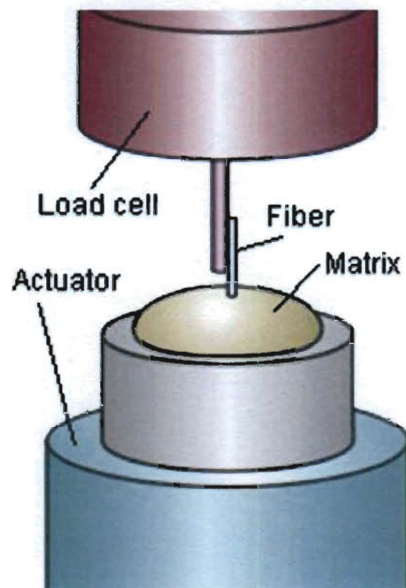
Figure 5.1 Schematic shows setup for a typical single fiber pullout experiment.

5.3.1. Single MWNT Pullout Experiments using Novel Technique

By employing a novel sample preparation scheme (see Figure 5.3), single MWNT pullout experiments can be performed within a scanning electron microscope (SEM) chamber using the experimental setup introduced in Chapter 3. Table 3.2 provides a list of advantages the novel techniques possesses over AFM based techniques for conducting similar experiments. The technique was thus used to directly characterize the mechanical properties of the MWNT (pristine and fluorinated)/Epoxy interface.

The micro-fabricated devices provide a robust platform for performing single fiber pullout tests. Misalignment issues are minimal since the experiments are conducted within a SEM chamber and pullout was monitored in real time. The technique allows for the facile implementation of desired composite processing conditions (for e.g. high temperature curing). Also, the pullout specimen preparation technique employed allows a certain degree of control over CNT embedment depth.

5.3.2. Experimental Methods

6 ± 0.5 µm thick devices (geometry shown in Figure 3.7) were used for all the single MWNT pullout experiments. A portion of each sample stage shuttle was first coated with a thin layer of 10:1 epoxy (Epon 828, diglycidyl ether of bisphenol-A) + curing agent (Epikure 3200, aminothylpiperazine- an unmodified aliphatic amine) mixture. A droplet from a sonicated suspension of Mitsui™ MWNTs (see Figure 5.2) in toluene was deposited onto a Si wafer coated with a 50 nm thick layer of titanium. Individual MWNTs, 75 ± 20 nm in diameter with

approximately 65 shells and roughly 10-15 um long and hence visible under an optical microscope, were "picked up" and placed across the shuttles using micromanipulators housed within a probe station. The embedment depths of the MWNTs were roughly estimated at this juncture by observation within a SEM. This was done in order to avoid any errors in the analysis that might arise from nanotube failure within the matrix during pullout. A large droplet of epoxy (mixed with curing agent) was subsequently dropped onto a segment of the MWNT that was on one of the sample stage shuttles. The droplet upon curing (at room temperature) embedded this segment of the MWNT. The other end the MWNT was clamped onto the device by electron beam induced deposition of platinum (using a gas injection system) within a FIB chamber (FEI Strata DB 235, FEI corp.). This step involved the focusing of the SEM/FIB electron beam on a desired area (usually a 0.5 μm x 0.5 μm square), insertion of the gas injection needle followed by the opening of the needle valve that let the platinum (Pt) precursor into the SEM/FIB chamber. Pt deposition occurs at the focus spot. This process inadvertently results in some Pt deposition on the exposed regions of the MWNT. However, the presence of the epoxy droplet ensures that no Pt sheathing of the embedded section of the MWNT occurs. The specimen was post cured at 80 C for 2 hours before the pullout experiment was conducted. Note that the use of the room temperature cure step followed by high temperature post-cure was preferred over the usage of a single high temperature cure step in order to minimize the internal stresses that would develop as a result of elevated temperature cures. These stresses generally develop from shrinkage of the epoxy

on polymerization or mismatch in thermal expansion coefficients between the substrate and resin. The MWNT pullouts were performed within the SEM equipped with an InSEM® Indenter system. A blunt berkovich nanoindenter tip was used to perform the indentations. The experiments were conducted at an indenter tip displacement rate of 10 nm/s with the load vs. displacement data being collected at the rate of 25 Hz. The maximum load applied on the device varied between 0.1 to 1 mN. Once this value was reached, the load was held constant for 0.5 seconds. This was followed by an unloading step at the aforementioned displacement rate. A thermal drift correction hold was conducted at about 0.1-1 % of the maximum applied load for about 50 seconds in order to account for small amounts of thermal expansion or contraction in the test material and/or indentation equipment.
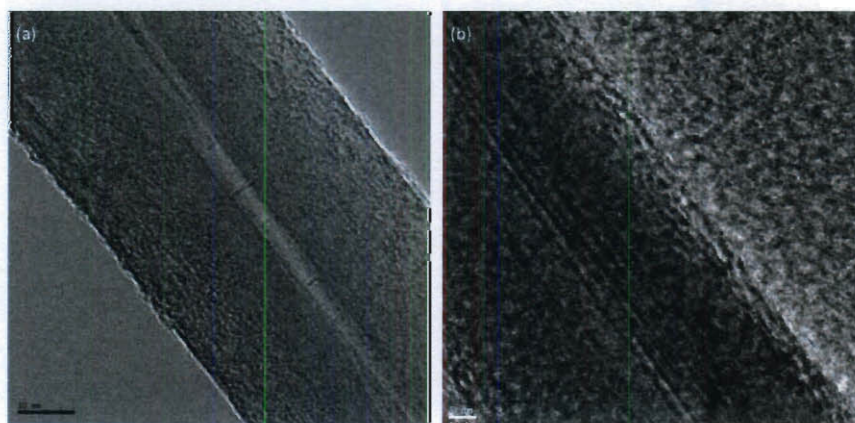
Figure 5.2 TEM images show the surface morphology of (a) a single pristine Mitsui[TM] **MWNT and (b) a single fluorinated Mitsui**[TM] **MWNT.**
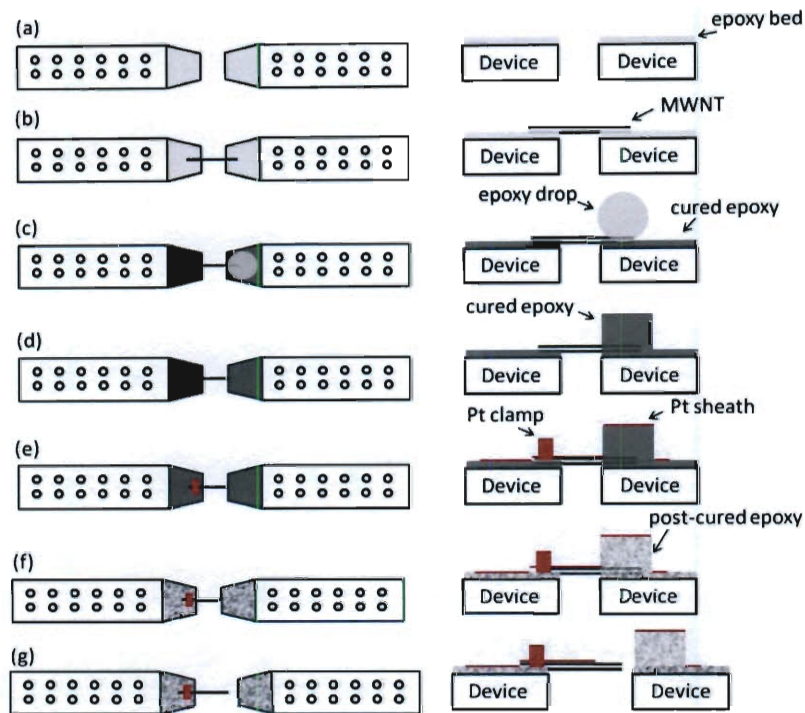
Figure 5.3 Sample preparation procedure; for each step undertaken, the top and side views of the sample stage shuttles shown side by side. (a) The ends of the sample stage shuttles are first coated with a thin layer of the epoxy, (b) an individual MWNT is placed across the gap, (c) a single droplet of epoxy is dropped onto one of the sample stage shuttles, (d) the droplet of epoxy upon curing at room temperature embeds one end of the MWNT, (e) the MWNT is clamped close to the other end by Pt deposition, (f) the specimen is post cured and finally (g) the pullout experiment is performed.
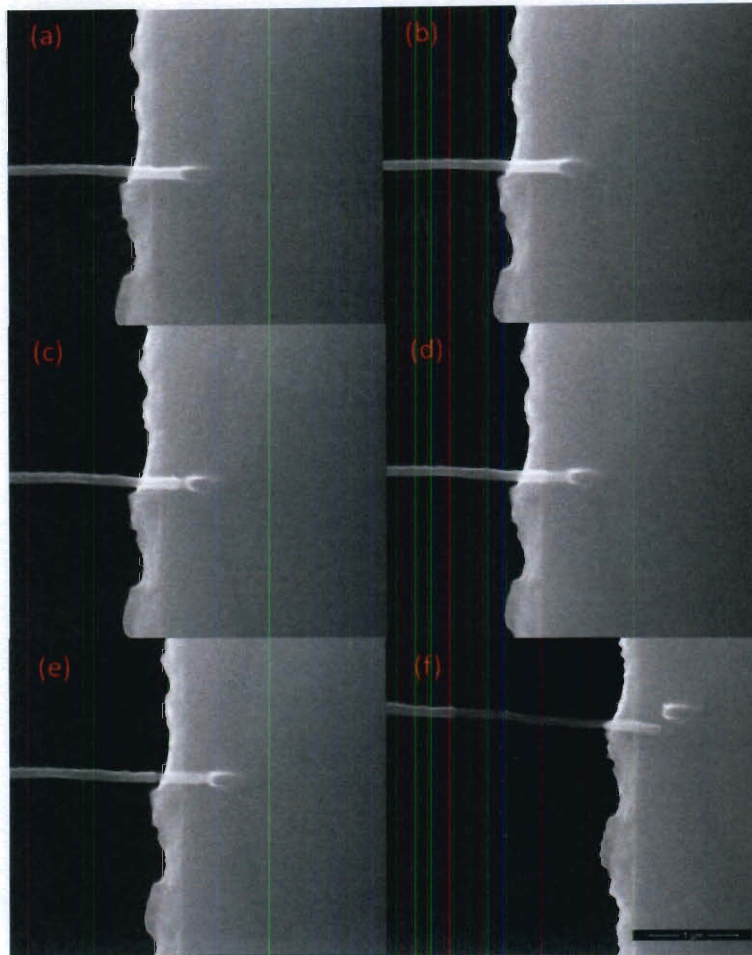
Figure 5.4 SEM snapshots show a single pristine MWNT as it pulls out of an epoxy matrix at (a) t=0, (b) t=10, (c) t=19, (d) t=30, (e) t=70 and (f) t=300 seconds. Pullout experiment was conducted at an indenter displacement rate of 10 nm/s.

5.3.3. Results and Discussion

The pullout specimens used in this study comprised of individual pristine (and subsequently fluorinated MWNTs) embedded in Epon 828 epoxy films. Epon 828 was chosen as the matrix material since the resin is routinely for formulation, fabrication and fusion technology. Four types of failure generally occur during a typical single-fiber pullout test. These include (i) specimen failure due to matrix failure away from the fiber-matrix interface, (ii) specimen failure by

fiber fracture along the external free length of the fiber, (iii) partial debonding followed by specimen failure due to fiber fracture along the embedded length of the fiber and (iv) specimen failure due to complete debonding and extraction of the debonded fiber from the matrix. The first three types of failure represent unsuccessful pullout tests and data from specimens that exhibit these types of failure are not included in pullout analyses. With regard to MWNT pullout from epoxy, the first three types of failure were generally not observed during the experiments. Unsuccessful experiments were generally the result of the failure of platinum clamps or due to pullout occurring from platinum depositions (see Figure 5.5 (b)). Often, during pullout experiments fracture of the platinum sheath around the exposed parts MWNTs made it impossible to validate pullout from the polymer matrix (see Figure 5.5 (a)). Such pullouts were considered unsuccessful and were not included in the analyses. The pullout experiments were thus characterized by a low success rate (< 10 %).
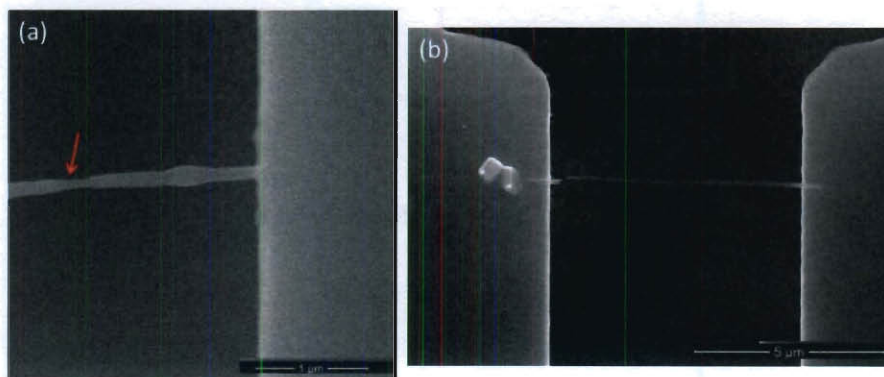
Figure 5.5 Unsuccessful pullout experiment characteristics. (a) SEM image shows the occurrence of fracture (red arrow) of the platinum sheath around the exposed part of a MWNT. (b) SEM image shows MWNT pullout from a platinum clamp.

Successful experiments were typified by the observation of the pullout of the MWNT specimens from the epoxy matrix (SEM snapshots extracted from the video recording of an illustrative test shown in Fig. 5.4) upon application of μN-level loads. Load vs. extension traces, extracted from their corresponding nanoindenter load vs. displacement curves via response subtraction (see Chapter 4 and Figure 5.6), were found to be linear for short MWNT embedment depth values and non-linear (generally bilinear) for larger embedment depth values. Note that such behavior can be considered qualitatively consistent with the predictions of continuum fracture mechanics models. Figure 5.9 shows a plot of the maximum pullout force values for a set of 15 samples, obtained as function of MWNT embedment depth. As is generally the case with single fiber pullout experiments, the data points were found to exhibit a considerable degree of scatter with the maximum pullout force values comparable to those reported by Barber et al. [43] The aforementioned authors conducted similar single fiber pullout experiments with MWNTs embedded in a two-part fast cure epoxy (Poxipol™) matrix. Interestingly, they reported that a transition in the failure mode, from interfacial failure to nanotube fracture, occurred at large MWNT embedment depth values; such a transition was not found to occur during the course of our experiments i.e. all embedded MWNT specimens tested were found to undergo complete pullout from the epoxy matrix and nanotube failure did not occur during any of the experiments within the embedded region or along the free length of the MWNTs. The pullout force values were used to calculate the nominal shear strength of the interface (IFSS), defined as

$$\tau = \frac{P_c}{2\pi r l} \qquad (1)$$

where P_c is the experimentally measured maximum pullout force, r is the MWNT radius and l is the embedment depth. It was observed that τ values exhibited significant scatter (see Table 5.1 and Table 5.3), and that its average value of 6.24 ± 3.6 MPa was one order of magnitude lower than the tensile strength (52 MPa) of the polymer matrix and orders of magnitudes lower than the strength of the MWNTs (see Figure 5.10). Hence interfacial failure and MWNT pullout would be expected to occur upon sufficient load application for all embedments as was the case. It is worth noting that single-fiber pullout experiments are inherently prone to data scattering. The origin of the data scattering had been assumed to be experimental error associated with pullout testing, though fracture mechanics analysis suggests that the data scattering is also inherent in the specimens themselves. The scatter apparently becomes particularly pronounced when nanoscale fibers are used as reinforcements. Similar experiments were conducted in the past revealed a similar scatter in the data. [42, 43] It is postulated that the scatter arises partially due to the fact that minor variations that occur during specimen preparation have a substantial effect on the values of maximum pullout load obtained.
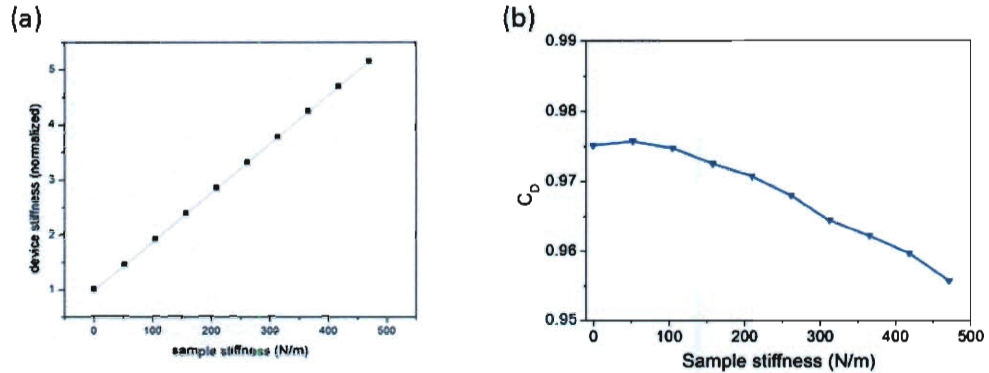
Figure 5.6 (a) Device stiffness (normalized) vs. sample stiffness curve and (b) C_D vs. sample stiffness curve for 6 µm thick devices (geometry shown in Figure 3.7). The curves were used to estimate C_D for all pullout experiments.

The lack of dependence of pullout capacity on embedment depth implied that the pullout process was not ductile (a constant shear stress equal to τ is not developed along the interface), but instead is associated with brittle cracking. This crack propagation scenario was supported also by the shapes of the load-displacement plots. As mentioned earlier, fibers with short embedments pulled out as a result of catastrophic (unstable) propagation of an initiated interface crack and thus exhibited a linear pre-peak response (see Fig. 5.8 (a) and Table 5.1). Deep embedments, however, enabled stable crack extension and thus produced nonlinear load-displacement responses prior to peak load. (see Fig. 5.8 (b) and Table 5.1).

(a)
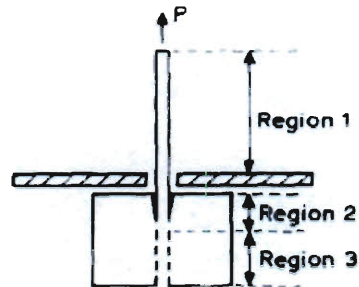
(b)
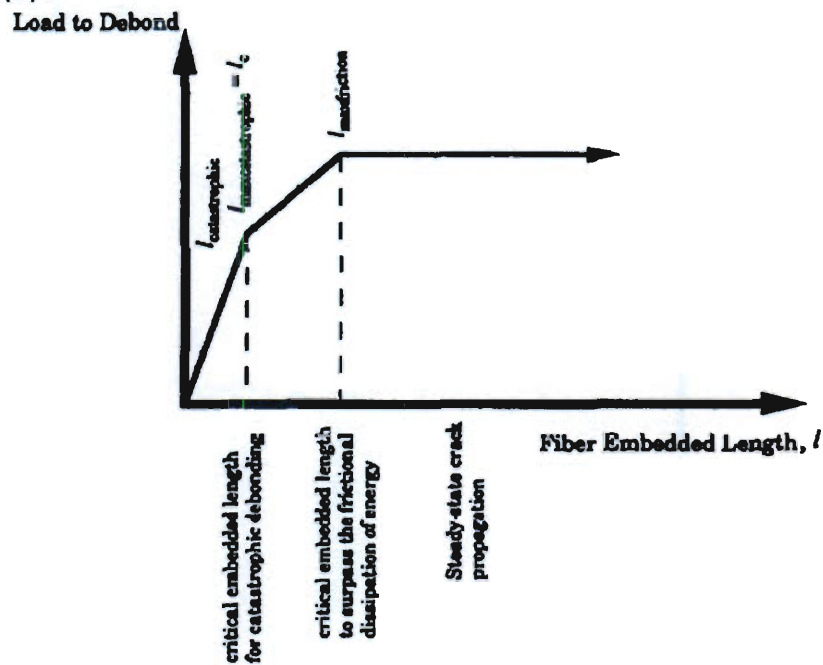
Figure 5.7 (a) Schematic illustration of single filament pull-out specimen with three regions defined. Region 1-fiber alone, Region 2-fiber and matrix debonded at the interface and Region 3-fiber and matrix bonded at the interface. [77] (b) Theoretical pullout force (maximum) vs. embedment depth (fiber embedded length) plot. [84] As the embedded length increases, the required load to debond also increases (linear relationship). Once the embedded length of fibre increases beyond $l_{maxcatastrophic}$, frictional effects alter the

relationship between load to debond and embedded length. For embedded lengths greater than $l_{maxfriction}$, Poisson's forces come into play and the load to debond becomes independent of embedded length.

The results suggested that the pullout experiments could provide the interfacial fracture energy, G_c for the system using the approximate fracture mechanics model developed by Jiang and Penn. [77] To analyze fiber/matrix debonding in the composite specimen the authors applied the energy balance principle to the interracial crack propagation process. They postulated that the strain energy released from the system must not only supply the energy required to propagate a crack through the bonded interface (region 3), but also must supply the energy dissipated through friction in the debonded region (region 2) (see Figure 5.7 (a)). Thus

$$\frac{\partial U_1}{\partial a} + \frac{\partial U_2}{\partial a} + \frac{\partial U_3}{\partial a} = \frac{\partial W_f}{\partial a} + 2\pi r G_c$$

where U_1, U_2 and U_3 are the total strain energies stored in Regions 1, 2 and 3, W_f is the work of friction in the debonded area, $2\pi r$ is the circumference of the interface and a is the crack length at the interface. Neglecting the effects of matrix compression and assigning a zero value of friction coefficient to the analytical formulae outlined in ref. 77 leads to the following formula relating the critical load for crack propagation, P_c, the Young's modulus of the fiber (matrix), E_f (E_m), the Poisson's ratio of the matrix, v_m, the radial distance from the fiber axis at which the shear stress in the matrix reduces to zero, R, the embedment depth, l, the initial crack length at the interface, a_o and the MWNT radius, r

$$P_c = \frac{2\pi r \sqrt{r E_f G_c}}{\sqrt{1 + \csc h^2 \left(n \dfrac{l - a_o}{r} \right)}} \qquad (2)$$

where n is a utility constant defined as

$$n = \sqrt{\frac{E_m}{E_f (1 + \upsilon_m) \ln \dfrac{R}{r}}}$$

Note that for the purpose of the calculations, the effects of friction in the debonded regions of the nanotubes were ignored because the load required to pull the nanotube through the hole in the matrix after debonding occurred was found to be consistently below the detectable range of the novel technique. This, however, does not mean that frictional energy dissipation was negligible. Also, the effects of matrix compression were ignored since the cross sectional area of the matrix (found to be equal to about 80 μm^2 for a representative specimen) was much larger than that of the nanotubes (<100 nm diameter).

Maximum pullout force values corresponding to non-linear load-displacement responses, i.e. those associated with deep embedments, were assumed to equal to the load required to debond the MWNT from the epoxy plus an amount of energy dissipated by frictional effects between the MWNT and the epoxy over the debonded length i.e. the values were > P_c and could be used for determining G_c. Thus, in theory, only the set of measured values of maximum pullout force corresponding to pullouts characterized by a linear load-displacement response could be used to compute the value of G_c using equation (2). However, maximum pullout loads associated with short embedments were known to be susceptible to errors, such as those introduced by the presence of

initial cracks (formed during specimen preparation or handling, initial cracks that are a large fraction of the embedment depth can reduce the value of P_c substantially). [77] Equation (2) could thus be used to reliably estimate the value of G_c only when the embedment depth is equal to a threshold value, l_{th}, for which the maximum pullout force value is insensitive to initial crack size and friction ($l_{maxcatastrophic}$ in Figure 5.7 (b)). In other words, to determine G_c, one would need to ascertain the point of transition between the catastrophic interfacial failure mode and the subcritical interfacial crack extension mode (see Figure 5.9).

(a) (b)
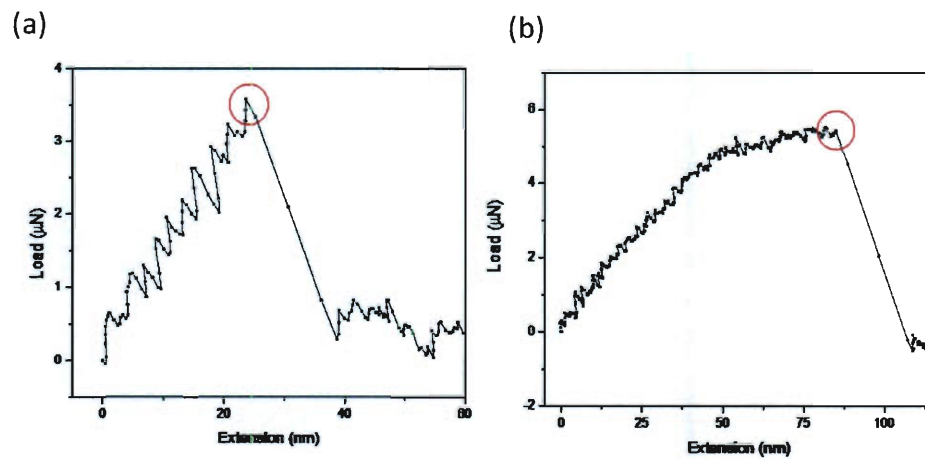
Figure 5.8 Representative load-extension curves for (a) a pristine MWNT specimen with a small embedment (2.55 μm) and (b) a pristine MWNT specimen with large embedment (6.38 μm). Circles indicate the maximum pullout load values.

Table 5.1 Interfacial properties ascertained from single pristine MWNT pullout experiments

Embedment Length (μm)	MWNT Outer Diameter (nm)	Maximum Pullout Force (μN)	Interfacial Shear Strength, (MPa)	Nature of Load-Displacement response
1.25	64.0	0.46	1.84	Linear
1.85	94.4	6.12	11.17	Linear
2.35	95.7	1.7	2.41	Linear
2.55	93.7	3.58	4.77	Linear
2.63	77.3	7.95	12.45	Not Clear
3.69	70.3	4.55	5.56	Non-Linear
3.73	71.8	3.10	3.69	Not Clear
3.93	95.5	11.75	9.98	Not Clear
4.58	70.0	2.88	2.86	Non-Linear
5.79	53.5	6.61	6.8	Non-Linear
6.29	83.5	15.48	9.39	Non-Linear
6.38	64.1	14.01	10.91	Non-Linear
6.38	61.3	5.51	4.49	Non-Linear
8.14	69.3	4.68	2.64	Non-Linear
8.22	67.5	8.12	4.66	Non-Linear

116
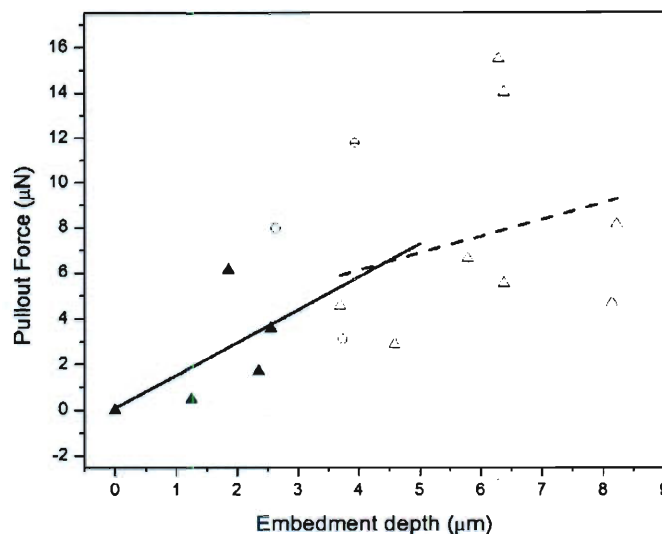
Figure 5.9 Maximum pullout force versus nanotube embedment depth (pristine MWNTs). The symbol (▲) indicates points that correspond to embedments that exhibited a linear pullout load-displacement response. The symbol (Δ) indicates points corresponding to deep embedments that exhibited a non-linear pullout load-displacement response. The symbol (Θ) indicates points corresponding to embedments that did not exhibit a clearly linear or non-linear pullout load-displacement response. Also shown are the linear fits that were applied for the points indicated by (▲) (solid line) and the points indicated by (Δ) (dashed line); their point of convergence was used to determine l_{th} (4.42 μm), and its corresponding maximum pullout force value P_c (th) (6.42 μN).

The average Young's modulus value of the pristine MWNT specimens was obtained by performing tensile tests using the novel technique (procedure outlined in Chapter 4 was used to conduct experiments on Mitsui MWNTs; Pt clamps were used to anchor specimens on devices) (see Figure 5.10). Assuming the entire cross sectional area of each nanotube was load bearing (a somewhat reasonable assumption since most catalytically grown MWNTs possess intershell

crosslinks that lead to considerable intershell load transfer), E_f was found to be equal to 200 GPa. The modulus of unreinforced Epon 828 (mixed with Epikure 3200 in a 10:1 ratio) resin was measured using tension experiments conducted on dog-bone shaped resin specimens (average E_m = 1099 MPa) . The Poisson's ratio of the resin was set equal to 0.33. [78]

The diameters of the MWNTs were measured as 75 ± 20 nm. Assuming a zero length of the initial crack length at the interface, and a stress transfer parameter R/r value ranging from 2 (a value typical for weak interfaces) to 9 (a value that would be typical for a strong interface) [79, 80], Equation (2) provided an interfacial fracture energy value for the pristine MWNT-Epon 828 interface within the range $0.05\text{-}0.25\ J/m^2$. Note that the choice of the value of the stress transfer parameter R/r did not significantly affect the value of G_c; the uncertainty in fracture energy arose primarily from the variation in the nanotube diameter.

The value of G_c obtained from the pullout experiments was approximately two orders of magnitude lower than that of other engineered composite materials (see Table 5.4).[81] It was also considerably lower than the values reported for nanotube pullout from a polyethylene butene matrix (4-70 J m^{-2}).[42] Note that the nominal shear strength measured was also considerably lower than the values reported for the MWNT-epoxy (Poxipol™ glue) system [43] (22.26 MPa, based on AFM tip assisted single MWNT pullout experiments), the MWNT-polyurethane system [82] (500 MPa, based on stress induced fragmentation experiments), the carbon nanofiber-Epikote 862 system [83] (170 MPa, using a probe assisted pullout technique) and the MWNT-polystyrene system [20] (160

MPa, value obtained via molecular mechanics simulations and elasticity calculations). The low values of G_c and nominal shear strength illustrate the weak nature of the non-bond interactions that bind pristine MWNTs to the Epon 828 epoxy matrix. Nano-mechanical interlocking, covalent bonding and polymer chain wrapping, three factors that generally play a significant role in filler matrix bonding, were assumed to have contributed minimally to adhesion at the pristine MWNT-Epon 828 interface.
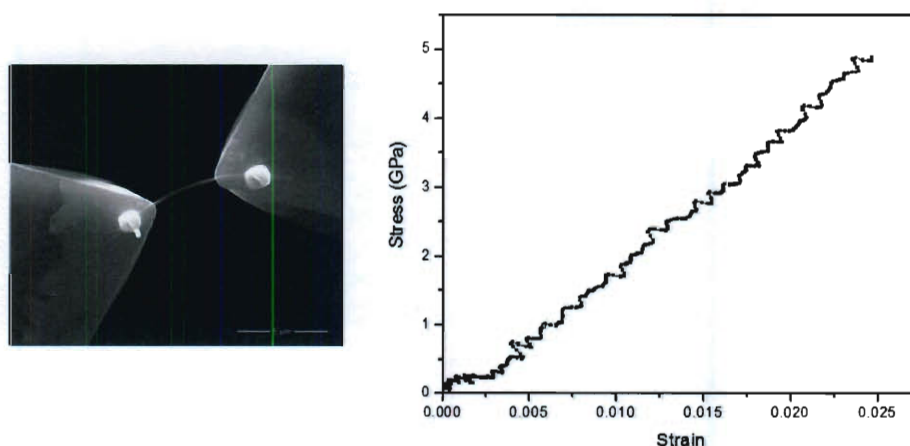
Figure 5.10 (Left) A Mitsui^{TM} MWNT tensile sample (Pt depositions were used to clamp specimens). (right) Representative stress-strain curve for a Mitsui^{TM} MWNT specimen, tensile tested using the technique outlined in Chapter 4; the Young's modulus was found to be approximately 200 GPa.

Samples, similar to the ones prepared for the pristine MWNT pullout experiments, were prepared for fluorinated MWNT pullout experiments (fluorination procedure outlined in Chapter 4). 13 successful pullout experiments were conducted (see Figure 5.11) and their load vs. extension traces, extracted from their corresponding nanoindenter load vs. displacement curves, were used to ascertain the interfacial strength of the composite system. Pullout experiments in

which the embedment depths were greater than 6 μm or lower than 3 μm were unsuccessful. The average value of the nominal interfacial shear strength, τ, for the F-MWNT/Epon 828 interface (19.8 ± 7.78 MPa), calculated using Equation (1), was found to be larger than that for the pristine MWNT/Epon 828 interface (6.24 ± 3.6 MPa) (see Table 5.3).

As with the case of the pristine MWNTs, fluorinated MWNTs with short embedment depths (lower than 6 μm) pulled out as a result of catastrophic (unstable) propagation of an initiated interface crack and thus exhibited a linear pre-peak response (see Fig. 5.12 (a) and Table 5.2). Deep embedments, however, enabled stable crack extension and thus produced nonlinear load-displacement responses prior to peak load (see Fig. 5.12 (b) and Table 5.2). These results essentially suggested that the pullout experiments could provide the interfacial fracture energy for the fluorinated MWNT/Epon 828 interface using the approximate fracture mechanics model developed by Jiang and Penn. [77] The effects of matrix compression and friction were neglected and thus equation (2) was used, once again, to ascertain the interfacial fracture energy, G_c, for the system (see Table 5.2). It must again be noted that the maximum pullout force values corresponding to non-linear load-displacement responses, i.e. those associated with deep embedments (the two points indicated by Δ in Figure 5.13), were assumed to equal the load required to debond the fluorinated MWNT from the epoxy plus an amount of energy dissipated by frictional effects between the MWNT and the epoxy over the debonded length. Thus, only the set of measured values of maximum pullout force corresponding to pullouts characterized by a

linear load-displacement response were used to compute the value of interfacial fracture energy G_c. However, since short embedments were known to be susceptible to errors introduced by the presence of initial cracks, the G_c values corresponding only to embedment depths 5.65 µm and 5. 74 µm were considered reliable. This is because these two embedment depth values can be assumed to be closest to the threshold value, l_{th}, since deeper embedments resulted in non-linear load vs. displacement responses. The actual point of transition between the catastrophic interfacial failure mode and the subcritical interfacial crack extension mode i.e. $l_{th,}$ could not be ascertained in this case, owing to the paucity of successful pullouts corresponding to deep embedments.
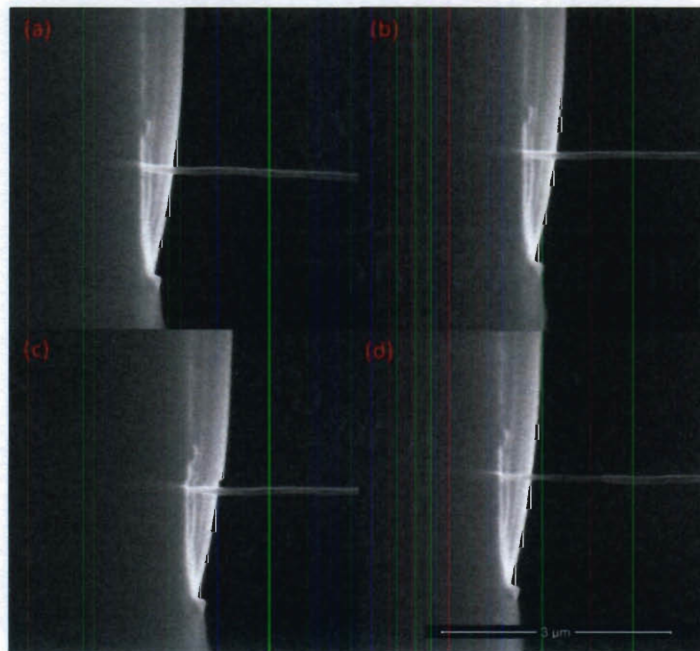
Figure 5.11 SEM snapshots show a single fluorinated MWNT as it pulls out of an epoxy matrix at (a) t=0, (b) t=, 8(c) t=16 and (d) t=144 seconds (during a pullout experiment). Pullout experiment was conducted at an indenter displacement rate of 10 nm/s.

With regard to the G_c calculations using equation (2), it must be mentioned that the average Young's modulus value for the fluorinated MWNT specimens was not obtained by performing tensile tests on the nanotubes. Instead, the magnitude of the reduction in Young's Modulus brought about by fluorination was estimated based on the experiments conducted on DLI-CVD MWNTs (see Sections 4.1.4 and 4.2.2). With regard to the DLI-CVD MWNTs, a 35% reduction in the Young's Modulus was observed upon fluorination (average apparent Young's Moduli for pristine DLI-CVD MWNTs was about 54.3 GPa; this value reduced to 35.3 GPa upon sidewall fluorination). The Mitsui[TM] MWNTs were thus assumed to have degraded similarly and hence their Young's Modulus value was set to 130.16 GPa.

The two reliable values of G_c, 1.501 J/m^2 and 1.916 J/m^2, were found to about one order of magnitude higher than that for the pristine MWNT/Epon 828 interface and thus comparable to the values reported for nanotube pullout from a polyethylene-butene matrix. [42] The values were still however, approximately one order of magnitude lower than that for engineered composite materials (see Table 5.4). [81] Fluorine on the sidewalls of F-MWNTs has been known to be readily displaced by alkylidene amino groups. There have been reports that suggest that fluorinated CNTs react *in situ* with amine curing agents (such as Epikure 3200) during a high temperature curing processes (130 C and above), thus establishing covalent linkages with an epoxy matrix. [73] However, since the pullout specimens were room temperature cured and subsequently post cured at 80 C, it was unlikely that any significant covalent bonding occurred between the

F-MWNTs and the epoxy matrix. Since any enhancement in the polymer's chain wrapping ability was also unlikely (owing to the large diameters of the MWNTs), the improvement in the interfacial adhesion was assumed to have occurred due to an increase in the surface roughness of the MWNTs brought about by fluorination, which in turn augmented the level of nanomechanical interlocking at the CNT/Epoxy interface.
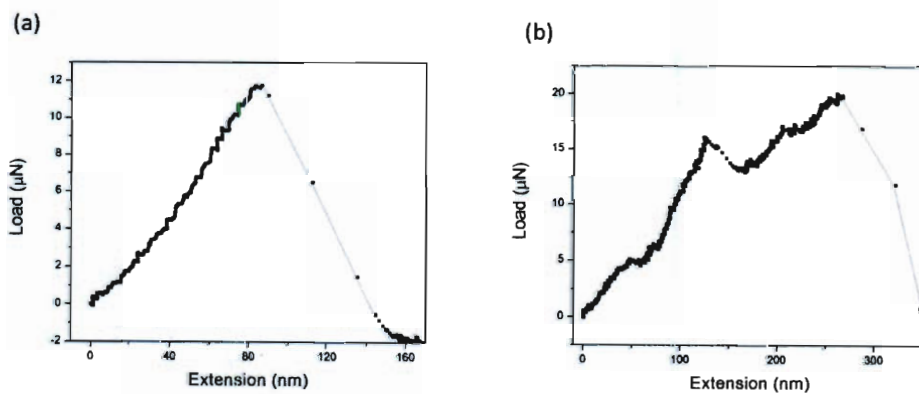
Figure 5.12 Representative load-extension curves for (a) a fluorinated MWNT specimen with a small embedment (3.36 μm) and (b) a fluorinated MWNT specimen with large embedment (6.01 μm).

Table 5.2 **Interfacial properties ascertained from single fluorinated MWNT pullout experiments. The two most reliable G_c values determined are highlighted in red. (N.A. = not applicable)**

Embedment Length (μm)	MWNT Outer Diameter (nm)	Maximum Pullout Force (μN)	Interfacial Shear Strength, (MPa)	Nature of Load-Displacement response	Interfacial Fracture Energy, G_c (J/m^2)
3.13	64.1	11.51	18.27	Linear	0.784
3.35	76.3	27.31	34.03	Linear	2.617
3.36	90.7	11.73	12.28	Linear	0.287
3.44	78.0	10.54	12.51	Linear	0.365
3.46	78.9	29.19	34.05	Linear	2.704
3.52	91.0	28.02	27.86	Linear	1.624
3.58	88.9	15.84	15.85	Linear	0.557
4.15	107.2	21.70	15.48	Linear	0.596
5.47	98.8	17.24	10.16	Not Clear	N.A.
5.65	113.8	37.67	18.67	Linear	1.501
5.74	77.5	23.92	17.12	Linear	1.916
6.00	90.6	23.60	13.82	Non-Linear	N.A.
6.01	59.2	19.78	17.70	Non-Linear	N.A.
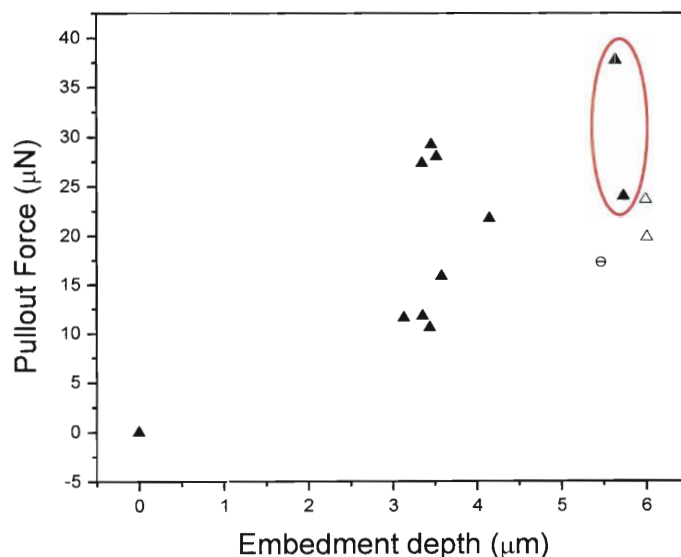
Figure 5.13 Maximum pullout force versus nanotube embedment depth (fluorinated MWNTs). The symbol (▲) indicates points that correspond to embedments that exhibited a linear pullout load-displacement response. The symbol (Δ) indicates points corresponding to deep embedments that exhibited a non-linear pullout load-displacement response. The symbol (Θ) indicates points corresponding to embedments that did not exhibit a clearly linear or non-linear pullout load-displacement response. The encircled points provided the most reliable values of G_c.

Table 5.3 Table compares MWNT/carbon nanofiber-polymer IFSS values reported by other researchers to those measured using the novel technique.

System (Report)	IFSS (MPa)
MWNT-Poxipol™ epoxy, (A.H. Barber et al., 2006)	22.26
MWNT-polyurethane (H.D. Wagner et al., 1998)	500
MWNT(60-70 nm diameter)-Polyethene-butene (A.H. Barber et al., 2004)	~15
Carbon nanofiber-Epikote (M.P. Manoharan et al., 2009)	170
Mitsui™ MWNT-Epon 828 (this work)	6.24
Fluorinated Mitsui™ MWNT-Epon 828 (this work)	19.8

Table 5.4 Table compares G_c values reported by other researchers for comparable systems to those measured for the MWNT-epoxy system using the novel technique.

System (Report)	Fracture Energy (J/m²)
Glass fiber-vinyl ester (S. Zhandarov et al., 2001)	16-34
MWNT-polyethene butene (A.H. Barber et al., 2004)	4-70
Mitsui™ MWNT-Epon 828 (this work)	0.05-0.25
Fluorinated Mitsui™ MWNT-Epon 828 (this work)	1.501/1.916

5.4. Macro-scale Testing

In order to further assess the effects of chemical functionalization on the reinforcement efficiency of CNTs, macro-scale tests were conducted on dog-bone shaped composite specimens. Pristine and F-MWNTs were incorporated into an Epon 828 matrix and the mechanical properties of the composites were tested using a micro-tensile tester.

Dog-bone shaped samples (see Figure 5.14 (a)) were prepared via the following procedure: Epon 828/Epicure 3200 (weight ratio: 10:1) mixtures were stirred and cast into dog-bone shaped molds. The samples were cured at room temperature for 2 hours followed by a high temperature (80 C) post-cure for 2 hours. 0.5% (by weight) pristine and fluorinated MWNTs (Mitsui™) were used reinforcements; the MWNTs were first dispersed in toluene followed by incorporation of dispersions into the epoxy/curing agent mixtures. The solvent was completely evaporated before casting of mixtures into molds. It must be noted that the composites, after post-curing, were found to be in a glassy state at room temperature. Tensile tests were performed in the dog-bone shaped

specimens using a Gatan™ Deben micro-tester (Gatan, Inc., Pleasanton, CA) (see Figure 5.14 (b)). The tensile experiments were conducted at a displacement rate of 0.5 mm/min.
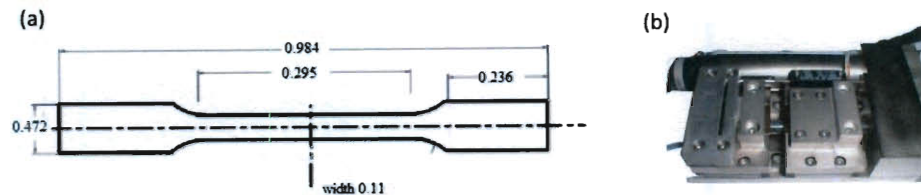
Figure 5.14 (a) Dimensions (in inches) of dog-bone specimens tested. The thickness of the specimens was 1 mm. (b) Image shows the Gatan™ Deben micro-tester.

From the stress vs. strain plots, shown in Figure 5.15 and the numbers reported in Table 5.5 it is clear that the tensile strength of the epoxy resin reduced considerably upon pristine and fluorinated MWNT addition. This behavior is not unusual since the interface between epoxy and carbon nanotubes is known to be considerably weak. Even upon MWNT fluorination, interfacial fracture energy values are much lower than that for engineering composites such as glass fiber reinforced vinyl ester (see Table 5.4). Also, owing to the high viscosity of the matrix material (and matrix nanotube mixture), uniform dispersions of MWNTs (pristine as well as fluorinated) in the matrix were probably not attained. A good dispersion is critical not only because it makes more filler surface area available for stress transfer, but also since it prevents the aggregation of the nanotubes. Aggregation causes nanotubes to act as stress concentrators and also leads to slippage of nanotubes during composite loading, thus degrading the performance of the composites greatly. [76] The existence of weak interfaces was corroborated by SEM images of fracture surfaces (see Figure 5.16). MWNT pullout was

consistently observed for both pristine and fluorinated MWNT reinforced composites thus confirming that interface failure was the dominant failure mechanism (fractured MWNTs were not observed on the surfaces). Dispersion levels, however, could not be assessed from the SEM images.

However, one should note that the addition of F-MWNTs results in a considerable improvement in the Young's modulus of the epoxy composite; no improvement was observed upon addition of pristine MWNTs. The reason for the improvement in stiffness, compared to pristine MWNT reinforced specimens, is not entirely clear. It presumably occurred owing to the relatively superior efficiency of load transfer to the reinforcements, as a result of the enhancement in nanotube-polymer interfacial adhesion brought about by fluorination.
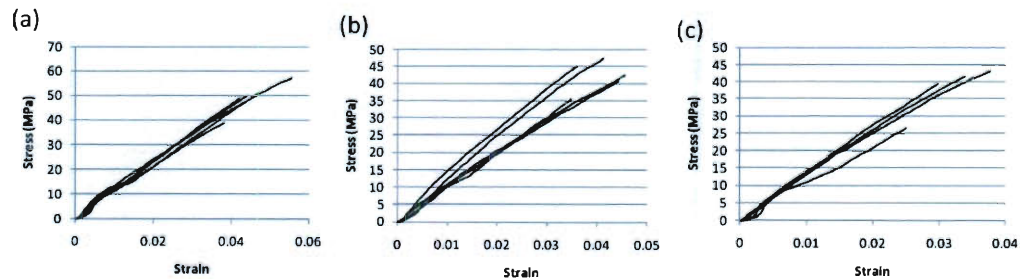
Figure 5.15 Representative stress vs. strain curves for (a) Epon 828 dog-bone specimens, (b) pristine MWNT reinforced Epon 828 specimens and (c) fluorinated MWNT reinforced Epon 828 specimens.

Table 5.5 Table summarizes mechanical properties of composites ascertained from tensile tests conducted on macro-scale dogbone specimens (average value for 10 specimens for each case).

Sample	Young's modulus (MPa)	Ultimate tensile strength (MPa)	Strain to failure
Epoxy	1099.0	52.24	0.05156
Pristine MWNT reinforced Epoxy	1099.2	40.20	0.03836
F-MWNT reinforced Epoxy	1290.2	30.33	0.02629
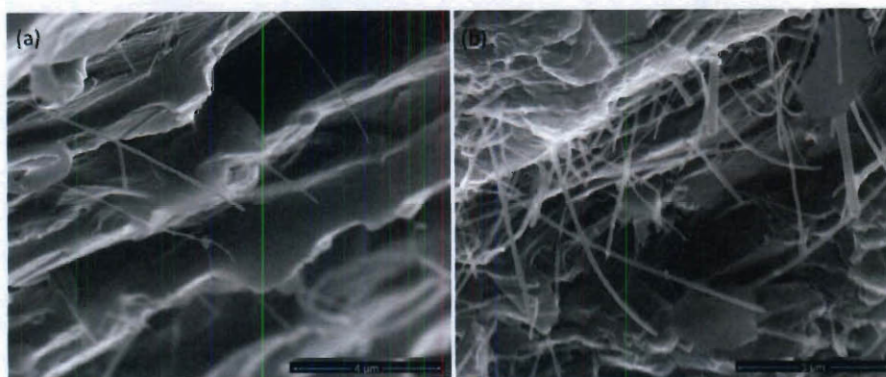
Figure 5.16 SEM images show fracture surfaces of (a) pristine MWNT reinforced epoxy specimens and (b) fluorinated MWNT reinforced epoxy specimens.

5.5. Load Transfer Analysis via Raman Spectroscopy

Micro-Raman spectroscopy was used to qualitatively assess the effectiveness of load transfer in the MWNT-reinforced epoxy composites because the second-order A_{1g} Raman peak position (around 2,700 cm^{-1}) shifts with applied strain on the tubes. [40] Raman spectra were acquired at each 30 N increment that occurred during the tensile tests conducted on the dog-bone specimens. A Renishaw^{TM} InVia Raman Microscope equipped with a 780 nm wavelength Laser was used for the spectral acquisitions. A considerable shift in the position of the second-order A_{1g} peak (larger shift for fluorinated MWNT reinforced specimens compared to pristine MWNT reinforced specimens) was observed upon nanotube

incorporation into the composites, based upon which one could conclude that the residual stresses in the composites were compressive in nature. This is because the load transfer in MWNT reinforced epoxy specimens has been known to be efficient under compression (see Chapter 2). The shifts in the position of the peak during the tensile tests were found to be insignificant, as expected. This phenomenon can be attributed to the weak coupling between the outer and inner shells of the multi-walled tubes during tension. In such composites, load transfer to MWNTs is known to occur in a fashion such that only the outer shells are stressed in tension whereas all the shells respond in compression. [40]
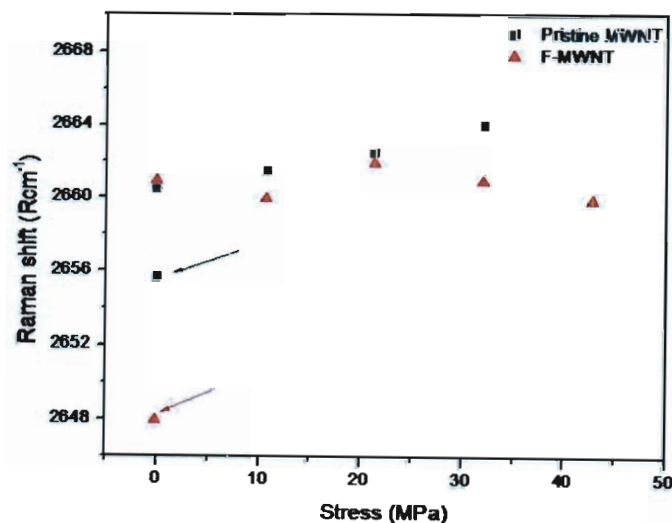
Figure 5.17 Plot shows shifts observed in the second order A_{1g} Raman peaks for pristine (black points) and fluorinated MWNTs (red points) as a function of applied stress. Points marked by arrows indicate the peak positions for the MWNTs before incorporation into the epoxy matrix.

5.6. Conclusions

The novel technique introduced in Chapter 3 was used to perform *in situ* single MWNT pullout experiments in order to study the properties of a MWNT-epoxy nanocomposite. Fifteen and thirteen successful pullout experiments allowed us to measure the interfacial fracture energy for the pristine MWNT-Epon 828 interface and the sidewall fluorinated MWNT-Epon 828 interface respectively. With regard to the pristine MWNT-Epon 828 interface, the interfacial fracture energy values were found to be considerably lower (by a couple of orders of magnitude) than those reported earlier for similar systems and those associated with conventional engineering composite systems. The interfacial fracture energy values improved upon MWNT functionalization (by about an order of magnitude). Macro-scale composite specimens, fabricated with fluorinated MWNTs as reinforcements, also exhibited a considerable increase in stiffness compared to unreinforced epoxy specimens.

6. Concluding Remarks

The development and application of a novel technique for mechanical characterization of nanomaterials and interfaces within an electron microscope was described in detail. The first set of experiments conducted using the technique, on individual Ni nanowires within a scanning electron microscope, yielded some interesting insights into size dependent mechanical behavior. For example, electrodeposited Ni nanowires were found to possess ultimate tensile strength values considerably higher than the ultimate tensile strength of Ni in bulk form. The technique was subsequently used for the *in situ* quantitative tensile testing of individual catalytically grown pristine, nitrogen doped and sidewall-functionalized (fluorinated) multiwall carbon nanotubes (MWNTs). The MWNTs were found to possess varied load bearing abilities and display unique fracture modes. Doped and sidewall fluorinated MWNTs were found to possess inferior load bearing abilities compared to pristine MWNTs owing to morphological differences and the degradation caused by functionalization respectively. Also, while undoped MWNTs failed in a brittle fashion, doped MWNTs were found to deform plastically, to a certain degree, prior to failure. Finally, the devices were used to perform single MWNT pullout experiments within a scanning electron microscope, in order to study the nature of adhesion at the MWNT/epoxy nanocomposite interface. The results of the pullout experiments, found to be qualitatively consistent with the predictions of continuum fracture mechanics models, showed that the interfacial strength (and toughness) of the pristine MWNT/Epoxy interface was considerably lower than that for conventional

engineering composite systems. However, a significant degree of improvement in the mechanical properties of the interface was observed upon sidewall fluorination of the MWNTs, possibly due to the increase in the extent of nanomechanical interlocking.

Even though there exists more than a decade's worth of research pertaining to the mechanical properties of CNTs and the interfacial properties and related load transfer mechanisms in CNT reinforced nanocomposites, our ability to engineer CNT based structural composites to achieve the desired properties still remains rather limited. The difficulties result from the lack of a solid physical understanding of CNT deformation and interfacial processes. The novel technique described in this thesis was developed in order to alleviate these issues. Future efforts need to be directed towards comparing the effects of various functionalization techniques and studying the influence of parameters such as the degree of functionalization and cure/post-cure temperature (interface studies) on the mechanical properties of CNTs and related interfaces. Looking forward, the author envisions the technique being used as a robust tool for studying novel reinforcement materials and for interface tailoring.

7. Related Publications and Patents

1. Y. Ganesan, Y. Lu, H. Lu and J. Lou, "*In Situ* Mechanical Characterization of One Dimensional Nanoscale Building Blocks Using Novel Microfabricated Devices", IEEE-NANO Conference Proceedings, 8, 2008.

2. Y. Ganesan and J. Lou, "Mechanical Characterization of Carbon Nanotube Reinforced Polymer Matrix Nanocomposites – An Unfolding Story of Interface", JOM, 61(1), 2009.

3. Y. Ganesan, Y. Lu, C. Peng, H. Lu, R. Ballarini and J. Lou, "Development and Application of a Novel Micro-fabricated device for *In Situ* Tensile Testing of 1-D Nanomaterials", Journal of Microelectromechanical Systems, 19(3), 2010.

4. Y. Ganesan, C. Peng, Y. Lu, L. Ci, A. Srivastava, P. M. Ajayan and J. Lou, "Effect of Nitrogen doping on the Deformation and Failure Mechanisms of Individual Catalytically Grown Multi-Wall Carbon Nanotubes", ACS Nano, in press, 2010.

5. Y. Ganesan, C. Peng, Y. Lu, P. E. Loya, P. Moloney, E. Barrera, B.I. Yakobson, J. M. Tour, R. Ballarini and J. Lou, "Interface Toughness of Carbon Nanotube Reinforced Epoxy Composites", ACS Applied Materials & Interfaces, in press, 2010.

6. Y. Lu, Y. Ganesan and J. Lou, "A Multi-step Method for *in situ* Mechanical Characterization of 1-D Nanostructures Using a Novel Micromechanical Device", Experimental Mechanics, 50(1), 2010.

7. Y. Ganesan, C. Peng, L. Ci, V. Khabashesku, P. M. Ajayan and J. Lou, "Effect of Sidewall Fluorination on the Mechanical Properties of Catalytically Grown Multi-Wall Carbon Nanotubes", 2010 Fall MRS Proceedings, in press, 2011.

8. Y. Ganesan, C. Peng, A. Cate, V. Khabashesku, R. Ballarini and J. Lou, "Effect of Sidewall Fluorination on the Interface Toughness of Carbon Nanotube Reinforced Epoxy Composites", in preparation.

9. C. Peng, Y. Ganesan, Y. Lu and J. Lou, "Size Dependent Mechanical Properties of Nickel Nanowires", in preparation.

10. Y. Lu, C. Peng, Y. Ganesan, J.Y. Huang, J. Lou, "*In situ* TEM tensile testing of nickel nanowires by using a novel micro mechanical device", in preparation.

11. Novel Micromechanical Devices for *In-situ* Characterizations of One Dimensional Nanomaterials, J. Lou, Y. Ganesan, Y. Lu and C. Peng, utility patent filed (USPTO# 20100108884), Oct. 2009.

8. References

1. B. C. Prorok et al., "Micro- and Nanomechanics", Encyclopedia of Nanoscience and Nanotechnology, 5, (2004), 555.

2. M. S. Dresselhaus et al., "Nanowires", Springer Handbook of Nanotechnology- Part A, (2010), 119.

3. B. Wu et al., "Mechanical properties of ultrahigh-strength gold nanowires", Nature materials, 4, (2005), 525.

4. S. Iijima, "Helical microtubules of graphitic carbon", Nature, 354, (1991), 56.

5. A. Thess et al., "Crystalline Ropes of Metallic Carbon Nanotubes", Science, 273, (1996), 483.

6. P. Nikolaev et al., "Gas-phase catalytic growth of single-walled carbon nanotubes from carbon monoxide", Chemical Physics Letters, 313, (1999), 91.

7. W. Z. Li et al., "Large-Scale Synthesis of Aligned Carbon Nanotubes", Science, 274, (1996), 1701.

8. P. Kim et al., "Thermal transport measurements of individual multiwalled nanotubes", Physical Review Letters, 87, (2001), 215502.

9. M. Kociak et al., "Superconductivity in ropes of single-walled carbon nanotubes", Physical Review Letters, 86, (2001), 2416.

10. Y. Ando et al., "Growing carbon nanotubes", Materials Today, 7, (2004), 22.

11. L. S. Schadler et al., "Polymer Nanocomposites: A Small Part of the Story", JOM, 59, (2007), 53.

12. P. J. F. Harris, "Carbon nanotube composites" International Materials Reviews 49, (2004), 31.

13. J. R. Greer and W. D. Nix, "Nanoscale gold pillars strengthened through dislocation starvation", Physical Review B, 73, (2006), 245410.

14. T. Dumitrica et al., "Symmetry-, time-, and temperature-dependent strength of carbon nanotubes", Proceedings of the National Academy of Sciences, 103, (2006), 6105.

15. M. F. Yu et al., "Strength and Breaking Mechanism of Multiwalled Carbon Nanotubes under Tensile Load", Science, 287, (2000), 637.

16. B. Peng et al., "Measurements of near-ultimate strength for multiwalled carbon nanotubes and irradiation-induced crosslinking improvements", Nature Nanotechnology, 3, (2008), 626.

17. M. F. Yu et al., "Tensile Loading of Ropes of Single Wall Carbon Nanotubes and their Mechanical Properties", Physical Review Letters, 84, (2000), 5552.

18. J. P. Lu, "Elastic properties of carbon nanotubes and nanoropes", Physical Review Letters, 79, (1997), 1297.

19. Z. Jia et al., "Study on poly-(methyl methacrylate):carbon nanotube composites", Materials Science and Engineering, A271, (1999), 395.

20. K. Liao and S. Li, "Interfacial characteristics of a carbon nanotube polystyrene composite system", Applied Physics Letters, 79, (2001), 4225.

21. P. M. Ajayan and J.M. Tour, "Nanotube Composites", Nature, 447, (2007), 1066.

22. C. A. Cooper et al., "Detachment of nanotubes from a polymer matrix", Applied Physics Letters, 81, (2002), 3873.

23. M. M. J. Treacy et al., "Exceptionally high Young's modulus observed for individual carbon nanotubes", Nature 381, (1996), 678.

24. P. Poncharal et al., "Electrostatic Deflections and Electromechanical Resonances of Carbon Nanotubes", Science, 283, (1999), 1513.

25. E. W. Wong et al., "Nanobeam Mechanics: Elasticity, Strength, and Toughness of Nanorods and Nanotubes", Science, 277, (1997), 1971.

26. J. P. Salvetat et al., "Elastic Modulus of Ordered and Disordered Multiwalled Carbon Nanotubes", Advanced Materials, 11, (1999), 161.

27. M. S. P. Shaffer and A. H. Windle, "Fabrication and Characterization of Carbon Nanotube/Poly-(vinyl alcohol) Composites", Advanced Materials, 11, (1999), 937.

28. H. Krenchel, Fiber Reinforcement (Copenhagen, Denmark: Akademisk Forlag, 1964).

29. M. Cadek et al., "Morphological and mechanical properties of carbon-nanotube-reinforced semicrystalline and amorphous polymer composites", Applied Physics Letters, 81, (2002), 5123.

30. J. C. Halpin Affdl and J. L. Kardos, "The Halpin-Tsai Equations: A Review", Polymer Science and Engineering, 16, (1976), 344.

31. H. D. Wagner et al., "Stress-induced fragmentation of multiwall carbon nanotubes in a polymer matrix", Applied Physics Letters, 72, (1998), 188.

32. A. Kelly and W. R. Tyson, "Tensile properties of fiber-reinforced metals: Copper/tungsten and copper/molybdenum", Journal of the Mechanics and Physics of Solids, 13, (1965), 329.

33. F. H. Gojny et al., "Surface modified multi-walled carbon nanotubes in CNT/epoxy-composites", Chemical Physics Letters, 370, (2003), 820.

34. V. Lordi and N. Yao, "Molecular mechanics of binding in carbon-nanotube–polymer composites" Journal of Materials Research, 15, (2000), 2770.

35. D. Qian et al., "Load transfer and deformation mechanisms in carbon nanotube-polystyrene composites", Applied Physics Letters, 76, (2000), 2868.

36. P. C. P. Watts and W. K. Hsu, "Behaviors of embedded carbon nanotubes during film cracking", Nanotechnology, 14, (2003), L7.

37. O. Lourie and H. D. Wagner, "Transmission electron microscopy observations of fracture of single-wall carbon nanotubes under axial tension", Applied Physics Letters, 73, (1998), 3527.

38. C. Bower et al., "Deformation of carbon nanotubes in nanotube–polymer composites", Applied Physics Letters, 74, (1999), 3317.

39. P. M. Ajayan et al., "Single-Walled Carbon Nanotube-Polymer Composites: Strength and Weakness", Advanced Materials, 12, (2000), 750.

40. L. S. Schadler et al., "Load transfer in carbon nanotube epoxy composites", Applied Physics Letters, 73, (1998), 3842.

41. T. K. Leeuw et al., "Strain Measurements on Individual Single-Walled Carbon Nanotubes in a Polymer Host: Structure-Dependent Spectral Shifts and Load Transfer", Nano Letters, 8, (2008), 826.

42. A. H. Barber et al., "Interfacial fracture energy measurements for multi-walled carbon nanotubes pulled from a polymer matrix", Composite Science and Technology", 64, (2004), 2283.

43. A. H. Barber et al., "Fracture Transitions at a Carbon-Nanotube/Polymer Interface", Advanced Materials, 18, (2006), 83.

44.   H. L. Cox, "The elasticity and strength of paper and other fibrous materials", British Journal of Applied Physics, 3, (1952), 72.

45.   Z. -F. Li and D. T. Grubb, "Single-fiber polymer composites Part 1", Journal of Materials Science, 29, (1994), 189.

46.   M. A. Haque and M. T. A. Saif, "*In situ* tensile testing of nanoscale freestanding thin films inside a transmission electron microscope", Journal of Materials Research, 20, (2005), 1769.

47.   P. E. Marszalek et al., "Atomic force microscopy captures quantized plastic deformation in gold nanowires", Proceedings of the National Academy of Sciences, 97, (2000), 6282.

48.   H. Kahn et al., "Electrostatically actuated failure of microfabricated polysilicon fracture mechanics specimens", Proceedings of the Royal Society London A, Mathematics Physics Engineering Science, 455, (1999), 3807.

49.   Y. Zhu and H.D. Espinosa, "An electromechanical material testing system for *in situ* electron microscopy and applications", Proceedings of the National Academy of Sciences, 102, (2005), 14503.

50.   S. Eppell et al., "Nano Measurements with Micro Devices: Mechanical Properties of Hydrated Collagen Fibrils," Journal of the Royal Society Interface, 3, (2006), 117.

51.   W. C. Oliver and G. M. Pharr, "Improved technique for determining hardness and elastic modulus using load and displacement sensing indentation experiments", Journal of Materials Research, 6, (1992), 1564.

52.   G. Feng et al., "A study of the mechanical properties of nanowires using nanoindentation", Journal of Applied Physics, 99, (2006), 074304.

53.   D. S. Gianola and C. Eberl, "Micro- and nanoscale tensile testing of materials", JOM, 61, (2009), 24.

54.   A. J. Durelli et al., "The theta specimen for determining tensile strength of brittle materials", Materials Research Standards, 2, (1962), 114.

55.   H. Guckel et al., "Diagnostic microstructures for the measurement of intrinsic strain in thin films", Journal of Micromechanics and Microengineering, 2, (1992), 86.

56.   T. M. Whitney et al., "Fabrication and Magnetic Properties of Arrays of Metallic Nanowires", Science, 261, (1993) 1316.

57.   M. A. Meyers and K. K. Chawla, Mechanical Behavior of Materials. Upper Saddle River, NJ: Prentice-Hall, 1998, ch. 2.

58.   A. M. Howatson, P. G. Lund and J. D. Todd, Engineering Tables and Data. Amsterdam, The Netherlands: Kluwer, 1991, p. 41.

59.   B. T. Kelly, In "Physics of Graphite", Applied Science: London and New Jersey, 1981; 477.

60.   K. Mølhave et al., "Electron irradiation-induced destruction of carbon nanotubes in electron microscopes", Ultramicroscopy, 108, (2007), 215.

61.   J. W. Jang et al., "Structural study of nitrogen-doping effects in bamboo-shaped multiwalled carbon nanotubes", Applied Physics Letters, 84, (2004), 2877.

62.   C. P. Ewels and M. J. Glerup, "Nitrogen Doping in Carbon Nanotubes", Nanoscience and Nanotechnology, 5, (2005), 1345.

63.   A. H. Barber et al., "On the tensile strength distribution of multiwalled carbon nanotubes. Applied Physics Letters, 87, (2005), 203106-1.

64.   B. Lukic et al., "Elastic modulus of multi-walled carbon nanotubes produced by catalytic chemical vapor deposition", Applied Physics A, 80, (2005), 695.

65.   M. Locascio et al., "Tailoring the Load Carrying Capacity of MWCNTs Through Inter-shell Atomic Bridging", Experimental Mechanics, 49, (2009), 169.

66.   M. B. Nardelli et al., "Brittle and Ductile Behavior in Carbon Nanotubes", Physical Review Letters, 81, (1998), 4656.

67.   J. Y. Huang et al., "Superplastic carbon nanotubes", Nature, 439, (2006), 281.

68.   J. Y. Huang et al., "Kink Formation and Motion in Carbon Nanotubes at High Temperatures", Physical Review Letters, 97, (2006), 075501-1.

69.   Z. Slanina et al., "Computational modeling of the elemental catalysis in the Stone–Wales fullerene rearrangements", Organometallic Chemistry, 599, (2000), 57.

70.   A. Hirsch, "Functionalization of Single-Walled Carbon Nanotubes", Angewandte Chemie International Edition, 41, (2002), 1854.

71.   J. L. Stevens et al., "Sidewall Amino-Functionalization of Single-Walled Carbon Nanotubes through Fluorination and Subsequent Reactions with Terminal Diamines", Nano Letters, 3, (2003), 331.

72. E. T. Mickelson et al., "Fluorination of single-wall carbon nanotubes", Chemical Physics Letters, 296, (1998), 188.

73. J. Zhu et al., "Improving the Dispersion and Integration of Single-Walled Carbon Nanotubes in Epoxy Composites through Functionalization", Nano Letters, 3, (2003), 1107.

74. V. N. Khabashesku et al., "Fluorination of Single-Wall Carbon Nanotubes and Subsequent Derivatization Reactions", Accounts of Chemical Research, 35, (2002), 1087.

75. M. D. Frogley et al., "Mechanical properties of carbon nanoparticle-reinforced elastomers", Composites Science and Technology, 63, (2003), 1647.

76. L. Liu and H. D. Wagner, "Rubbery and glassy epoxy resins reinforced with carbon nanotubes", Composites Science and Technology 65, (2005), 1861.

77. K. R. Jiang and L. S. Penn, "Improved analysis and experimental evaluation of the single filament pullout test", Composite Science and Technology, 45, (1992), 89.

78. C.A. May, Epoxy Resins, Chemistry and Technology (Marcel Dekker, New York, ed. 2, 1988), pp. 608.

79. C. Galiotis, "Interfacial studies on model composites by laser Raman spectroscopy", Composite Science and Technology, 42, (1991), 125.

80. M. Detassis et al., "Interface toughness in fiber composites by the fragmentation test", Composites A, 27, (1996), 769.

81. S. Zhandarov et al., "Investigation of load transfer between the fiber and the matrix in pullout tests with fibers having different diameters", Journal of Adhesion Science and Technology, 15, (2001), 205.

82. H. D. Wagner et al., "Stress-induced fragmentation of multiwall carbon nanotubes in a polymer matrix", Applied Physics Letters, 72, (1998), 188.

83. M. P. Manoharan et al., "The interfacial strength of carbon nanofiber epoxy composite using single fiber pullout experiments", Nanotechnology, 20, (2009), 295701-1.

84. Celene DiFrancia et al., "The single-fibre pull-out test. 1: Review and interpretation", Composites: Part A, 27A, (1996), 597.